TRANSPARENT CONDUCTORS BASED ON MICROSCALE/NANOSCALE MATERIALS FOR HIGH PERFORMANCE DEVICES

by

Tongchuan Gao

B. S., Tsinghua University, China, 2011

Submitted to the Graduate Faculty of

the Swanson School of Engineering in partial fulfillment

of the requirements for the degree of

Doctor of Philosophy

University of Pittsburgh

2016

UNIVERSITY OF PITTSBURGH

SWANSON SCHOOL OF ENGINEERING

This dissertation was presented

by

Tongchuan Gao

It was defended on

August 31st, 2016

and approved by

Paul W. Leu, Ph.D., Associate Professor, Department of Industrial Engineering

Bopaya Bidanda, Ph.D., Ernest E. Roth Professor, Department of Industrial Engineering

Jung-kun Lee, Ph.D., Associate Professor, Department of Mechanical Engineering & Materials Science

Youngjae Chun, Ph.D., Assistant Professor, Department of Industrial Engineering

Dissertation Director: Paul W. Leu, Ph.D., Associate Professor, Department of Industrial Engineering

TRANSPARENT CONDUCTORS BASED ON MICROSCALE/NANOSCALE MATERIALS FOR HIGH PERFORMANCE DEVICES

Tongchuan Gao, PhD

University of Pittsburgh, 2016

Transparent conductors are important as the top electrode for a variety of optoelectronic devices, including solar cells, light-emitting diodes (LEDs), flat panel displays, and touch screens. Doped indium tin oxide (ITO) thin films are the predominant transparent conductor material. However, ITO thin films are brittle, making them unsuitable for the emerging flexible devices, and suffer from high material and processing cost. In my thesis, we developed a variety of transparent conductors toward a performance comparable with or superior to ITO thin films, with lower cost and potential for scalable manufacturing. Metal nanomesh (NM), hierarchical graphene/metal microgrid (MG), and hierarchical metal NM/MG materials were investigated. Simulation methods were used as a powerful tool to predict the transparency and sheet resistance of the transparent conductors by solving Maxwell's equations and Poisson's equation. Affordable and scalable fabrication processes were developed thereafter. Transparent conductors with over 90% transparency and less than 10 Ω/square sheet resistance were successfully fabricated on both rigid and flexible substrates. Durability tests, such as bending, heating and tape tests, were carried out to evaluate the robustness of the samples. Haze factor, which characterizes how blurry a transparent conductor appears, was also studied in-depth using analytical calculation and numerical simulation. We demonstrated a tunable haze factor for metal NM transparent conductors and analyzed the principle for tuning the haze factor. Plasmonic effects, excited by some transparent conductors, can lead to enhanced performance in photovoltaic devices. We systematically studied

the effect of incorporating metal NM into ultrathin film silicon solar cells using numerical simulation, with the aid of optimization algorithms to reduce the optimization time. Mechanisms contributing to the enhanced performance were then identified and analyzed. Over 72% enhancement in short-circuit current-density was demonstrated by the optimal solar cell compared with 300-nm-thick Si solar cell with antireflection coating and silver back reflector.

TABLE OF CONTENTS

LIST OF TABLES

LIST OF FIGURES

PREFACE

This work is dedicated to my mom and dad.

I would first like to thank my academic advisor, Dr. Paul Leu, for giving me the opportunity to pursue my Ph.D. degree at University of Pittsburgh. Over the five years, his mentorship has always been very helpful and inspiring. I'd also like to thank him for challenging me and making a perfect environment for me to think and practice. I truly think being challenged was one of the most exciting and memorable part of my Ph.D. years.

I would also like to thank Professors Bopaya Bidanda, Jung-kun Lee, and Youngjae Chun for serving on my candidacy and thesis committees. I appreciate their time and the valuable comments on my research and on my life.

I would like to acknowledge and thank all of the students and staff members that I have worked with, learned from, and become friends with over the years. I'd like to thank Drs. Bo Ding, Zhiting Li, and Po-shun Huang for the useful discussions and their devotion to our research projects. I would like to thank the staff members who helped me at University of Pittsburgh: Dr. Susheng Tan, Mike McDonald, and Matthew France in Gertrude E. & John M. Petersen Institute of NanoScience and Engineering, Kim Wong in the Center for Simulation & Modeling, Albert Stewart and Cole van Ormer in the Materials Micro-Characterization Laboratory, and Dr. Joel Gillespie in the Materials Characterization Laboratory. I also would like to thank the folks at CMU Nanofab: Norman Gottron, Carsen Kline, Dr. Matthew Moneck, Dasheng Li, and Xiao Chuan Ong for the training sessions and helpful advice.

I would like to thank the undergraduate students I had the privilege of mentoring in Dr. Leu's Laboratory of Advanced Materials at Pittsburgh (LAMP): Sean McCarthy, Thomas Werkmeister, Donnie Voland, Brandan O'Brien, Ibrahim Chebib, Erica Stevens, Miriam

Rathbun, Lincoln Walton, and Michael Bollenbacher. Thomas is applying for graduate school and I hope maybe we can collaborate someday. I'd like to dedicate my thanks to my lab brother Baomin (now he is Dr. Wang) who offered me kind help when I first came to Pittsburgh and worked closely on research projects with me. It has never been boring arguing with him on research and it was also a lot of fun chatting with him about sports, music, and everything.

I also would like to thank my old friends from Tsinghua University and my high school: Dr. Chen Sun, Dr. Chengyu Mao, Xian Shi, and Tao Zhang; and my roommates: Kexi Liu and Ruichen Sun. Friends made me relax after a day's research and gave me spirit for tomorrow.

I would like to thank Pet Shop Boys, My Little Airport, Deserts Xuan, the Velvet Underground, the Beatles, and the other musicians appearing in my playlists for providing the fantastic music which always made me happy and enjoy my life.

I would like to dedicate my special thanks to Miss Qi Zhang for all her company and the sweet moments over the two years. You always give me the energy to become a better researcher and also a better person in life. Lastly but most importantly, I would like to thank my mom and dad for their unconditional love and for supporting me to pursue my Ph.D. degree abroad. You are the reason I have done all this.

And, grandma, how I wish you could see this, too.

Tongchuan Gao

August 2016

Pittsburgh, PA

1.0 INTRODUCTION

1.1 APPLICATIONS OF TRANSPARENT CONDUCTORS

Transparent conductors (TCs), which are optically transparent ($> 80\%$) and electrically conductive ($< 10\ \Omega$/sq) simultaneously, play a crucial role in a variety of photonic and optoelectronic devices and have been comprehensively studied since 1907 by Bädeker.[1, 2] As is implied by the name, transparency and electrical conductivity are the two most important figure of merits for assessing the performance of a TC material. The burgeoning of research on novel photonic and optoelectronic devices puts increasingly stringent requirement for performance onto TC materials, thus greatly prompting the research in this field in the past decade. For example, Rowell *et al* has reported that a transparency over 90% at a sheet resistance of less than 10 Ω/sq is the prerequisite for a competitive monolithically integrated thin film solar cell module,[3] which is something far from trivial to achieve.

From a electrodynamics point of view, the optical transparency and electrical conductivity of a material is inherently determined by its complex permittivity $\epsilon = \epsilon' + \mathrm{j}\epsilon''$, where ϵ' and ϵ'' are the real part and the imaginary part of permittivity, respectively, and $\mathrm{j}^2 =$ -1. Optical transparency is often a characteristic of dielectrics, indicated by a real ϵ with a positive value. That the imaginary part of permittivity ϵ'' is zero indicates that they are electrical insulators. However, electrical conductivity is predominantly possessed by metals, described by a negative ϵ' and a non-zero ϵ''.[4] The dilemma can be solved using a variety of strategies, including making an insulator conductive without affecting the optical properties, *e.g.* by doping tin oxide to degeneracy using indium atoms,[5] exploring new physics in materials,[6] or combining the optical and electrical properties of multiple materials. The development of metal nanomesh (NM) is an example of the third strategy that combines

the excellent conductivity of metal and the transparency of air.[7] Furthermore, hierarchical materials have also been investigated recently using the this strategy.[8, 9]

Apart from increasing the transparency while reducing the sheet resistance, effort has also been devoted by the industry to the realization of inexpensive manufacturing methods of scalable and flexible TCs, so as to accommodate the emerging flexible and wearable devices.[10–12] Bae *et al* reported successful fabrication of 30-inch graphene thin films with 97.4% optical transmittance at a sheet resistance of 125 Ω/sq using roll-to-roll technique.[13] Advanced printing techniques offer another approach for the fabrication of TCs and even devices. Hu *et al* reported on the printing of Ag nanowire (NW) ink onto a flexible plastic film using a Meyer rod and achieved over 80% transparency at a sheet resistance of 8 Ω/sq.[14] Supercapacitors on cloth fabrics were successfully printed using a modified inkjet printer by researchers in the Chongwu Zhou group.[15] Other methods, such as vacuum filtration,[16] convective self–assembly,[17] and capillary printing,[18] have also been demonstrated and showed potential for industry scale manufacturing.

Beside the transparency and electrical conductivity, more application specified characterizations, including haze factor and work function, are of special interest to the TC researchers and have been intensively studied. Haze factor will be discussed in more detail in the following chapters. Applications such as flat panel displays and touch screens require very low haze factor for a clear appearance, while applications such as solar cells favor both a high transparency and a high haze factor to increase the light path length in the photoactive layer. Preston *et al* theoretically studied the haze factor of Ag NWs using scattering theory and simulation tools.[19] Work function matching is important for devices including solar cells and photoelectrochemical cells. Zhou *et al* developed a universal method to produce low work function TCs by the incorporation of aliphatic amine groups.[20] More and more work is being focused on these topics towards a more comprehensive understanding in the compatibility between TCs and the user devices.

Being not only a hot topic for researchers in academia, TC materials also possess a growingly huge market. The demand for TCs has been increasing rapidly over the past decade and it is forecasted that the transparent conductive film/glass market will be over $6 billion market by 2024 (Source: Transparent Conductive Films (TCF) 2014-2024: Forecasts,

Markets, Technologies (IDTechEx)). The trend is expected to continue for the foreseeable future. Liquid-crystal displays (LCDs) is currently the largest user of TCs, while other applications, such as touch screens,[13, 21, 22] light-emitting diodes (LEDs),[23–25] transparent heaters,[26] smart windows,[27] and electromagnetic interference shields,[28] also see a rapid growth in their market shares. The emerging of flexible devices prompt the investigation of novel TCs suitable for such applications, although rigid devices still have a huge market share. Currently, the most mature and dominant TC material is tin-doped indium oxide (ITO), with $3 billion dollar market in 2010.[29] However, ITO is expected to lose some of its market share to new TC materials. In the following section, a brief review of typical TC materials is presented.

1.2 DOPED METAL OXIDES

Transparent conductive metal oxides (TCOs) are the prevailing TC materials today. The interest in TCOs may date back to 1900s, when Bädeker studied the resistivity of CdO, Cu_2O and PbO.[1] Amongst them, CdO thin films have a transparent appearance with resistivity only one order of magnitude higher than that of ITO. In 1947, SnO_2 was used as transparent heating layer for airplane cockpit windows.[30] Fluorine and antimony-doped tin oxide (FTO and ATO) were the first commercialized TCO materials and are still widely used in thin film solar cells today. In_2O_3 attracted scientists' interest in 1960s as infrared filters in low-pressure sodium discharge lamps.[31]Zinc oxide (ZnO) was initially used as a compound semiconductor, whereas thin film ZnO was then investigated as piezoelectric devices in 1960s.[32] As a TCO material, the lowest resistivity of antimony doped zinc oxide (AZO) is 2 - 4 $\times$ 10^{-4} Ω cm, which is between SnO_2 and ITO and two orders of magnitude higher than silver. Since invented in 1947 by Corning company, the properties and the deposition technique of ITO have been vastly developed for over 50 years with the prosperity of flat-panel display industry. The ability of depositing ITO with a well-controlled thickness and doping concentration makes it the most mature TCO material today.

Most of the TCOs are degenerately doped n-type wide band-gap semiconductors, such as ITO, AZO, FTO, and ATO. They are absorbing in the UV regime due to the excitation of electrons from the valence band to the conduction band, and photons with an energy lower than the plasma energy will be reflected by the free electrons. To maintain an transparency window in the visible range, the key factor to be tuned is the ratio of the free carrier concentration n and the effective carrier mass m^*.[6]

The resistivity ρ of TCOs is typically 10^{-4} –10^{-3} Ω cm due to the relatively high mobility ($\mu < 100$ cm^2 V^{-1} s^{-1}), compared to $\rho = 1.6 \times 10^{-6}$ Ω cm for the best conductor – silver. The resistivity originates from that the charge carriers are scattered by both phonons and ionized doping atoms, while the latter is dominant. The mobility contributed by uniformly distributed scattering centers in TCO is given by

$$\mu_{ii} = \frac{3(\epsilon_r\epsilon_0)^2h^3}{Z^2m^{*2}e^3}\frac{n}{N_i}\frac{1}{F_{ii}^{np}(\xi_d)} \tag{1.1}$$

where $\xi_d = (3\pi^2)^{1/3}\epsilon_r\epsilon_0h^2n^{1/3}/m^*e^2$, $\epsilon_r\epsilon_0$ is the permittivity of the metal oxide, h is Planck's constant, e is the elementary charge, n and N_i are the electron and ionized doping atom concentrations respectively, Z and F_{ii}^{np} are the number of charge and the screening function for a non-parabolic conduction band for ionized doping atoms respectively, ξ_d is the screening parameter, and m^* is the effective mass of charge carrier.[33] However, lattice defects, which are introduced by doping and deposition process, will significantly reduce the mobility of TCO.

A variety of thin film deposition methods have been developed to deposit TCOs, such as ITO, FTO, and AZO. The optical and electrical properties strongly depend on the deposition method, because different deposition methods will result in different material nanostructure and defect status. Commonly used deposition techniques for ITO thin films include evaporation, sputtering, reactive ion plating, chemical vapor deposition (CVD), spray pyrolysis, dip coating, and sol-gel method.

In manufacturing environment, dc magnetron sputtering is typically used as the deposition method.[34] Annealing at elevated temperature (> 135 °C) is required for the as-deposited amorphous ITO to crystallization. The conductivity of ITO will be increased by 5 times after about 10 h annealing at 135°C. A 100-nm-thick ITO thin film has can achieve an

average visible transparency of 85% at a sheet resistance of 15-20 Ω/sq, which is adequate for most optoelectronic devices.

Though as the best TC material, ITO thin film suffer from several drawbacks, hindering its dominance and development in the future. First, In is a rare metal with rising price.[35] As a byproduct from Zn mining, the In supply is usually below demand. The In over Sn atom ratio in ITO is 90/10 when the optimal TC properties are achieved, which means the mass of In is 75% of ITO. Second, the commercially used dc magnetron sputtering process requires high temperature, making it unsuitable for emerging organic devices. Third, the work function of ITO depends on the cleaning procedure of the substrate.[36] Fourth, as a ceramic material, cracks form and propagate in ITO easily under small strain, degrading the conductivity significantly. Therefore it is not suitable for flexible devices and resistive touch screens. Last, the ITO is only transparent in the visible range, making it unsuitable for applications such as UV LEDs and IR detectors.

AZO and FTO are considered decent alternatives to replace ITO. AZO, which is widely used in CIGS solar cells[37] and LEDs,[38] is an inexpensive substitution for ITO. Sputtering is commonly used for AZO deposition and usually followed by annealing processes. However, the electrical stability of thin AZO film remains a concern especially in high humidity situations. FTO, which can be grown using CVD, is widely used in solar cells. However, the etching of AZO is prohibitively difficult, hindering its usefulness in nanoscale/microscale applications.

Towards better performance on flexible devices and lower manufacturing cost, a variety of novel materials have been developed as potential substitutes for TCOs, such as conductive polymers, carbon nanotube and graphene thin films, metal NW networks, and hierarchical structures.

1.3 CONDUCTIVE POLYMERS

Conductive polymers have emerged as a good substitution for TCOs with good electrical conductivity and optical transparency. These materials also offer excellent flexibility, good

processability and compatibility with plastic substrates, and lower cost. The conductivity of polymers originates from charged doping in the polymer chains by the solvent and other additives. Historically, a broad range of conductive polymers have been developed, including polythiophene (PT) and its derivatives, poly(paraphenylene vinylene) (PPV), polypyrrole (PPy), polyaniline (PANI), and so on. Currently, PT and PANI with their respective derivatives are the mostly used conductive polymers. PT materials are a family of conjugated polymers with good environmental stability. The most important PT derivative is poly(3,4ethylenedioxythiophene) (PEDOT), which is usually stabilized by polystyrenesulfonic acid (PSS) in aqueous environment. PEDOT:PSS has been used in a broad range of applications, such as solar cells,[39] nonlinear optical devices,[40] OLEDs,[41] and smart windows,[42] and received vast commercial success. PEDOT:PSS is also used with other TC materials for a smoother surface and thus better performance[43]. PANI, similar to PEDOT, is a positively doped polymer. PANI is normally processed by solution-cast[44] and electrospinning.[45] TC materials based on PANI fibers, graphene/PANI and carbon nanotubes/PANI composites have been reported.[46–48] PPy has its applications as sensitizer in solar water splitting devices.[49] However, conductive polymers still suffer instability of the doped state, resulting in a gradual degradation in the electrical conductivity.

1.4 CARBON NANOTUBES AND GRAPHENE

1.4.1 Carbon Nanotubes

Carbon nanotubes (CNTs) are tubular allotropes of carbon consisting of coaxial tubes of graphitic sheets, first discovered by Iijima in 1991 using arc-discharge evaporation[50]. "Needle-like" tubular structures was found at the negative electrode. In terms of the number of graphitic sheets in an individual tube, CNTs are categorized as single-walled nanotubes (SWNTs) and multi-walled nanotubes (MWNTs). Carbon atoms are $sp2$ hybridized in SWNTs and a series of coaxially aligned SWNTs form MWNTs by van der Waals forces.

The structure of a SWNT can be considered as a single graphite sheet wrapped to form a seamless tube. SWNTs can either be metallic or semiconducting depending on the direction of wrapping, represented by indice pair (m, n), where m and n are integers. SWNTs are can be categorized into either of armchair, zigzag, or chiral by (m, n). WMNTs share similar electrical properties to SWNTs when free of defects and contaminations. Electrons are transported ballistically along a CNT, making it capable of carrying high current without significant heat effect. Though it is difficult to limit the type of SWNTs in producing, SWNTs with certain chirality can be sorted by post-treatments. For example, metallic SWNTs can be selectively eliminated by electrical heating. SWNTs with small diameter have exceptionally high stiffness and strength, with density-normalized Young's modulus and yield strength 19 and 56 times that of steel, respectively. The high mechanical strength and chemical stability of SWNTs make them a promising candidate for durable TCs.

Two-dimensional random networks may be the most viable form of utilizing CNTs for TCs. Purified SWNTs, usually a mixture of metallic and semiconducting types, are most commonly used for such purpose. Both wet and dry processing techniques have been developed to fabricate CNT TCs. Wet processing methods include spin coating, dip coating, and vacuum filtration. Conductive CNTs films consisting of both SWNTs and DWNTs were reported by Mirri *et al* using scalable dip coating method[51]. CNTs were dispersed in chlorosulfonic acid (CSA) solutions without the use of surfactants, functionalization, or ultrasonication and then coated onto glass slides using dip coating. The sheet resistance was 100 Ω/sq at 90% transmission in the visible.

Despite that these methods are scalable and have high throughput, the presence bundled CNTs becomes a major issue. Vacuum filtration will have better dispersion. The advantage of solution based methods is that they may be potentially incorporated to roll-to-roll processes, which allows for continuous, automatic, and scalable manufacturing.

1.4.2 Graphene

Graphene is a two-dimensional crystal consisting of a single-layered graphite sheet with $sp2$ hybridized carbon atoms bonded in a hexagonal lattice. Graphene flakes were discovered by

Novoselov and Geim *et al* using mechanical exfoliation in 2004[52] and a variety of modified procedures were developed afterwards.[53] Though great research interest incentivized, it is difficult to study the physics and the properties with the exfoliated graphene flakes due to their small size and irregular shape. CVD was then used to grow large scale monolayer graphene and few-layer graphene (FLG). Few-layer graphite has been successfully growth epitaxially on metals such as Pt,[54] Ni,[55] Fe,[56] Pd, and Co[57] with carbon-containing gas at high temperature ($\geq$ 1000°C). The growth mechanism is interpreted as that the C atoms, from the decomposition of C-containing gases, are dissolved in and segregate on the surface of metal to form graphene layers. H_2 is often used to eliminating the contamination in metal for uniform growth. However, it is difficult to exclusively get single-layered graphene because C atoms dissolved in metal tend to continue segregating on the metal surface when the system cooling down. Today, Cu has been proved as an excellent catalytic substrate for growing exclusively single-layered graphene using methane (CH_4) and H_2 at 1000°C,[58, 59] because the solubility of C in Cu is about 1/1000 of that in Ni at 1000°C,[60, 61] minimizing the forming of more layers.

The π-conjugation in single-layer graphene leads to different behaviors from bulk materials. Unique thermal, mechanical, and electrical properties of graphene were unveiled. A thermal conductivity of approximately 5000 $Wm^{-1}K^{-1}$,[62] Young's modulus of about 1 TPa,[63] and an intrinsic carrier mobility of 200000 $cm^2V^{-1}s^{-1}$.[64] As a semiconductor with zero band gap, graphene has many interesting properties, including quantum Hall effect[65] and zero electron effective mass near the Dirac point. Graphene films (ranging from monolayer graphene to FLG) have recently emerged as a promising transparent electrode material due to its high carrier mobility and high transparency when thin.[66, 67]

The first graphene-based transparent conductor was reported by Wang *et al*.[68] Films were deposited by dip-coating with graphene oxide (GO) and reducing by thermal annealing. Sheet resistances as low as 0.9 kΩ/sq were obtained at 70% transmission. Reduced graphene oxide (rGO) was solution-processed for transparent conductor in OLEDs.[69, 70] CVD grown graphene less imperfection and is more scalable, making it preferable to exfoliated graphene for TCs. Transferring techniques for CVD grown graphene was developed and TCs with improved performance were reported.[71, 72] Roll-to-roll manufacturing of 30-inch

graphene-based TCs were reported by Bae *et al*,[13] making scalable automated manufacturing possible. Graphene-CNT hybrid TC was also reported with $R_s = 240\ \Omega/\text{sq}$ at $T = 86\%$.[73]

1.5 METAL NANOWIRES

Metal NWs (NWs) with high aspect ratio and good conductivity are promising building blocks for TCs as a substitute for ITO. Ag, Cu, Al, and Au are the most commonly used NW metals to form the network. The prevailing synthesis method today is the seeding and growing in solution environment. NWs can also be prepared by metal deposition on a patterned substrates. Most of the metal NWs solution-processed to fabricate TCs, allowing for scalable manufacturing.

One-dimensional[63] and two-dimensional[74] Ag gratings were investigated using simulation methods and they demonstrate comparable performance to ITO. Lee *et al* fabricated two-dimensional percolation Ag NW networks on glass slide by dipping a NW suspension onto the substrate and drying.[63] Further research has followed up to improve the TC performance of NWs.[14, 16, 75, 76] Also, Ni was used to form alloy with Cu to improve the resistance to oxidation at elevated temperature.[77] Other structures such as metal nanotroughs,[12] TiN nanofibers,[78] and metal networks by grain boundary lithography[79] were also reported with impressive performance.

To achieve a high transmission at a given R_s, networks consisting of long NWs with a large diameter is favorable.[80, 81] However, a large separation between NWs will result in poor localized conductivity and thus, poor uniform carrier collection or delivery. This is especially a problem for organic optoelectronic devices, which have short exciton diffusion lengths. A variety of hierarchical structures were investigated to combine the advantage of microscale materials and nanoscale materials.[8, 82, 83]

1.6 PHOTOVOLTAICS PERSPECTIVE

Solar energy, as the world's fastest growing energy source, are forecasted to provide over 10% of the energy for the world by 2050. It is commonly accepted that the electricity price provided by solar cell systems must be below \$1/W$_p$ so as to be competitive with the conventional retail electricity. Wafer based solar cells, including single crystal silicon and multicrystalline silicon solar cells, used to take up to 90% of the market share. However, the market share of wafered solar cells has dropped below 90% due to the fast growth of thin film solar cell industry. Amorphous silicon (a-Si), cadmium telluride (CdTe), copper indium gallium selenide (CIGS) thin film solar cells and dye-sensitized solar cells have been extensively studied in the past decades. Despite the manufacturing cost of CdTe thin film solar cells has been reduced to below \$1/W$_p$ by *First Solar*, there is still plenty of interest in the research of improving the performance of silicon based solar cells due to their huge market share and mature manufacturing protocols. The cost of a silicon based solar cell can be distributed to the following parts: the cost of silicon wafer, the cost of module fabrication, and the cost of cell. The cost of silicon wafer can be then broken down to the raw material cost, crystal growth cost, and sawing cost. Historically, the most significant cost of solar cell modules is the cost of photoactive material, *e.g.* crystalline silicon. However, as the price of solar cells saw a dramatic decline in the past decade, other costs of a solar cell system become increasingly important. One of the most prominent costs coming into our attention is from the balance of systems (BOS). Considering the high BOS cost, it will be more economical to use slightly more costly but more efficient solar cells in the system. In this work, our aim is to significantly improve the solar cell performance of silicon based solar cells even with slightly increased cost. For example, in our study of the Cu nanomesh as the top electrode for solar cells. The marginal cost will be \$10 for a 4-inch solar cell considering the cost of polystyrene nanospheres and metal deposition.

2.0 CHARACTERIZATION OF TRANSPARENT CONDUCTORS

2.1 SHEET RESISTANCE

Sheet resistance (R_s) is a measure of electrical resistance of thin film materials with a uniform thickness, commonly used in semiconductor industry and coating materials. The unit of R_s is Ω/sq. More detail on the definition and the measurement of R_s can be found in the classic textbook by Schroder.[84] For homogeneous thin film materials, the sheet resistance is calculated by

$$R_s = \rho/t \tag{2.1}$$

where ρ is the resistivity of the material and t is the thickness. Though bulk resistivity is usually assumed when the film is not very thin for simplicity, corrections accounting for the surface and/or grain boundary scattering of electrons is sometimes necessary for more accurate modeling of R_s due to the polycrystalline nature of evaporated metal thin films.[85, 86]

In experiments, four-point probe method and van der Pauw method are the two commonly used methods for R_s measurement. A four-point probe, also known as Kelvin probe, with two probes applying current I and two sensing voltage V, is used to offset the contact resistance between probes and the material, which may be greater than the sheet resistance. A factor depending on the spacing between each probe and the dimension of the sample is required for correction purpose. Specifically with our equipment setup, R_s is calculated as follows when the size of the sample is not smaller than 2 cm by 2 cm.

$$R_s = 4.53\frac{V}{I} \tag{2.2}$$

Van der Pauw method is used when four-point probe method is not applicable, *e.g.* when it is difficult to get good contact between the probes and the sample. In order to reduce error in measurement, geometrically symmetric samples are prepared and four small contact pads are deposited close to the boundary of the sample using conductive silver paste to form Ohmic contact. The four contacts are numbered 1 to 4 in a clockwise manner. A current I_{12} is applied to contact 1 and 2 and the voltage V_{34} is measured between contact 3 and 4. The resistance is then calculated according to Ohm's law: $R_{12,34} = V_{34}/I_{12}$. Similarly, $R_{23,41}$ is measured with current applied to contact 2 and 3 and voltage measured between contact 4 and 1. Using van der Pauw formula, R_s is obtained by solving:

$$e^{-\pi R_{12,34}/R_s} + e^{-\pi R_{23,41}/R_s} = 1. \tag{2.3}$$

R_s is measured on a Hall effect measurement unit at room temperature and the result is the average of four measurements with current applying to different pairs of contacts.

2.2 TRANSMISSION AND HAZE FACTOR

Optical transmission of TC materials is measured using a Perkin Elmer Lambda 35 UV-visible spectrophotometer. The incoming light generated by the deuterium lamp ranges from 190 to 1100 nm.The wavelength range of interest is from 400 to 1000 nm and the optical slit width is 2 nm. Diffusive transmission T, which accounts for the transmitted light from all angles, is measured with a Labsphere RSA-PE-20 diffuse-reflectance integrating sphere accessory. Specular transmission T_{spec}, which only accounts for the normally transmitted light, is measured without the integrating sphere. Transmitted light with an horizontal angular divergence of about $\pm 3^\circ$ is accepted by the detector. In order to obtain the total reflection of the TC materials, an 8° angled sample holder is placed at the backside of the integrating sphere, and a barium sulfate Lambertian reflector is used as a standard control sample. The subtraction of diffusive transmission and reflection from the unity gives the absorption spectrum of the sample.

The haze factor, defined as $(T - T_{spec})/T$, is an important property for TCs to quantify the extend of haziness. The haziness of metal NW network, for example, originates from the Mie scattering from individual NWs, resulting in a haze factor of 13% to 33%. TCs with very low haze factor are desirable for applications such as flat panel displays and touch screens, while TCs with high haze factor are beneficial as top electrode for solar cells to increase the length of optical path in absorber.

2.3 FIGURE OF MERITS

From uniform thin films such as ITO thin films, there is inevitably a tradeoff between transparency and sheet resistance. Sheet resistance and transparency is simultaneously reduced when the film thickness increases. TC in devices can be either active or passive roles. For passive type, a knowledge of sheet resistance and transmission separately will satisfy the requirement. However, a proper combination of sheet resistance and transmission is required to compare the performance of TCs in active type devices to address the inherent tradeoff, due to the more stringent device requirement.[87] A combination of R_s and T for TC performance comparison is called a figure of merit (FoM).

One early FoM defined by Fraser and Cook in 1972 is $F = T/R_s$.[88] However, this FoM gives R_s too much weight. The FoM is modified by Haacke in 1976[89] as

$$\phi = \frac{T^{10}}{R_s}. \tag{2.4}$$

For solid thin films, the FoM is then expressed as $\phi = \sigma t e^{-10\alpha t}$, where σ is the conductivity, t is the thickness of the film, and α is the absorption coefficient of the material. For TCs with a give R_s, a greater σ/α ratio will lead to higher ϕ. For comparing TCs with the same thickness, the FoM F = -$R_s$ln$T$ is often used. Recently, σ_{DC}/σ_{op} is a commonly used FoM for nanostructure-based transparent conductors,[90] where σ_{DC} is the dc conductivity of the material and σ_{op} is the optical conductivity. This FoM can be represented in terms of T and R_s by

$$T = \left(1 + \frac{\mathrm{Z}_0}{2R_{\mathrm{s}}}\frac{\sigma_{op}}{\sigma_{DC}}\right)^{-2}, \tag{2.5}$$

where $Z_0 = 377\ \Omega$ is the free space impedance. As a function of thickness, the FoM can be written as

$$T = (1 + 188.5\sigma_{op}t)^{-2}. \tag{2.6}$$

Notably, all the FoMs are functions of wavelength λ. Here, all the FoMs are calculated at λ = 550 nm unless noted.

2.4 DURABILITY TESTS

To examine the durability of the TCs, a variety tests are designed including bending test, heating test, and tape test.

Bending test is designed for testing the robustness of flexible TCs under repeating bending with a given curvature. The samples are bended around a steel rod and the sheet resistance or resistance is monitored. The bending is done with the conducting films either towards or opposite to the rod, corresponding to compression and tension test.

The heating test is designed for examining the chemical stability of TCs under constant heating. Samples are placed on a hot plate and are heated at elevated temperature in ambience. Sheet resistance or resistance is monitored as a variable evolving with time.

Tape test is designed for testing the attachment of conductive films to the substrate. Scotch tape is pressed onto the TC with finger pressure and then pulled off to assess the attachment of film to the substrate. Sheet resistance or resistance is monitored as a function of the number of test cycles.

For all the tests monitoring resistance of the TCs, two rectangular Au contact pads are deposited on the sample to minimize the measurement errors.

3.0 METAL NANOWIRES FOR TRANSPARENT CONDUCTORS

Metal NW networks have been experimentally demonstrated as excellent TC materials to replace ITO thin films.[14, 75–77] However, theoretical study on how the dimensions of NWs and the density of network affect the transparency and sheet resistance is still lacking. Here, we propose to theoretically evaluate the performance of metal NW arrays for TCs and shed light on the physical mechanisms governing the light-matter interaction in a NW system. 1D and 2D Ag NW networks are first investigated and compared with ITO using the FoM. Cu NWs, as an inexpensive substitute for Ag NWs, are then examined, along with the impact of alloying Cu with Ni to form cupronickel as a protection layer.

3.1 SILVER NANOWIRE ARRAYS

3.1.1 Schematic and Methodology

Figure 1 shows the schematic of the different transparent conductor systems we studied: (a) Ag thin films defined by thickness t, (b) 1D Ag NW arrays with diameter d and pitch a, and (c) 2D Ag NW arrays. The 2D Ag NW arrays are also defined by diameter d and the pitch a of the square lattice. Silver thin films thicknesses $t = 1$ to 158 nm were studied, and Ag NW arrays with NW diameter range from $d = 5$ to 400 nm and pitches a from 5 to 2000 nm with $d \leq a$ were investigated. The optical properties were determined by solving Maxwell's questions using the finite difference time domain (FDTD) method.[91, 92] The optical constants for silver were taken from experimental measurement results in Palik's *Handbook of Optical Constants of Solids*.[93] A non-uniform simulation mesh with a finer

mesh near interfaces and larger mesh in bulk regions was utilized. Perfectly matched layer boundary conditions were used for the upper and lower boundary of the simulation cell,[94] while appropriate periodic boundary conditions were used for the side boundaries to model the periodic nature of the arrays.

To study the performance of these different structures as transparent conductors, the solar integrated transmission was calculated from

$$T_{solar} = \frac{\int b(\lambda)T(\lambda)d\lambda}{\int b(\lambda)d\lambda} \tag{3.1}$$

where λ is the free-space wavelength, $b(\lambda)$ is the photon flux density, and $T(\lambda)$ is the optical transmission for light with wavelength λ. We considered the wavelength range $\lambda = 280$ to 1000 nm of the global 37° tilt AM1.5 solar spectrum.[95]

ch

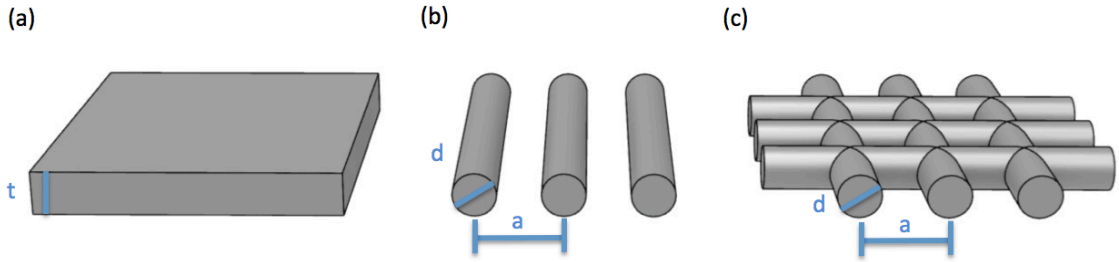

Figure 1: Schematic of structures studied: (a) silver thin film with thickness t, (b) 1D Ag NW array with pitch a and the diameter d, and (c) 2D Ag NW array.

3.1.2 Results and Discussion

Figure 2(a) illustrates a contour plot of $T(\lambda)$ for silver thin films of thickness t. At larger wavelengths, photons are governed by free electron-like behavior as governed by the Drude model. Almost all of the incident light is reflected since the real part of the index of refraction is small and $R(\lambda) = |(n(\lambda) - 1) / (n(\lambda) + 1)|^2$ where $n(\lambda)$ is the complex index of refraction of silver and the index of refraction of air is 1. Below 310 nm, interband transitions from d

electrons to the Fermi surface start to become important. The absorption edge is at about 320 nm (3.9 eV), which is associated with interband transitions from the L_{32} to $L_{2'}$ band.[96] Silver thin films have some reflection and high absorption for photons with lower wavelength than this absorption edge.

The plasma frequency of the free electrons in the silver is about 130 nm (9.2 eV) and thus, photons across the entire solar spectrum range cannot propagate in silver. Ag films only support evanescent modes, where the electromagnetic field intensity decays exponentially from the front surface. The transmission in films is described by the skin depth, where transmission is possible when t is comparable or smaller than the skin depth. The skin depth of Ag is slightly over 20 nm for most of the spectral range of interest and has a maximum at the 320 nm wavelength.

Figure 2(b) plots T_{solar} with the same y-axis as in (a) with R_s shown on the right y-axis. $R_s = \rho_{bulk}/t$ where $\rho_{bulk} = 1.59 \times 10^{-8}$ Ω·m, which is the bulk silver resistivity.[97] Because the transmission is evanescent in silver thin films, T_{solar} rapidly decreases with increasing thickness. $T_{solar} = 90\%$ at $t = 2$ nm where $R_s = 8$ Ω/sq.

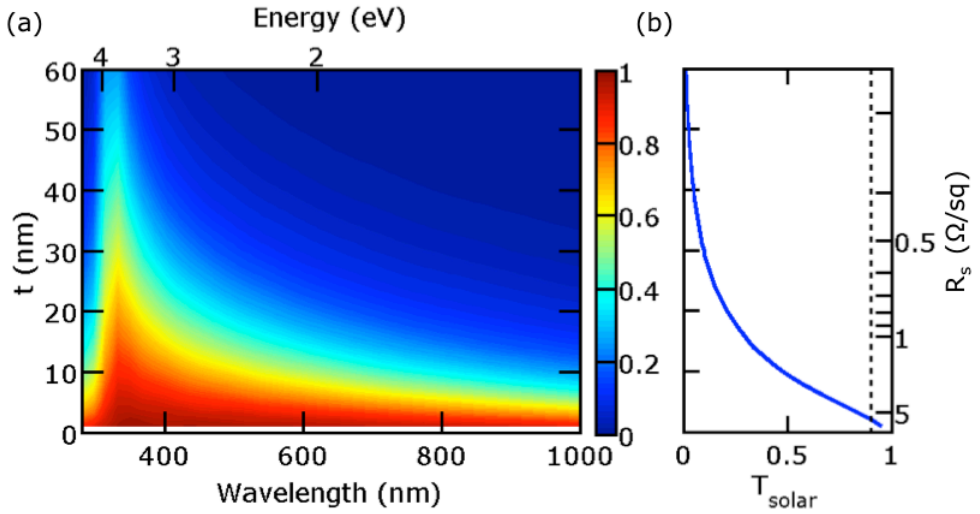

Figure 2: (a) Transmission of different silver thin film thicknesses t for wavelengths $\lambda = 280$ to 1000 nm. (b) T_{solar} across the wavelengths shown for different thicknesses with the sheet resistance R_s labelled on the right y-axis. The y-axis in (b) is the same as in (a).

In order to compare the transmission properties of 1D ordered NW arrays with thin films, we evaluated the transmission characteristics of traverse electric (TE)-polarized and traverse magnetic (TM)-polarized incident light. The electric field is parallel to the axes of the NWs for TE-polarized incident light and perpendicular for TM. Figure 3(a) plots $T(\lambda)$ as a function of diameter with $a = 600$ nm for TE-polarized incident light. The transmission has a small peak at 326 nm for the same reasons as the Ag thin film discussed above. The transmission exhibits evanescent behavior except when propagating modes are supported between the Ag NWs.

Due to the translational symmetry of the NW array as well as the mirror symmetry, these propagating modes occur when $k_0 \pm k_0 \sin\theta = 2\pi m/a$, where k_0 is the free space wave-vector, m is the mode number and a positive integer, and θ is the incident angle. Equivalently, this can be expressed as

$$\lambda = a(1 \pm \sin\theta)/m. \tag{3.2}$$

For normal-incident light ($\theta = 0$), the propagating modes exist at $\lambda = a/m$.

Due to these propagating resonant TE modes, NW arrays have higher T_{solar} for TE-incident light compared to thin films at the same R_s as shown in Fig. 3(b). $R_s = 4\rho_{bulk}a/\pi d^2$ for 1D Ag NW arrays. $T_{solar} = 90\%$ at $d = 90$ nm and $a = 600$ nm where $R_s = 1.5\ \Omega$/sq. Figure 3(c) shows the electromagnetic field of the doubly-degenerate TE_1 and TE_2 modes under normal incidence in these Ag NW arrays. At these wavelengths, there is an enhanced electromagnetic field surrounding the NWs leading to high transmission. These propagating modes begin to be cut off when $d > \lambda/2$ as the electromagnetic wave is unable to concentrate completely in the space around the NWs.

Figure 4(a) shows the angular dependence of propagating TE modes for 1D Ag NW arrays with $a = 600$ nm and $d = 80$ nm. $R_s = 1.9\ \Omega$/sq. These modes are labelled with subscripts based on the mode number and $\pm$ in Eq. 3.2. The propagating modes are singly degenerate, except at the center of each Brillouin zone where $k_x = m2\pi/a$ and at the edges of the Brillouin zone where $k_x = (m + 1/2)2\pi/a$. High transmission occurs at the propagating modes for TE-incident light. Other than these propagating modes, the electric field is evanescent at higher angles and thus T_{solar} decreases at higher angles as shown in Fig. 4(b). $T_{solar} = 91\%$ at normal incidence and drops below 90% at angle of 11°.

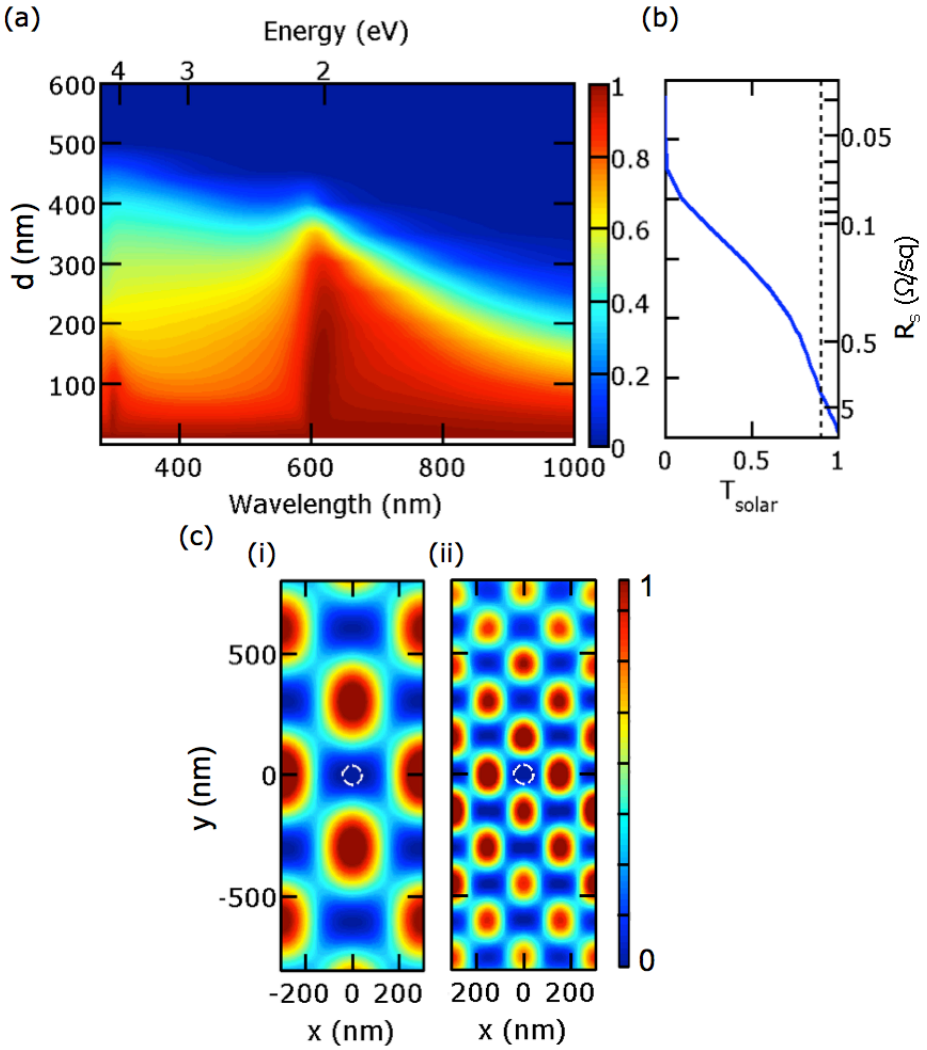

Figure 3: Transmission characteristics of Ag NW arrays for TE-incident light for $a = 600$ nm. (a) Contour plot of T as a function of wavelength and NW diameter d. (b) T_{solar} over the wavelength range shown with the sheet resistance R_s shown in the right y-axis. (c) Electric field intensity $|E|^2$ for (i) TE_1 mode at $\lambda = 600$ nm and (ii) TE_2 mode at $\lambda = 300$ nm with $d = 80$ nm where the edge of the NW is shown with a dashed white line.

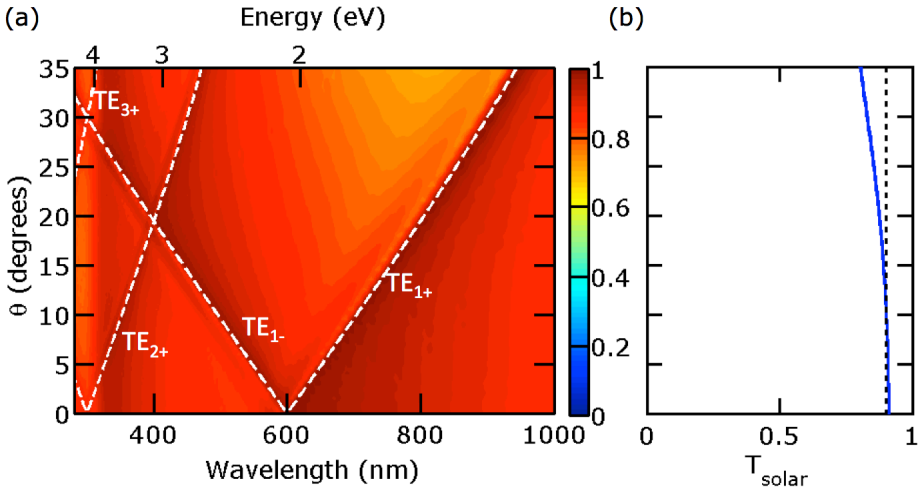

Figure 4: Angular-dependence of Ag NW arrays transmission for TE-incident light for $a =$ 600 nm and $d = 80$ nm. (a) Contour plot of T as a function of wavelength and incident angle θ. (b) T_{solar} over the wavelength range with the same y-axis as in (a).

The TM transmission spectrum is shown in Fig. 5(a). Near $\lambda = 340$ nm for all NW arrays, there is a dip in the transmission spectrum due to enhanced absorption. This absorption is mostly independent of the Ag NW diameter and due to the excitation of the surface plasmon of the silver, which can also be excited in thin films under non-normal TM incidence.[98] The dispersion relation of the TM modes are the same as those of the TE modes with one important difference–the existence of a TM_0 mode. The TE_0 mode does not exist because $E_z = 0$ everywhere in order to satisfy the boundary conditions of $E_z = 0$ at the NW surface. In contrast, there exists a TM_0 mode which does not have a cutoff wavelength. This mode is a TEM mode since both the electric and magnetic field are transverse. It is a direct transmission process where the incident energy goes straight through the NWs. This propagating mode is responsible for enhanced transmission in metallic nanoslits, regardless of how small these nano slits are.[99–101] From our contour plot, it was noted that when the TM_0 mode is the only mechanism for enhanced transmission, the transmission resonance peak is where the NW diameter is about half of the wavelength. Under these conditions, the magnetic field can concentrate in the space between the NWs allowing for high transmission.

There are thus, two mechanisms for enhanced transmission in Ag NW arrays under TM-incident light: direct transmission from a TM_0 mode and indirect propagating $TM_{m\pm}$ modes. T_{solar} is plot for the different diameter NW arrays shown in Fig. 5(b) and tends to be higher than that for TE-incident light due to the TM_0 mode. $T_{solar} = 90\%$ at $d = 120$ nm and $a = 600$ nm where $R_s = 0.8\ \Omega$/sq. The indirect TM propagating modes occur simultaneously with surface plasmon polariton (SPP) modes. Due to the periodic structure of the NWs, surface plasmon polaritons can couple to incident light when $k_{SPP} = k_0 \sin\theta \pm m\frac{2\pi}{a}$, where m is a positive integer. The real part of the H_z field patterns at $\lambda = 589$ nm and 300 nm are shown in Fig. 5(c) and (d) respectively for (i) 50 and (ii) 200 nm diameter NWs. For small diameter NWs such as the 50 nm illustrated, the transmission is primarily due to direct transmission through the TM_0 mode. For larger diameter NWs, the incident light couples more strongly to the indirect propagating modes. Due to interference between the two mechanisms for transmission at larger wavelengths, the transmission behavior exhibits Fano-type resonances with characteristic asymmetric peaks preceded by sharp dips.[102] For 200 nm diameter Ag NWs, the dip in the transmission spectra at 589 nm and 300 nm result from interference between the TM_0 mode and TM_1 mode (Fig. 5cii) and the TM_2 mode (Fig. 5dii), respectively.

In Fig. 6, we plot the angular dependence of the transmission of 1D Ag NW arrays with $a = 600$ nm and $d = 80$ nm under different incidence angles for TM-polarized light. The transmission is high across the spectrum due to the TM_0 transmission pathway. The distinct dip in transmission near $\lambda = 340$ nm is due to the excitation of surface plasmons and independent of incidence angle. Enhanced absorption is associated with the surface plasmon. The dispersion relation of the TM modes, where the modes are again labelled with subscripts based on Eq. 3.2, is identical to that of the TE modes. For low incident angles the transmission is high across the spectrum as transmission is primarily due to the TM_0 mode for this small diameter NW array, but at higher angles the indirect transmission pathways become more important such that Fano resonances start to become evident. $T_{solar} = 96\%$ at normal incidence and at incidence angles up to 35°.

Figure 7(a) shows T_{solar}, averaged for TE and TM polarization for different 1D NW array sheet resistances R_s. $T_{solar} = 90\%$ and $R_s = 10\ \Omega$/sq are shown with dashed black lines,

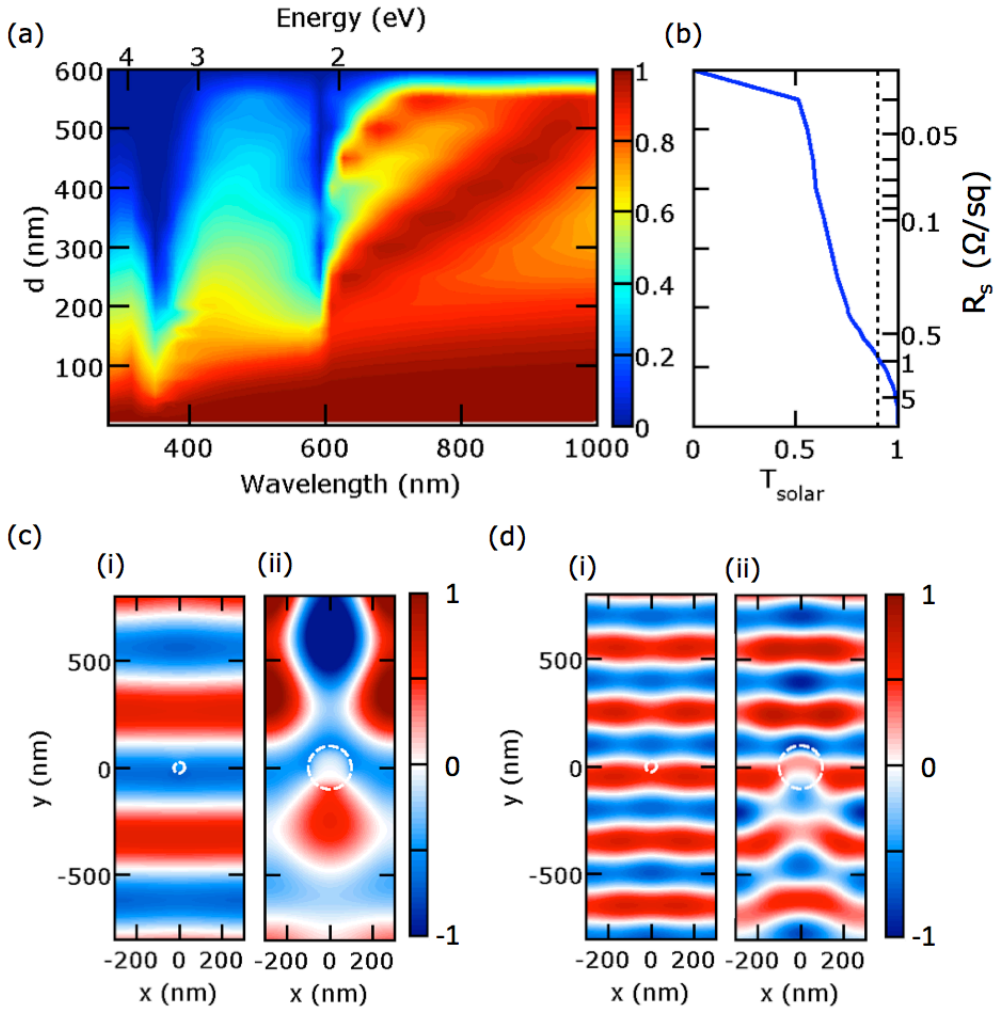

Figure 5: Transmission characteristics of Ag NW arrays for TM-incident light for $a = 600$ nm. (a) Contour plot of T as a function of wavelength and NW diameter d. (b) T_{solar} over the wavelength range shown with the same y-axis as in (a) and the sheet resistance R_s shown in the right y-axis. (c) Real part of H_z at $\lambda = 589$ nm for (i) 50 and (ii) 200 nm diameter Ag NWs. (d) Re(H_z) at $\lambda = 300$ nm for (i) 50 and (ii) 200 nm diameter Ag NWs.

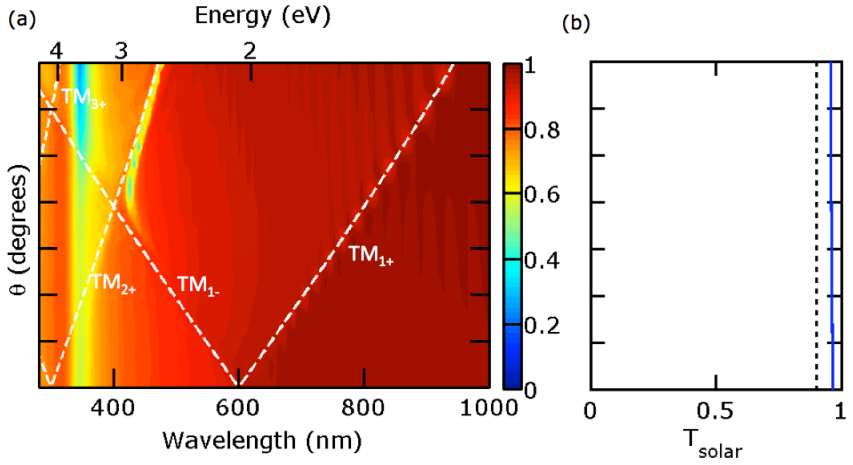

Figure 6: Angular-dependence of Ag NW arrays transmission for TM-incident light for $a = 600$ nm and $d = 80$ nm. (a) Contour plot of T as a function of wavelength and incident angle θ. (b) T_{solar} over the wavelength range with the same y-axis as in (a).

since both $T_{solar} \geq 90\%$ and $R_s \leq 10\ \Omega$/sq are important for transparent conductors in thin film solar cells.[3] Different diameter NWs are represented by different color markers, and the pitch is indicated by the size of the marker. The curves show clear trends for solar transmission as a function of diameter d and pitch a. For the same R_s, NW arrays with larger diameter at the appropriate pitch have higher T_{solar}. This is because R_s decreases with $1/d^2$ while transmission decreases approximately proportional to d. It can also be seen from this figure that NW arrays are superior to thin films as they can achiever higher T_{solar} for the same R_s.

To further compare the performance of different Ag NW array geometries for transparent electrodes, we plot in Fig. 7(b) the commonly used figure of merit for transparent electrodes σ_{DC}/σ_{op}[90] as a function of R_s where σ_{DC} is the DC conductivity of the material and σ_{op} is the optical conductivity. Higher values for this figures of merit indicate better performance. This figure of merit arises from $T_{solar} = \left(1 + \frac{Z_0}{2R_s}\frac{\sigma_{op}}{\sigma_{DC}}\right)^{-2}$, where $\mathrm{Z_0} = 377\ \Omega$ is the free space impedance.

This plot of figure of merit further demonstrates the improved performance of Ag NW arrays over silver thin films as well as the improved performance of larger diameter NWs

over smaller diameter NWs. In addition, these figures of merit allow for comparison between a wide range of materials and demonstrate that ordered Ag NW arrays have the potential to exceed what has been currently fabricated experimentally. Random films of Ag NWs have exhibited $\sigma_{DC}/\sigma_{\text{op}}$ of about 500[16] compared to about 0.5 for graphene thin films[68] and about 30 for random carbon nanotube meshes.[103] Our simulations indicate $\sigma_{DC}/\sigma_{\text{op}} > 1000$ may be achievable in ordered Ag NW arrays.

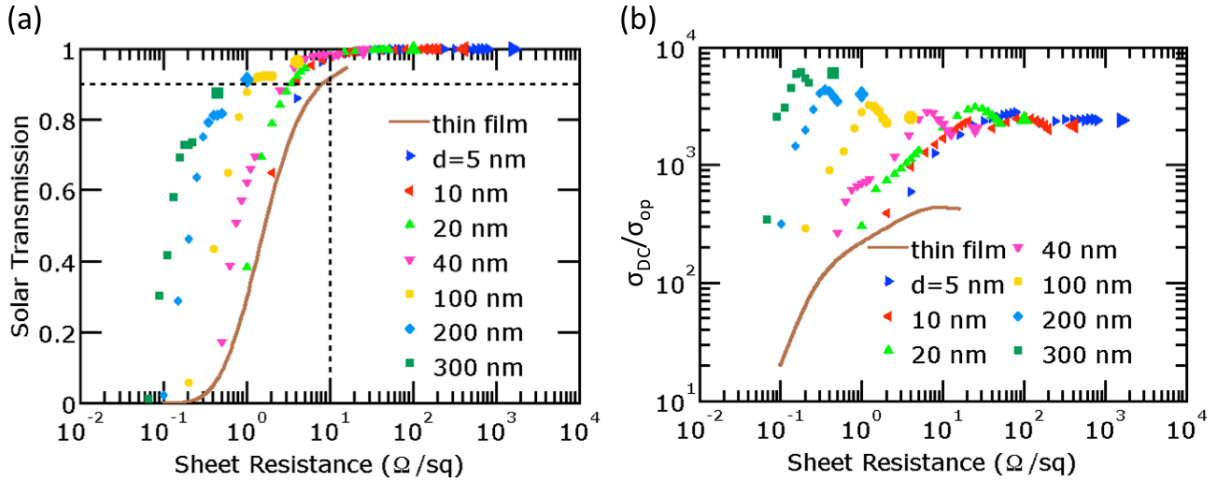

Figure 7: (a) T_{solar} versus R_{s} and (b) σ_{DC}/σ_{op} for 1D Ag NWs with different diameters d. T_{solar} is the average of TE and TM-polarized incident light. The marker size is proportional to the pitch a of the NW array from 10 to 2000 nm. The pitches shown are from 10 to 100 nm in 10 nm increments, 100 to 1000 nm in 100 nm increments and 2000 nm. $a \geq d$.

Finally, we performed simulations of 2D Ag NW square arrays. We compared T_{solar} averaged for both TE and TM-polarized incident light for 1D Ag NW arrays with T_{solar} for 2D Ag NW arrays and found that they agree well with one another. 2D NW arrays can be viewed as the two 1D NW arrays intersecting one another at 90°, and thus the transmission spectrum of 2D NW arrays are approximately the same as that for both TE and TM-incident light averaged together. We also performed finite element analysis to obtain the sheet resistance R_s for 2D Ag NW arrays, which cannot be derived analytically. The R_s for 2D NW arrays are only slightly lower than the 1D NW arrays of the same d and a. In Fig. 8, we plot (a) T_{solar} versus R_s for 2D NW arrays and (b) σ_{DC}/σ_{op} versus R_s. The plots are approximately the same as that in Fig. 7, though T_{solar} and R_s are both slightly lower.

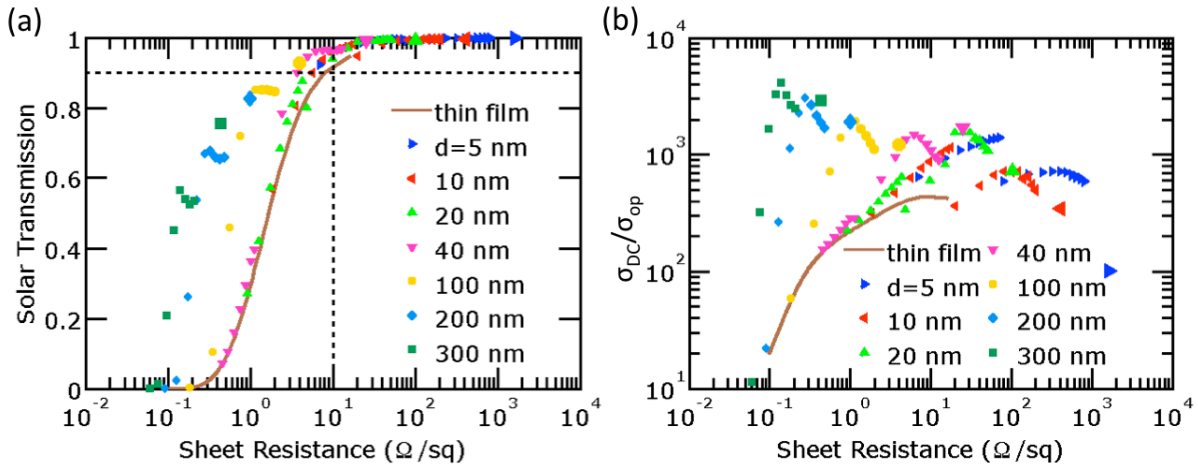

Figure 8: (a) T_{solar} versus R_s and (b) σ_{DC}/σ_{op} for 2D Ag NW arrays with different diameters d. The marker size is proportional to the pitch a of the NW array from 10 to 2000 nm. The pitches shown are from 10 to 100 nm in 10 nm increments, 100 to 1000 nm in 100 nm increments and 2000 nm. $a \geq d$.

3.1.3 Conclusions

Silver thin films and 1D and 2D silver NW arrays with a broad range of geometries were investigated as transparent electrodes. The enhanced transmission in Ag NW arrays is due to indirect propagating modes between the NWs. For TE-incident light, 1D NWs have enhanced transmission due to these propagating modes. For TM-incident light, enhanced transmission occurs through direct and indirect propagating modes. When the transmission is primarily through the direct TM_0 mode, there is enhanced transmission, but when both direct and indirect mechanisms are present, asymmetric Fano resonances are observed. These indirect propagating modes are assisted by surface plasmon polaritons. Superior optoelectronic performance was shown for NW arrays, which are able to achieve higher T_{solar} for a given R_s. Higher σ_{DC}/σ_{op} may be achieved in NW arrays over thin films and higher σ_{DC}/σ_{op} may be achievable in ordered NW arrays over current experimental results.

3.2 COPPER NANOWIRE ARRAYS

With the previous results for Ag NW arrays, we continue the work by using simulation methods to study of the optical and electrical properties of 1D and 2D Cu NW arrays of circular cross-section with diameters from 5 to 400 nm and pitches from 5 to 2000 nm. These structures should correspond well to experimentally fabricated Cu NWs with long lengths or could be fabricated by other means such as nanoimprint or electron beam lithography. We compare these results to that of Cu thin films and Ag NW results.[80] The angular dependence and dispersion relation of propagating modes are discussed. The electrical and optical performance of various structures are compared and general design principles are elucidated. In addition, we perform simulations on 1D Cu/Ni core-shell NWs, where the Ni shell prevents the Cu from oxidation. We evaluate the performance of these core-shell NWs for transparent electrodes.

3.2.1 Schematic and Methodology

Figure 9 shows the schematic of the different transparent conductor systems we studied: (a) Cu thin films defined by thickness t, (b) 1D Cu NW arrays with diameter d and pitch a, and (c) 2D Cu NW arrays. The 2D Cu NW arrays are also defined by the diameter d and the pitch a of the square lattice. Cu thin films of thicknesses $t = 1$ to 158 nm were studied, and Cu NW arrays with NW diameter range from $d = 5$ to 400 nm and pitches a from 5 to 2000 nm with $d \leq a$ were investigated.

The optical properties were determined by solving Maxwell's questions using the finite difference time domain (FDTD) method.[91, 92] The optical constants for Cu were taken from experimental measurement results in *CRC Handbook of Chemistry and Physics*.[97] A non-uniform simulation mesh with a finer mesh near interfaces and larger mesh in bulk regions was utilized.

Perfectly matched layer boundary conditions were used for the upper and lower boundary of the simulation cell,[94] while appropriate periodic boundary conditions were used for the side boundaries to model the periodic nature of the arrays. To study the performance of

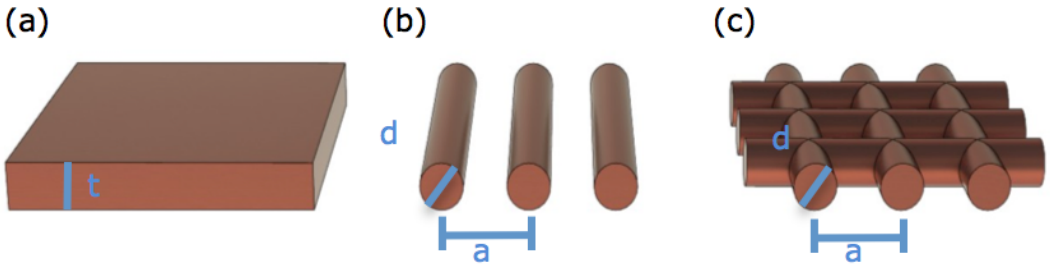

Figure 9: Schematic of structures studied: (a) Cu thin film with thickness t, (b) 1D Cu NW array with pitch a and the diameter d, and (c) 2D Cu NW array.

these different structures as transparent conductors, the solar integrated transmission was calculated from

$$T_{solar} = \frac{\int b(\lambda)T(\lambda)d\lambda}{\int b(\lambda)d\lambda} \tag{3.3}$$

where λ is the free-space wavelength, $b(\lambda)$ is the photon flux density, and $T(\lambda)$ is the optical transmission for light with wavelength λ. We considered the wavelength range $\lambda = 280$ to 1000 nm of the global 37° tilt AM1.5 solar spectrum.[95]

3.2.2 Results and Discussion

Figure 10(a) illustrates a contour plot of $T(\lambda)$ for Cu thin films of thickness t. At larger wavelengths, photons are governed by free electron-like behavior as governed by the Drude model. Almost all of the incident light is reflected since the real part of the index of refraction is small and $R(\lambda) = |(n(\lambda) - 1) / (n(\lambda) + 1)|^2$ where $n(\lambda)$ is the complex index of refraction of Cu and the index of refraction of air is 1. Below 590 nm (above 2.1 eV), interband transitions from d electrons to the Fermi surface start to become important. [104] The plasma frequency of the free electrons in Cu is about 130 nm (9.3 eV) and thus, photons across the entire solar spectrum range cannot propagate in Cu.[104]

Cu thin films only support evanescent modes, just like Ag thin films do, where the electromagnetic field intensity decays exponentially from the front surface. The transmission in films is described by the skin depth, where transmission is possible when t is comparable

or smaller than the skin depth. The skin depth of Cu is over 20 nm for most of the spectral range of interest and has a maximum at the 570 nm wavelength. Figure 10(b) plots T_{solar} with the same y-axis as in (a) with R_s shown on the right y-axis. $R_s = \rho_{Cu}/t$ where the bulk Cu resistivity $\rho_{Cu} = 1.68 \times 10^{-8}$ Ω·m.[97] Because the transmission is evanescent in Cu thin films, T_{solar} rapidly decreases with increasing thickness. Cu thin films have T_{solar} = 91% at $t = 1$ nm where $R_s = 16.8$ Ω/sq and $T_{solar} = 80\%$ at $t = 3$ nm where $R_s = 5.6$ Ω/sq. In contrast, Ag thin films have $T_{solar} = 95\%$ at $t = 1$ nm where $R_s = 15.8$ Ω/sq and $T_{solar} = 85\%$ at $t = 3$ nm where $R_s = 5.3$ Ω/sq.[80] Both $T_{solar} \geq 90\%$ and $R_s \leq 10$ Ω/sq are important for transparent conductors in thin film solar cells,[3] but Cu thin films cannot simultaneously achieve both figures of merit.

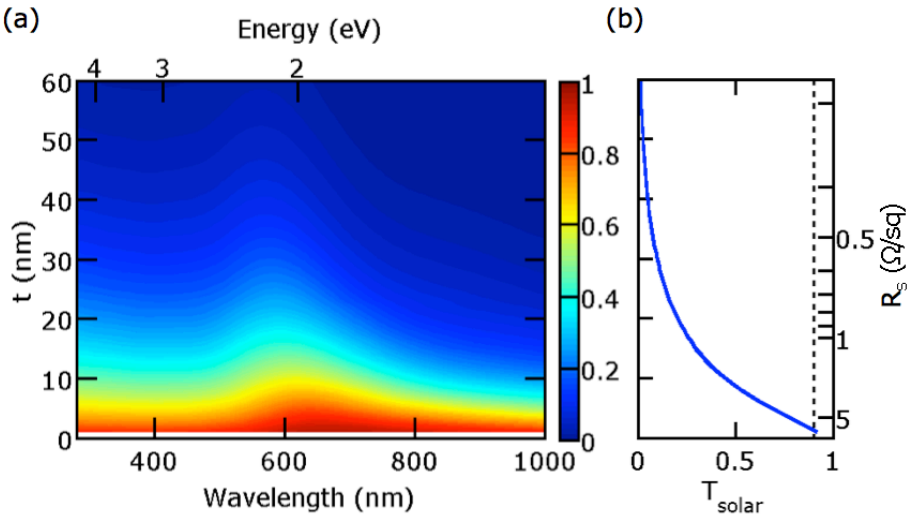

Figure 10: (a) Transmission of different Cu thin film thicknesses t for wavelengths $\lambda = 280$ to 1000 nm. (b) T_{solar} across the wavelengths shown for different thicknesses with the sheet resistance R_s labelled on the right y-axis. The y-axis in (b) is the same as in (a).

To compare the transmission properties of 1D ordered NW arrays with thin films, we evaluated the transmission characteristics of TE-polarized and TM-polarized incident light. The electric field is parallel to the axes of the NWs for TE-polarized incident light and perpendicular for TM. Fig. 11(a) plots $T(\lambda)$ as a function of diameter with $a = 600$ nm for TE-polarized incident light. The transmission exhibits evanescent behavior except when

propagating modes are supported between the Cu NWs. Due to the translational symmetry of the NW array as well as the mirror symmetry, these propagating modes occur when $k_0 \pm k_0 \sin\theta = 2\pi m/a$, where k_0 is the free space wave-vector, m is the mode number and a positive integer, and θ is the incident angle. Equivalently, this can be expressed as

$$\lambda = a(1 \pm \sin\theta)/m. \tag{3.4}$$

For normal-incident light ($\theta = 0$), the propagating modes exist at $\lambda = a/m$. Due to these propagating resonant TE modes, NW arrays have higher T_{solar} for TE-incident light compared to thin films at the same R_s as shown in Fig. 11(b). The sheet resistance of 1D Cu NW arrays is defined by $R_s = 4\rho_{Cu}a/\pi d^2$. Cu NWs have $T_{solar} = 90\%$ at $d = 80$ nm and $a = 600$ nm where $R_s = 2\ \Omega$/sq. For the same geometry, Ag NWs have $T_{solar} = 91\%$, $R_s = 1.9\ \Omega$/sq. The dispersion relation of propagating modes is independent of the dielectric properties of the metal, and thus the optical transmission of Cu NW arrays is almost the same as that of Ag NW arrays. The sheet resistance is also comparable since the conductivity of Cu is about 95% that of Ag. Fig. 11(c) shows the electromagnetic field of the doubly-degenerate TE_1 and TE_2 modes under normal incidence in these Cu NW arrays. At these wavelengths, there is an enhanced electromagnetic field surrounding the NWs leading to high transmission. These propagating modes begin to be cut off when $d > \lambda/2$ as the electromagnetic wave is unable to concentrate completely in the space around the NWs.

Fig. 12(a) shows the angular dependence of propagating TE modes for 1D Cu NW arrays with $a = 600$ nm and $d = 80$ nm. $R_s = 1.9\ \Omega$/sq. These modes are labelled with subscripts based on the mode number and $\pm$ in Equation 3.4. The propagating modes are singly degenerate, except at the center of each Brillouin zone where $k_x = m2\pi/a$ and at the edges of the Brillouin zone where $k_x = (m + 1/2)2\pi/a$. High transmission occurs at the propagating modes for TE-incident light. Other than these propagating modes, the electric field is evanescent at higher angles and thus T_{solar} decreases at higher angles as shown in Fig. 12(b). $T_{solar} = 89\%$ at normal incidence and is 78% at 35°. Fig 12(b) also shows our results for 1D Ag NW arrays under TE incident light, where the original plot has been corrected.[80] For Ag NW arrays under TE-incident light, $T_{solar} = 91\%$ at normal incidence and this drops below 90% at an incidence angle of 11.5° and is 80.5% at 35°.[80]

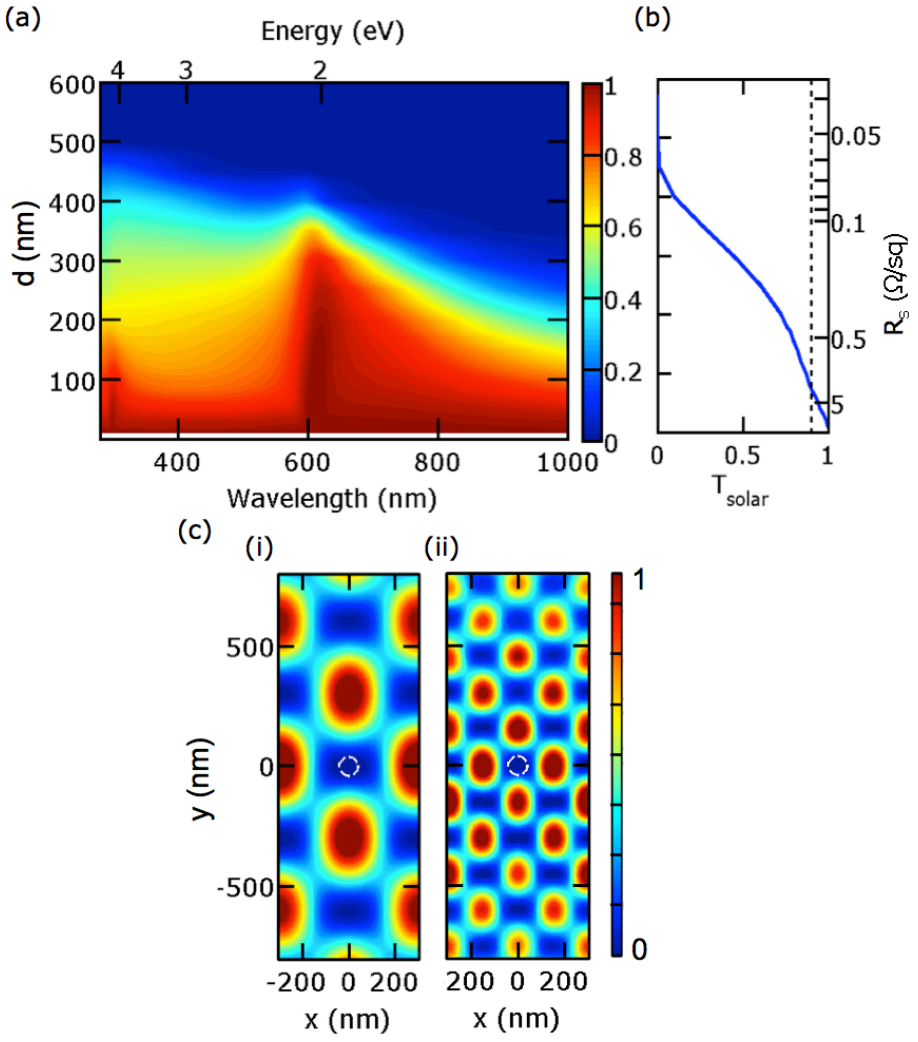

Figure 11: Transmission characteristics of Cu NW arrays for TE-incident light for $a = 600$ nm. (a) Contour plot of T as a function of wavelength and NW diameter d. (b) T_{solar} over the wavelength range shown with the sheet resistance R_s shown in the right y-axis. (c) Electric field intensity $|E|^2$ for (i) TE_1 mode at $\lambda = 600$ nm and (ii) TE_2 mode at $\lambda = 300$ nm with $d = 80$ nm where the edge of the NW is shown with a dashed white line.

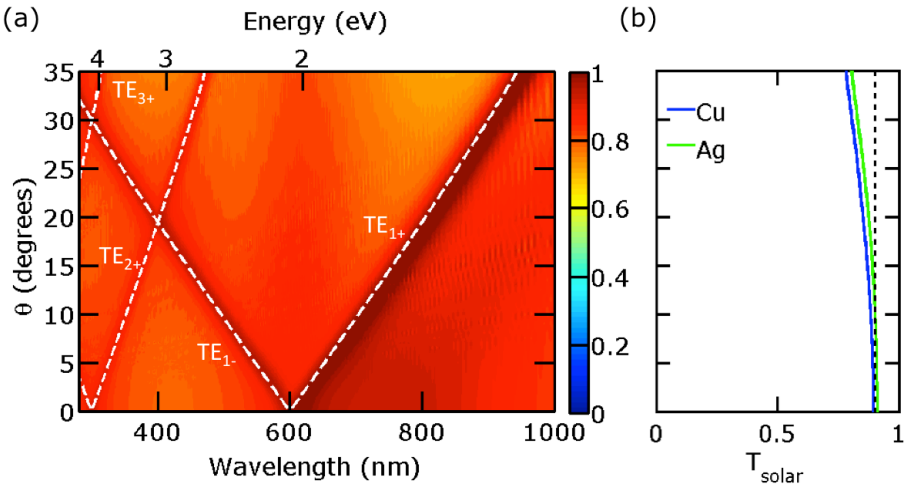

Figure 12: Angular-dependence of Cu NW arrays transmission for TE-incident light for $a = 600$ nm and $d = 80$ nm. (a) Contour plot of T as a function of wavelength and incident angle θ. (b) T_{solar} over the wavelength range with the same y-axis as in (a). Our Ag NW results are also shown for comparison.[80]

The TM transmission spectrum is shown in Fig. 13(a). As we discussed in our previous paper, the dispersion relation of the TM modes are the same as those of the TE modes, except with regards to the existence of a TM_0 mode.[80]

There are two mechanisms for enhanced transmission in Cu NW arrays under TM-incident light: direct transmission from a TM_0 mode and indirect propagating $TM_{m\pm}$ modes. T_{solar} is plot for the different diameter NW arrays shown in Fig. 13(b) and tends to be higher than that for TE-incident light due to the TM_0 mode. $T_{solar} = 90\%$ at $d = 110$ nm and $a = 600$ nm where $R_s = 1.1\ \Omega$/sq. The indirect TM propagating modes occur simultaneously with SPP modes. Due to the periodic structure of the NWs, surface plasmon polaritons can couple to incident light when $k_{SPP} = k_0 \sin\theta \pm m\frac{2\pi}{a}$, where m is a positive integer. The real part of the H_z field patterns at $\lambda = 589$ nm and 300 nm are shown in Fig. 13(c) and (d) respectively for (i) 50 and (ii) 200 nm diameter NWs. For small diameter NWs such as the 50 nm illustrated, the transmission is primarily due to direct transmission through the TM_0 mode. For larger diameter NWs, the incident light couples more strongly to the

indirect propagating modes. At larger wavelengths, Fano-type resonances with characteristic asymmetric peaks preceded by sharp dips is present due to interference between the two mechanisms for transmission.[102] For 200 nm diameter Cu NWs, interference between the TM_0 mode (Fig. 13cii) and TM_1 mode (Fig. 13dii) results in the dip in transmission spectra at 300 nm and 589 nm.

In Fig. 14, we plot the angular dependence of the transmission of 1D Cu NW arrays with $a = 600$ nm and $d = 80$ nm under different incidence angles for TM-polarized light. The transmission is high across the spectrum due to the TM_0 transmission pathway.

The dispersion relation of the TM modes, where the modes are again labelled with subscripts based on Equation 3.4, is identical to that of the TE modes. For low incident angles the transmission is high across the spectrum as transmission is primarily due to the TM_0 mode for this small diameter NW array, but at higher angles the indirect transmission pathways become more important such that Fano resonances start to become evident. $T_{solar} = 95\%$ at normal incidence and drops to only 94% at 35°. The transmission remains high due to the TM_0 mode. Fig 14(b) also shows our results for 1D Ag NW arrays under TM incident light, where the original plot has been corrected.[80] For Ag NWs, $T_{solar} = 96\%$ at normal incidence and remains at 96% at an incidence angle up to 35°.[80]

Fig. 15(a) shows a contour plot of the transmission spectrum of 2D Cu NW arrays for different diameters with pitch $a = 600$ nm. While the TEM mode no longer exists in 2D NW arrays,[100] enhanced transmission can still occur due to a propagating plasmonic HE_{11} mode in the space between the NWs.[99] Below $\lambda = 600$ nm, most of the loss is from absorption, while above $\lambda = 600$ nm, the loss is primarily from reflection. Fig. 15(b) shows T_{solar} with the same y-axis as in (a) and the sheet resistance R_s is shown on the right y-axis. The sheet resistances of 2D Ag NW arrays were calculated from finite element analysis. $T_{solar} \approx 90\%$ at $d = 70$ nm where $R_s = 2.6\ \Omega$/sq.

Fig. 16(a) shows T_{solar}, averaged for TE and TM polarization for different 1D NW array sheet resistances R_s. $T_{solar} = 90\%$ and $R_s = 10\ \Omega$/sq are shown with dashed black lines, since it is desirable for transparent conductors in thin film solar cells to have both $T_{solar} \geq 90\%$ and $R_s \leq 10\ \Omega$/sq.[3] Different diameter NWs are represented by different color markers, and the pitch is indicated by the size of the marker. The curves show clear trends for solar

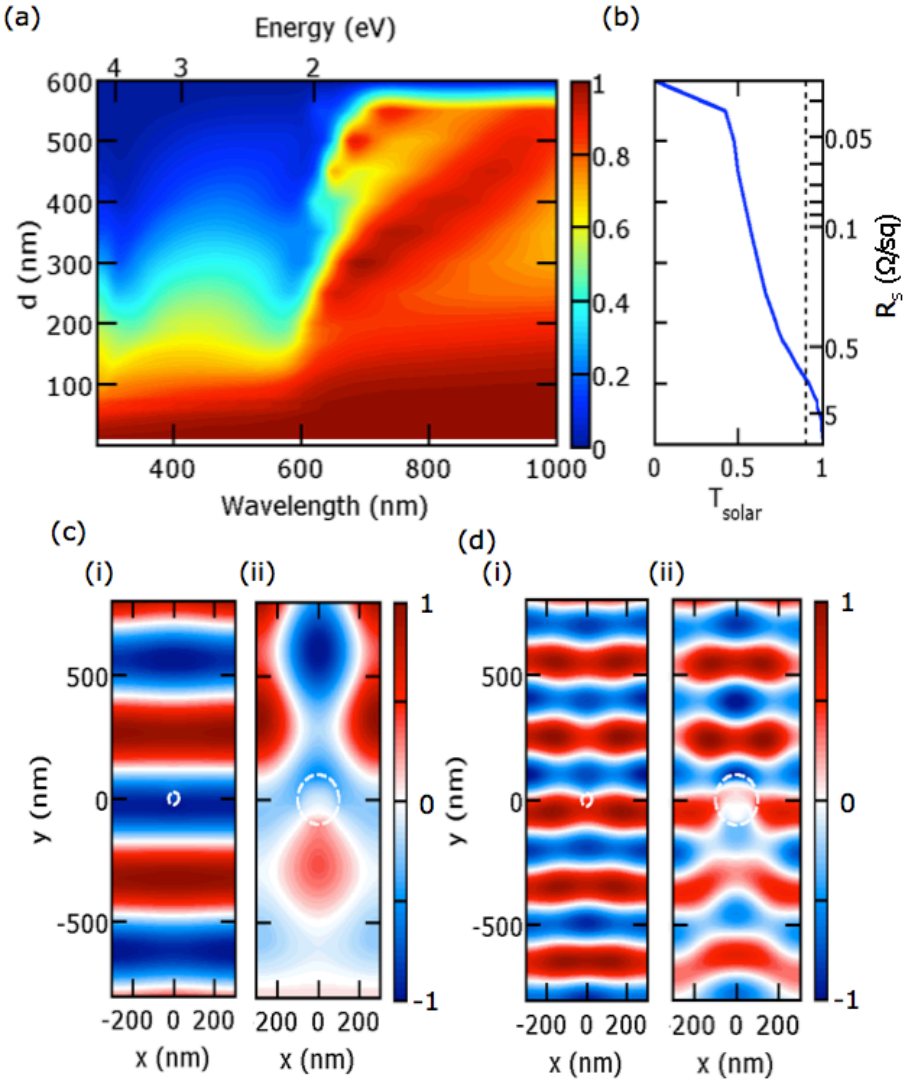

Figure 13: Transmission characteristics of Cu NW arrays for TM-incident light for $a = 600$ nm. (a) Contour plot of T as a function of wavelength and NW diameter d. (b) T_{solar} over the wavelength range shown with the same y-axis as in (a) and the sheet resistance R_s shown in the right y-axis. (c) Real part of H_z at $\lambda = 589$ nm for (i) 50 and (ii) 200 nm diameter Cu NWs. (d) Re(H_z) at $\lambda = 300$ nm for (i) 50 and (ii) 200 nm diameter Cu NWs.

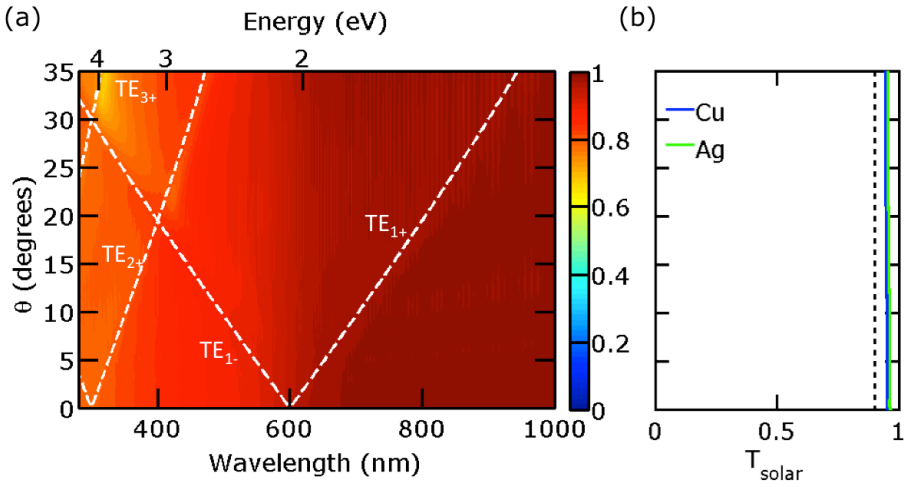

Figure 14: Angular-dependence of Ag NW arrays transmission for TM-incident light for $a = 600$ nm and $d = 80$ nm. (a) Contour plot of T as a function of wavelength and incident angle θ. (b) T_{solar} over the wavelength range with the same y-axis as in (a). Our corrected Ag NWNW results are also shown for comparison.[80]

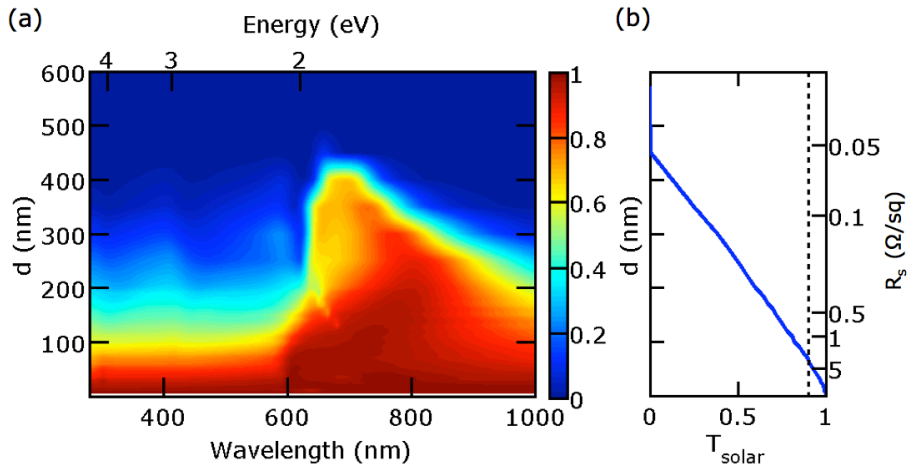

Figure 15: Transmission characteristics of 2D Cu NW arrays with $a = 600$ nm. (a) Contour plot of T as a function of wavelength and NW diameter d. (b) T_{solar} over the wavelength range shown with the sheet resistance R_s shown in the right y-axis.

transmission as a function of diameter d and pitch a. For the same R_s, NW arrays with larger diameter at the appropriate pitch have higher T_{solar}. This is because R_s decreases with $1/d^2$ while transmission decreases approximately proportional to d. NW arrays are superior to thin films as they can achiever higher T_{solar} for the same R_s. While Cu thin films are unable to achieve both $T_{solar} \geq 90\%$ and $R_s \leq 10\ \Omega$/sq, Cu NW arrays may satisfy both conditions across a range of diameters and pitches.

To further compare the performance of different Cu NW array geometries for transparent electrodes, we plot in Fig. 16(b) the commonly used figure of merit for transparent electrodes σ_{DC}/σ_{op}[90] as a function of R_s, where σ_{DC} is the DC conductivity of the material and σ_{op} is the optical conductivity,. Higher values for this figures of merit indicate better performance. This figure of merit arises from the equation $T_{solar} = \left(1 + \frac{Z_0}{2R_s}\frac{\sigma_{op}}{\sigma_{DC}}\right)^{-2}$, where $Z_0 = 377\ \Omega$ is the free space impedance. It is demonstrated by this figure of merit that Cu NW arrays have improved performance over Cu thin films and that larger diameter NWs have better performance over smaller diameter NWs. In addition, this figure of merit allows for comparison between a wide range of materials and demonstrate that ordered Cu NW arrays have the potential to exceed what has been currently fabricated experimentally. Random films of Ag NWs have exhibited $\sigma_{DC}/\sigma_{\text{op}}$ of about 500[16] compared to about 0.5 for graphene thin films[68] and about 30 for random carbon nanotube meshes.[103] Our simulations indicate $\sigma_{DC}/\sigma_{\text{op}} > 1000$ may be achievable in ordered Cu NW arrays. The results for Cu NW arrays are comparable to that of Ag NW arrays.[80]

In Fig. 17, we plot (a) T_{solar} versus R_s for 2D NW arrays and (b) σ_{DC}/σ_{op} versus R_s. The plots are approximately the same as that in Fig. 16, though T_{solar} and R_s are both slightly lower for the same geometry. σ_{DC}/σ_{op} is also slightly than when using the averaged T_{solar}. In the 2D case, both $T_{solar} \geq 90\%$ and $R_s \leq 10\ \Omega$/sq are achievable at the same time. Some NW configurations also exhibit $\sigma_{DC}/\sigma_{\text{op}} > 1000$.

We further evaluated the performance of Cu/Ni core-shell NWs for transparent electrodes. One of the challenges with the use of Cu for transparent electrodes is that a thin native oxide layer of about 5 nm forms on the surface upon exposure to the ambient for a few days. [105] This oxide layer reduces the electrical conductivity and renders less stable performance. To protect the Cu NWs from being oxidized, Rathmell *et al* fabricated core-

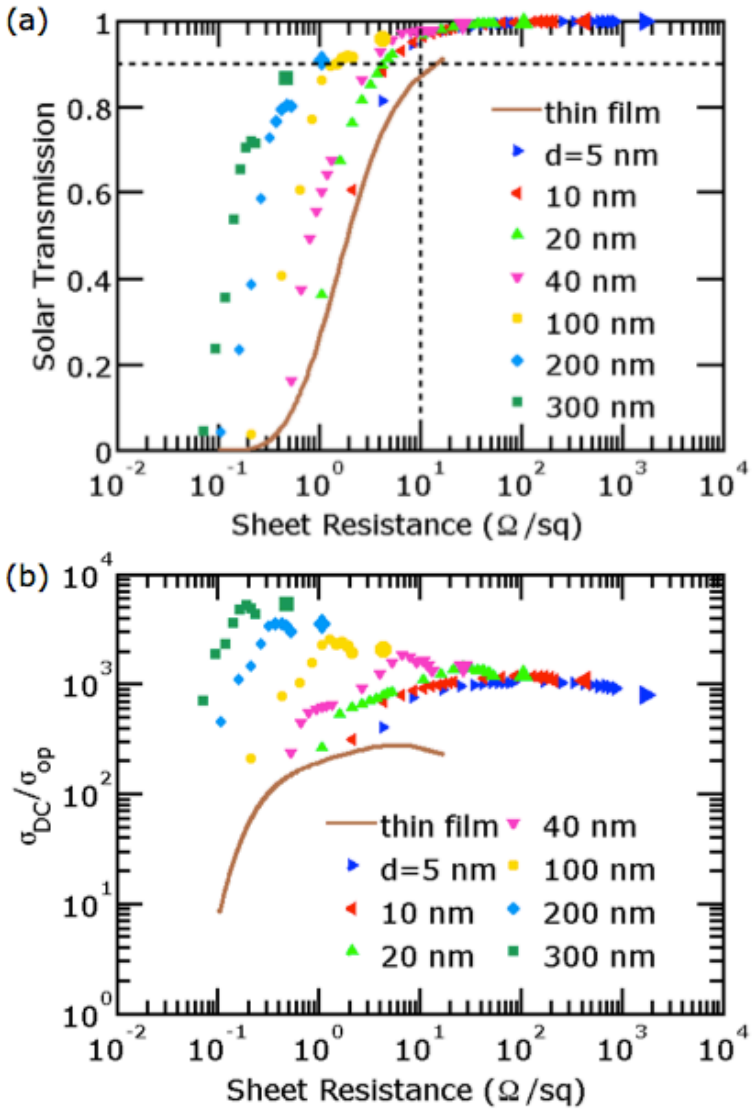

Figure 16: (a) T_{solar} versus R_s and (b) σ_{DC}/σ_{op} for 1D Cu NWs with different diameters d. T_{solar} is the average of TE and TM-polarized incident light. The marker size is proportional to the pitch a of the NW array from 10 to 2000 nm. The pitches shown are from 10 to 100 nm in 10 nm increments, 100 to 1000 nm in 100 nm increments and 2000 nm. $a \geq d$.

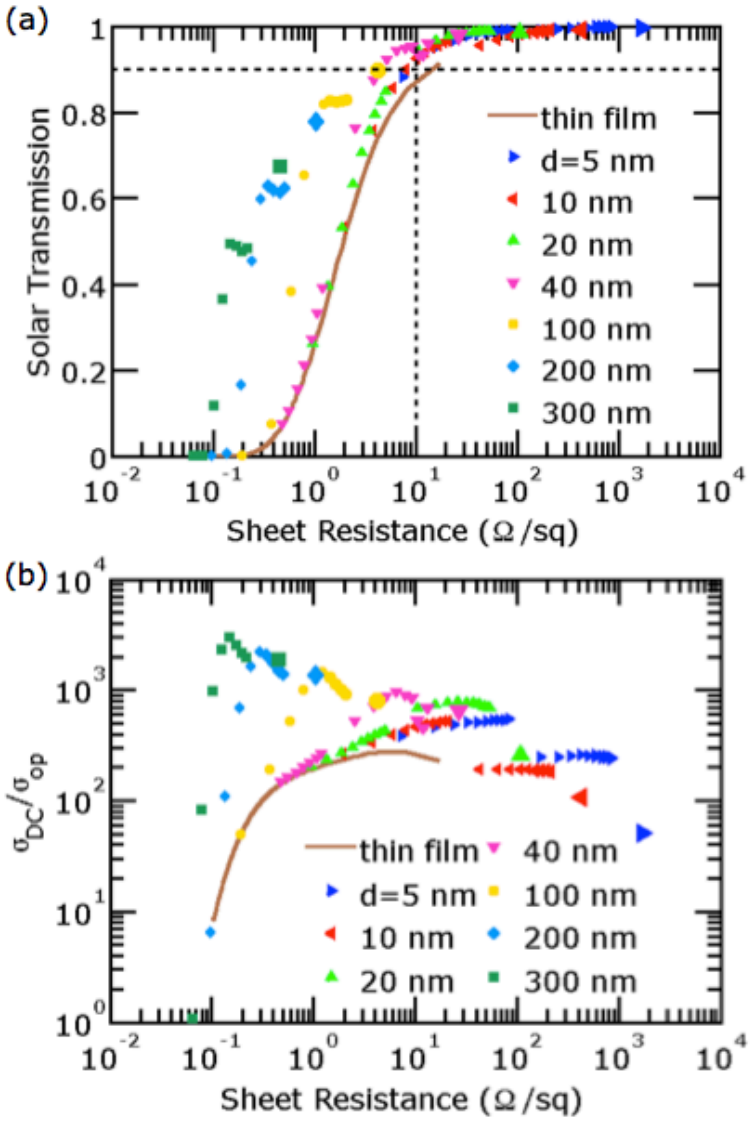

Figure 17: (a) T_{solar} versus R_s and (b) σ_{DC}/σ_{op} for 2D Cu NWs with different diameters d. The marker size is proportional to the pitch a of the NW array from 10 to 2000 nm. The pitches shown are from 10 to 100 nm in 10 nm increments, 100 to 1000 nm in 100 nm increments and 2000 nm. $a \geq d$.

shell NWs consisting of a Cu core and Ni shell where the thickness of the Ni coating can be tuned chemically. [77]

The geometry is shown in the inset of Fig. 18(a) where D is the total NW diameter, t is the Ni shell has thickness, and a is the NW pitch as before. The thickness of the Ni coating was fixed to be 10 nm. The sheet resistance can be expressed as $R_s = \frac{4\rho_{Cu}\rho_{Ni}a}{\pi\{\rho_{Ni}(D-2t)^2+\rho_{Cu}[D^2-(D-2t)^2]\}}$. The bulk resistivity for Ni is $\rho_{Ni} = 6.93 \times 10^{-8}$ Ω·m, which is more than four times larger than the bulk resistivity of Cu.[97]

Fig. 18 shows (a) T_{solar} versus R_s for and (b) σ_{DC}/σ_{op} versus R_s for the 1D Cu/Ni core-shell NW arrays. T_{solar} is averaged for TE and TM polarization. In comparison with the 1D Cu NW arrays in Fig. 16, the core-shell NW arrays have higher sheet resistance due to the Ni shell. This is especially pronounced in the smaller diameter core-shell NWs, where the shell is a larger fraction of the cross-sectional area. However, the transmission is about the same, since the transmission is mostly independent of the metal as discussed above. For $D = 40$ nm, $t = 10$ nm, and $a = 400$ nm, $T_{solar} = 90\%$ and $R_s = 12$ Ω/sq. For Cu NW arrays with $d = 40$ nm and $a = 400$ nm, $T_{solar} = 96\%$ and $R_s = 5.3$ Ω/sq. For Ag NW arrays of the same geometry, $T_{solar} = 97\%$ and $R_s = 5.0$ Ω/sq.[80] For $D = 100$ nm, $t = 10$ nm, and $a = 1000$ nm, $T_{solar} = 90\%$ and $R_s = 2.9$ Ω/sq. For Cu NW arrays with $d = 100$ nm and $a = 1000$ nm, $T_{solar} = 91\%$ and $R_s = 2.1$ Ω/sq. In contrast, for Ag NW arrays of the same geometry, $T_{solar} = 92\%$ and $R_s = 2.0$ Ω/sq.[80] Based on these results, the benefits of using Ni as an anti-oxidation coating can be seen in larger diameter NWs where performance is not sacrificed much.

3.2.3 Conclusions

We have performed simulations of 1D and 2D Cu NW arrays and compared their transmission and sheet resistance to that of Cu films and our recent Ag NW array results. Cu NW arrays exhibits enhanced transmission due to propagating modes between the NW arrays. These modes are independent of the metal, and thus, the solar transmission is approximately the same regardless of the metal for the same geometry. The Cu resistivity is also about the same as that of Ag, such that about the same sheet resistances are achievable. We also

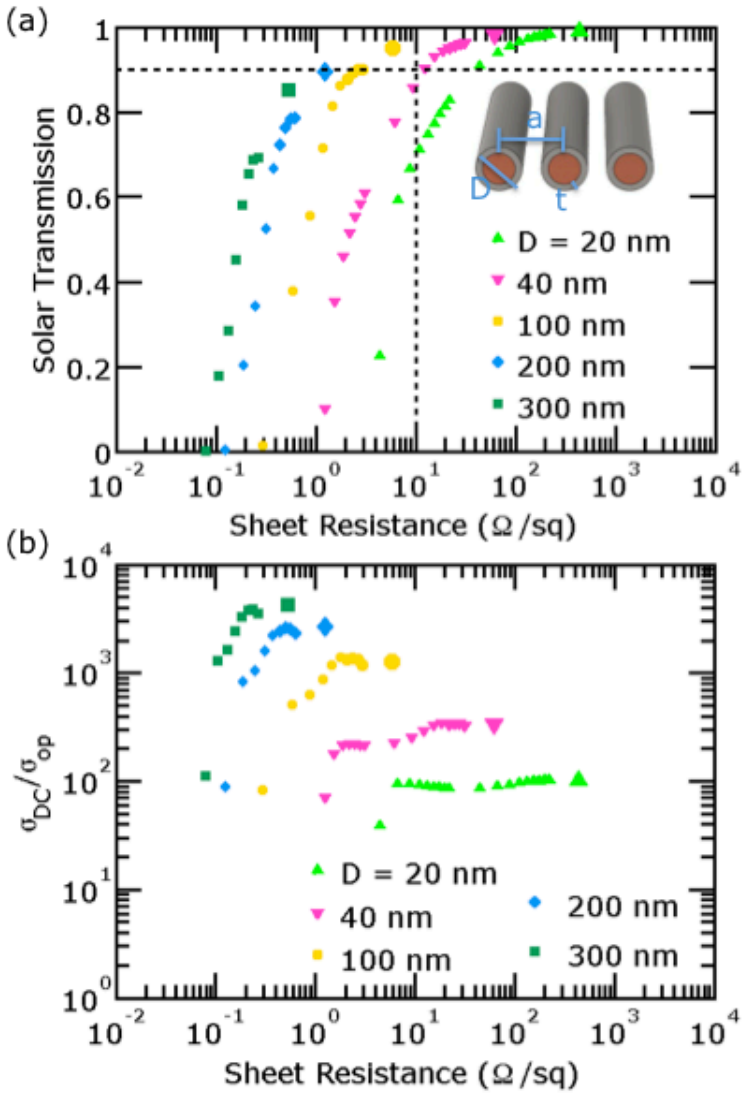

Figure 18: (a) T_{solar} versus R_s and (b) σ_{DC}/σ_{op} for 1D Ni Cu/Ni core-shell NWs with different total diameters D. The thickness of Ni coating t is 10 nm. The marker size is proportional to the pitch a of the NW array from 20 to 2000 nm. The pitches shown are from 20 to 100 nm in 10 nm increments, 100 to 1000 nm in 100 nm increments and 2000 nm. $a \geq D$. $D = 20$ nm indicates a Ni NW array with diameter of 20 nm (or $2t$).

investigated 1D Cu/Ni core-shell NW arrays as a system to address oxidation issues of Cu. The Ni shell degrades the sheet resistance, particularly in smaller NW arrays, but do not affect the transmission substantially.

4.0 COPPER NANOMESH FOR TRANSPARENT CONDUCTORS

As studied in the previous chapter, Ag NW films fabricated by solution-based methods have demonstrated superior optical transmission and sheet resistance compared to ITO films.[14, 16, 63] However, the abundance of Ag in the Earth's crust is comparable to that of In, and the price of Ag and In have been about the same over the past several years.

Cu is far more abundant than In and Ag, and its price is about two orders of magnitude lower[106]. Printable random Cu NW networks have been fabricated and have shown impressive optoelectronic properties comparable to ITO.[76, 77, 107] However, random Cu NW networks have several fabrication and performance disadvantages. The synthesis of printable metal NW solutions requires sophisticated solution processing to obtain high aspect ratio NWs.[63] Distinct chemistries must be utilized for synthesizing different metals. Percolation may also be a serious problem in these random structures. The density of the NWs must be above the percolation threshold to form a connected current pathway.[108] However, to achieve high transparency, the networks should be sparse, resulting in poor connectivity and high resistivity such that some nanomaterials are unusable for transparent electrodes. This is especially a problem at the contacts between NWs, where there is high contact resistance, and for Cu, which has a tendency to oxidize. As reported, random NW networks have been shown to fail from ohmic heating in short times.[109] The growth of long wires,[14] mechanical pressing,[14] plasmonic welding,[110] and surface passivation[77] have been alternatively proposed as means to reduce junction resistance. Recently, electrospun nanotroughs have been reported with transparencies of about 90% at 2 Ω/square[12] and random Au NMs prepared by grain boundary lithography have demonstrated 82.5% transmission at about 20 Ω/square.[79] However, these structures, like random NW networks, lack uniformity and ordering.

The ability to carefully control morphology with high uniformity and ordering are beneficial for many transparent conductor optoelectronic applications, but approaches such as electron beam lithography[111] are not scalable. Nanoimprint lithography has been demonstrated for fabricating metal gratings with high resolution and high throughput.[112] However, scalability is a challenge for this methodology since large contact areas between the mold and the imprinted nanostructures can result in sticking issues and pattern fidelity is poor over large areas since the polymer chains in the materials tend to elastically relax .[113] The nanoimprint mold must be patterned by unscalable methods such as electron beam lithography or focused ion beam, and the mold tends to wear with usage. Nanoimprint lithography is also unsuitable for directly fabricating nanostructures on flexible substrates due to the high pressure and temperatures required. While transfer printing methods have been adapted for these purposes,[114] it would nevertheless be advantageous to directly fabricate the transparent electrode onto the device. These imprinted Cu structures also have not performed as well as ITO as discussed below in Figure 19.

In this chapter, we propose both a simulation and experimental investigation of Cu NMs as TC material. The Cu NM consists of holes arranged in a hexagonal lattice in a Cu thin film. We perform electrodynamic simulations and transport simulations to show that Cu NMs may achieve higher optical transmission than ITO films at the same sheet resistance. We also demonstrate a low-cost approach for fabricating metal NMs by microsphere lithography, which is a fast and scalable method compatible with well-established wafer-scale photolithography processes.[115, 116] NMs may be fabricated over large areas with precise control over morphology and with high uniformity and order. The as-prepared transparent conductors should have a more uniform resistance and optical properties on the microscale compared with random networks of NWs. The NMs also have less hazy appearance due to reduced light scattering. Our methodology is versatile in that it may be used to fabricate NMs of any metal that may be deposited through standard evaporation processes. Metal NMs may be fabricated on both rigid or flexible substrates and the morphology may be carefully controlled for various plasmonic applications such as optical filters or sensors, or the formation of ohmic or Schottky barrier contacts for different optoelectronic devices. We demonstrate the fabrication of Cu NMs directly on both rigid quartz and flexible PET sub-

strates and determine that they have comparable performance to ITO films when fabricated on quartz, and slightly poorer performance on PET. In addition, we performed durability experiments to assess the performance of Cu NMs under various bending, heating, and abrasion conditions.

4.1 RESULTS AND DISCUSSION

Figure 19 plots the relationship between transmission and sheet resistance for a variety of transparent conductors. Our simulation data for Cu NMs is plot with red circles, and our experimental data on quartz and PET substrates is plot with blue squares and green diamonds respectively. Our transmission data is plot at the wavelength $\lambda = 550$ nm, which is near the middle of the visible spectrum. The effect of the substrates has been excluded. For comparison purposes, we plot simulation data for ITO thin films,[63] as well as the best experimental data in the literature for several alternative transparent conductors: electrospun Cu nanotroughs[12] and nanofibers,[117], nanoimprinted Cu gratings,[112] solution-coated random Cu NW networks,[76] solution-processed random Ag NW networks,[63] random Au NMs by boundary lithography,[79] dip-coated solution-processed double walled carbon nanotubes (DWNT) films,[51] and roll-to-roll synthesized and transferred graphene.[13]

The data shown for the random Ag NW networks[63] is the weighted average of the spectral transmission with the AM1.5 global photon flux over the wavelength range $\lambda = 400$ to 800 nm, and the data for the nanimprinted Cu gratings[112] is the average transmittance over the wavelength range $\lambda = 400$ to 800 nm. The rest of the data are shown for $\lambda = 550$ nm. Our simulation data predicts that Cu NMs may be more transmissive than ITO films for the same sheet resistance. Our experimental data demonstrates that Cu NMs fabricated on quartz substrates exhibit comparable performance to ITO films. More details about the simulations and experiments and differences in the results between the two will be discussed later in the text.

Figure 20 shows our simulation results. Figure 20(a) shows the schematic for the Cu NMs studied in simulations. The Cu NMs consist of a Cu thin film with holes in a hexagonal

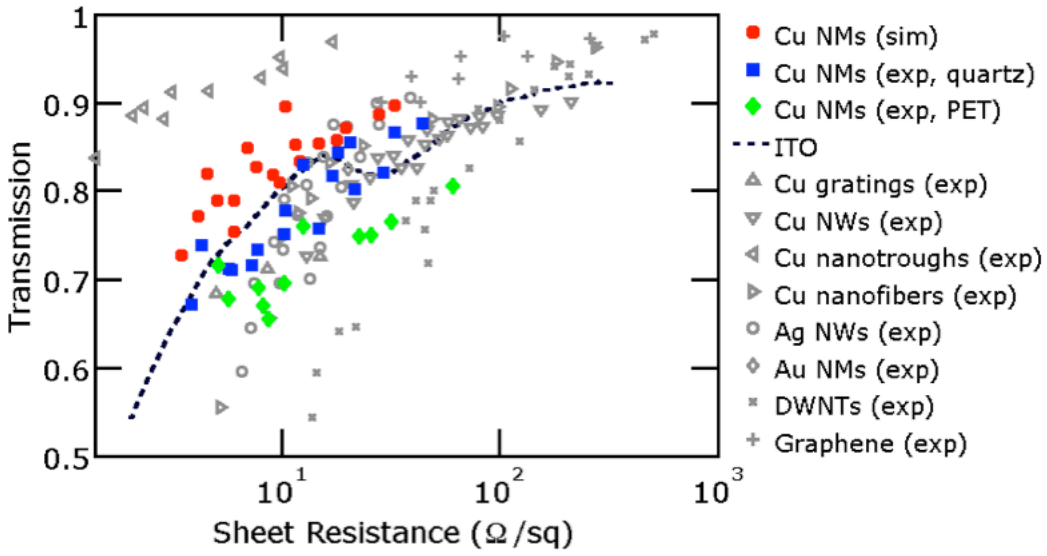

Figure 19: Transmission versus sheet resistance for various transparent conductors. Our Cu NM data is shown for simulations (red circles) and experimentally on quartz (blue squares) and PET (green diamonds) substrates at $\lambda = 550$ nm. The best data that the authors are aware of for ITO thin films[63], periodically perforated Cu gratings[112], Cu NWs[76], electrospun Cu nanotroughs[12], electrospun Cu nanofibers[117], Ag NWs[63], random Au NMs by boundary lithography[79], double walled carbon nanotubes (DWNTs)[51], and graphene[13] are also shown.

array. The primitive lattice vectors are $\vec{a}_1 = (a, 0)$ and $\vec{a}_2 = (\frac{a}{2}, \frac{\sqrt{3}}{2}a)$ with $|\vec{a}_1| = |\vec{a}_2| = a$ and $\varphi = 60°$. The morphology of Cu NMs are defined by the thickness of the Cu t, the pitch of the hexagonal array a, and the minimum width of the metal w between holes. The NM width is $w = a - d$, where d is the diameter of the holes. The transmission and sheet resistance of metal NMs is anisotropic, but invariant under 60° rotational transformations. We used finite difference time domain simulations to obtain the transmission spectra and finite element method simulations to determine the sheet resistances of these structures. The optical simulations utilized the refractive index for Cu from *CRC Handbook of Chemistry and Physics*[97] and the transport simulations assumed the Cu resistivity in the NMs is the bulk resistivity ($\rho_{Cu} = 1.68 \times 10^{-8}$ Ω·m).

For comparing different structures, we utilized the angle averaged transmission $T = \frac{1}{2}(T_{xx} + T_{yy})$ and angle averaged sheet resistance $R_s = \frac{1}{2}(R_{s,xx} + R_{s,yy})$ where T_{xx} and T_{yy} are the transmission for light polarized in the x- and y-directions respectively, and $R_{s,xx}$ and $R_{s,yy}$ are the sheet resistances in the x- and y-direction. NMs exhibit a six-fold symmetry and our simulations indicated very little dependence of transmission on polarization and sheet resistance on transport direction. Figure 20(b) shows a contour plot of the optical transmission for Cu NMs as a function of w between 50 and 120 nm and wavelength between 400 nm and 1000 nm. The pitch $a = 1300$ nm and the thickness $t = 20$ nm. The simulated angle averaged sheet resistances are shown on the right y-axis. The angle averaged sheet resistances range from $R_s = 6.0$ Ω/sq for $w = 120$ nm to $R_s = 11.5$ Ω/sq for $w = 50$ nm.

While other work has demonstrated extraordinary transmission for sub-wavelength holes at particular wavelengths due to surface plasmon modes[118] and propagating plasmonic modes,[119] the NMs in this work contain apertures with sizes greater than the wavelengths of interest, such that there is broadband transmission close to unity. The transmission spectra is primarily due to the excitation of propagating modes in the NM holes. Cylindrical holes in a perfect metal support propagating modes at wavelengths $\lambda \lesssim 2d$,[118] which covers the entire spectrum studied, since the smallest hole diameter studied was $d = 1180$ nm where $w = 120$ nm. A broadband transmission over 80% is achievable for $R_s \leq 10$ Ω/sq. In addition, surface waves are resonantly excited by the NMs when $\vec{k}_{spp}(\lambda_{mn}) = \vec{k}_{in,x} + m\vec{b_1} + n\vec{b_2}$ where $\vec{k}_{spp} = \frac{2\pi}{\lambda}\sqrt{\frac{\epsilon}{\epsilon+1}}$ is the wave vector of the surface plasmon polariton, $\vec{k}_{in,x}$ is the in-plane

component of the incident wave vector, ϵ is the permittivity of the Cu, and m and n are integers. The reciprocal lattice basis vectors are $\vec{b}_1 = \left(\frac{2\pi}{a}, -\frac{2\sqrt{3}\pi}{3a}\right)$ and $\vec{b}_2 = \left(0, \frac{4\sqrt{3}\pi}{3a}\right)$. For normal incidence light, SPPs are excited when $|\vec{k}_{spp}(\lambda_{mn})| = \frac{2\pi}{a}\sqrt{\frac{4}{3}(m^2 + n^2 - mn)}$. The lowered transparency at 650 nm is due to Fano interference between the two transmission pathways of propagating modes and the $(2,1), (1,2)$, or $(1,-1)$ SPP at $\lambda = 670$ nm.[102]

The dashed black line indicates the wavelength $\lambda = 550$ nm where the transmission was plotted in Figure 19. Figure 20(c) shows the electric field intensity at $\lambda = 550$ nm in the x-z plane passing though the center of the hole for a NM with $a = 1300$ nm, $w = 100$ nm, and $t = 20$ nm (indicated in Figure 20b with a black circle). The electric field intensity is shown for both light polarized in the (i) x-direction and the (ii) y-direction. The electromagnetic field pattern demonstrates the propagating mode in the holes between the metal, which leads to high transmission. The diameter of the holes $d = 1200$ nm is much larger than the wavelength $\lambda = 550$ nm such that the transmission is close to 100%. The transmission $T_{xx} = 84.8\%$ and $T_{yy} = 84.9\%$, while the sheet resistance $R_{s,xx} = R_{s,yy} = 7.0\ \Omega$/sq. The transmission of the NM is higher than the geometric aperture, which is $\frac{2\pi(d/2)^2}{\sqrt{3}a^2} = 77.3\%$. The loss at this wavelength is primarily due to absorption of the metal.

To demonstrate the potential of Cu NMs as a transparent electrode, we developed a large-area, low-cost method to fabricate Cu NMs directly on both rigid quartz and flexible PET substrates. Figure 21(a) shows a schematic of the microsphere lithography approach for fabricating Cu NMs. The microsphere lithography approach was adapted from nanosphere lithography methods that combine an air/water interface self-assembly technique with a solvent-vapor-annealing method.[120–122] Close-packed hexagonal polystyrene (PS) microspheres were obtained at the air/water interface in a 4" Petri dish using a self-assembly technique. The area of well-patterned PS microspheres can be scaled up by increasing the size of the container for industrial scale manufacturing. Wire-wound rod coating methods may also be adaptable for this purpose.[123] The patterned microspheres were then transferred to solid substrates dried in air at room temperature. Reactive ion etching (RIE) with oxygen was used to reduce the diameter of the PS microspheres. Cu was then deposited directly onto the PS microsphere patterned substrate with an evaporator at pressures of about 10^{-8} Torr. Finally, the PS microspheres were lifted off by ultrasonication to form Cu

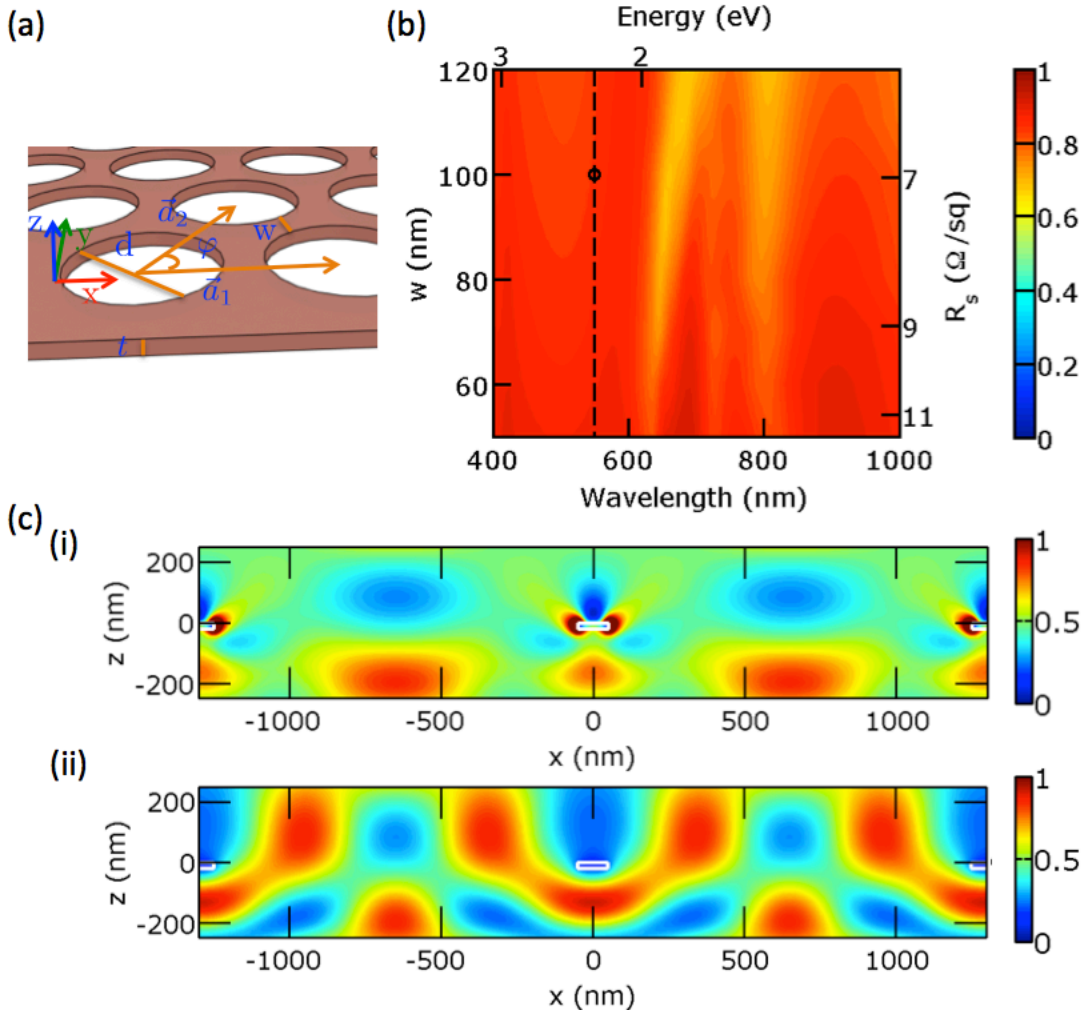

Figure 20: Simulation results. (a) Schematic of Cu NMs simulated, where the morphology consists of a hexagonal array of holes in a metal thin film, where a is the pitch, t is the thickness, and w is the metal width. (b) Contour plot of angle averaged transmission for various w with $a = 1300$ nm and $t = 20$ nm as a function of wavelength. The calculated sheet resistance, which depends on w, is shown on the right axis of the plot. The dashed black line indicates $\lambda = 550$ nm, which was used in Figure 19.

(c) Electric field intensity $|E|^2$ at $\lambda = 550$ mn for incident light polarized in the (i) x- and (ii) y-direction for $w = 100$ nm, which is indicated by the black circle in (b). The edges of the NM cross section are indicated with white lines.

NMs. No chemical process was involved in the metal-coating step, thus reducing the cost of reactant. Please refer to Supporting Information for details. This fabrication process may be easily modified for other evaporated metals depending on the particular application. Specific control over metal pitch a, thickness t, and width w may be accomplished through the self assembly of different diameter microspheres or nanospheres,[122] different etching times, and different evaporation times. Figure 21(b) shows representative scanning electron microscope (SEM) images of a Cu NM with $a = 1300$ nm, $w = 150$ nm, and $t = 40$ nm fabricated on a rigid quartz substrate. The high uniformity and long-range order of the NM is apparent in the images, where these qualities address the percolation and contact resistance issues of random NW networks or disordered structures. Figure 21(c) shows an optical image of a Cu NM on a flexible PET substrate about 40 cm^2. The figure also shows SEM images of the Cu NM at four different locations, where the NM exhibits more nonuniformities and defects in the lattice on the PET substrate compared to quartz. This is because the assembled microsphere monolayer has more lattice dislocations and defects due to deformation of the PET substrate during self-assembly from its low elasticity. The transparent conductor looks uniform and clear, without the appearance of Moiré fringes.

The optical transmittance of the Cu NMs was measured using an integrating sphere. Samples with various morphologies involving different w and t were fabricated and the diffuse transmission at $\lambda = 550$ nm was plotted as a function of sheet resistance in Figure 30. The NMs on rigid quartz exhibit higher transmission at a particular sheet resistance than the NMs on the PET substrates due to the better uniformity and ordering of the microspheres during self-assembly. The NMs on quartz achieve 80% transmission with a sheet resistance of 17 Ω/sq, which is comparable to ITO thin films. On PET, the NMs achieve 80% transmission with a sheet resistance of 60.5 Ω/sq and their performance is generally worse than that on quartz.

Figure 22(a) plots both the simulated and experimentally measured (on quartz) diffuse transmission spectrum for a Cu NM with $a = 1300$ nm, $w = 70$ nm, and $t = 15$ nm. The simulation results represent an averaged result for x- and y-polarized incident light as discussed before. The simulated and experimentally transmission spectra are fairly close to each other, where the slight differences can be accounted for by statistical variations and

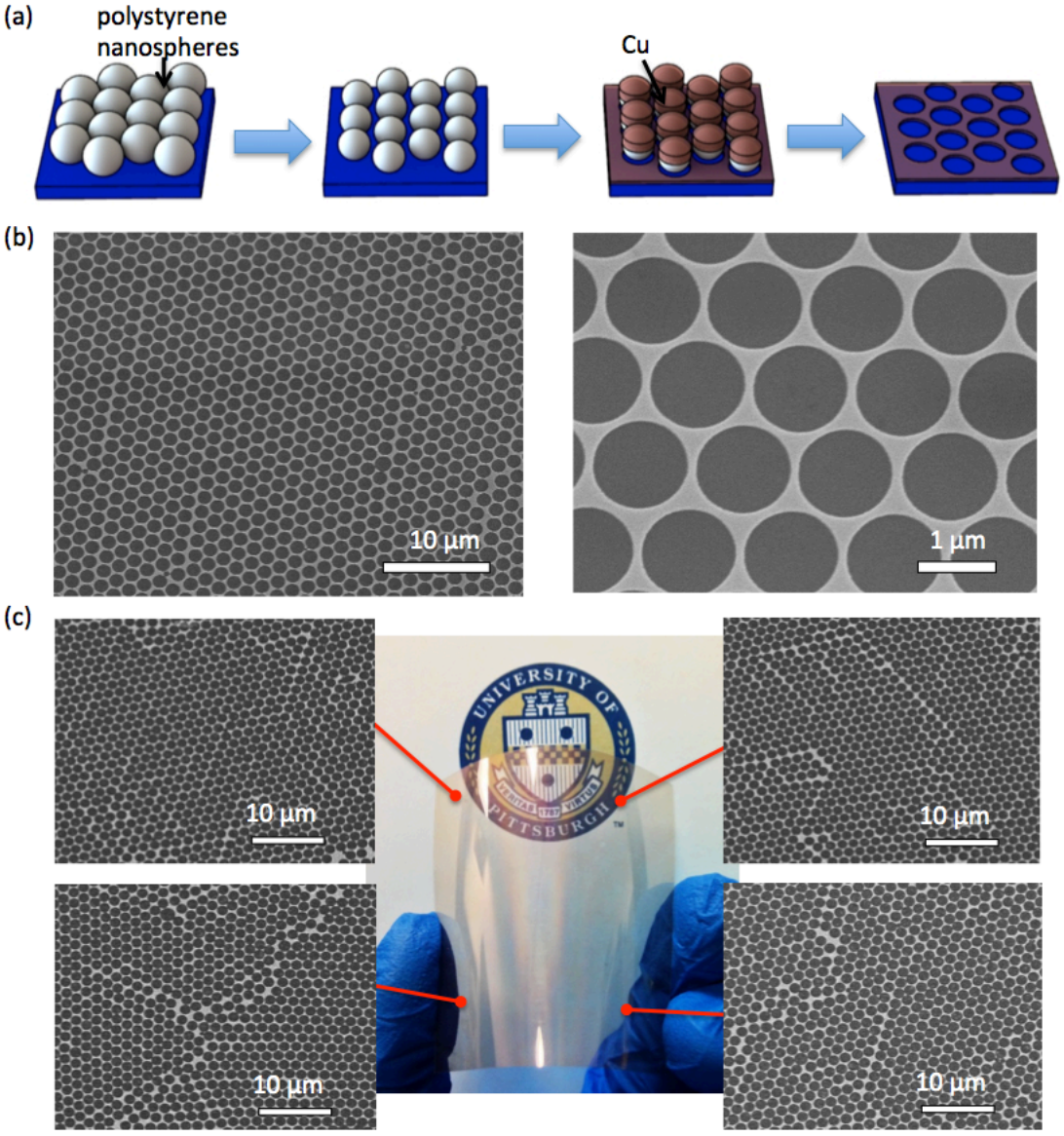

Figure 21: (a) Schematic of the Cu NM fabrication process. (b) SEM images of fabricated Cu NM with $a = 1300$ nm, $w = 150$ nm, and $t = 40$ nm on a rigid substrate. (c) Optical image of a Cu NM fabricated directly on a flexible polyethylene terephthalate (PET) substrate. SEM images show the Cu NM at four various locations.

imperfections in the fabricated structure. The averaged simulated sheet resistance for this NM is 12.1 Ω/sq, with $R_{s,xx} = R_{s,yy} = 12.1$ Ω/sq, while the measured sheet resistance was 20.6 Ω/sq. The NM simulations do not consider surface or grain boundary scattering, and thus predict lower sheet resistances than those measured.

Figure 22(b) shows the simulated diffuse transmission, specular transmission, and absorption versus sheet resistance for Cu NMs with different sheet resistance. The specular transmission was determined from the fraction of power transmitted into the $(0, 0)$ diffraction mode and the diffuse transmission was determined from the total transmitted power. See the Supporting Information for details. The average difference between the simulated diffuse and specular transmission is about 2% and the difference increases for samples with larger sheet resistance.

Figure 22(c) shows the experimentally measured diffuse transmission, specular transmission, and absorption versus sheet resistance for various Cu NMs on PET. For Cu NMs on quartz substrates, the average difference between diffuse and specular transmission is about 4%, which is lower than random Ag NW films which have a difference of about 10%.[14] Less scattering makes the electrode appear less hazy and should be advantageous for applications such as displays. By comparing Fig. 22(b) and (c), we notice that simulations overestimate the transmission since the fabricated samples are not perfectly ideal, and the simulated sheet resistance are also lower than the experimental values because bulk resistivity was assumed, which does not consider electron scattering from the grain boundaries and surfaces.

Figure 23 shows the results of various durability tests to evaluate the robustness of the Cu NMs. Fig. 23(a) shows the variation in the sheet resistance of two Cu NMs on PET substrates after both bending in compression and tension. The Cu NM for both bending tests has a geometry of $t = 20$ nm, $a = 1300$ nm, and $w = 100$ nm. The original sheet resistance of the samples prepared for the tension and compression tests are 22.5 Ω/sq and 21.4 Ω/sq respectively. After 150 cycles of bending, the sheet resistance for the samples are 27.2 Ω/sq and 22.6 Ω/sq, demonstrating good durability under bending. Fig. 23(b) shows the change in sheet resistance of a Cu NM on quartz substrates after the heating test. The geometry of the Cu NM is $t = 15$ nm, $a = 1300$ nm, and $w = 120$ nm. The sheet resistance of the sample changed from 16.6 to 20.0 Ω/sq after six days of continuous heating on a

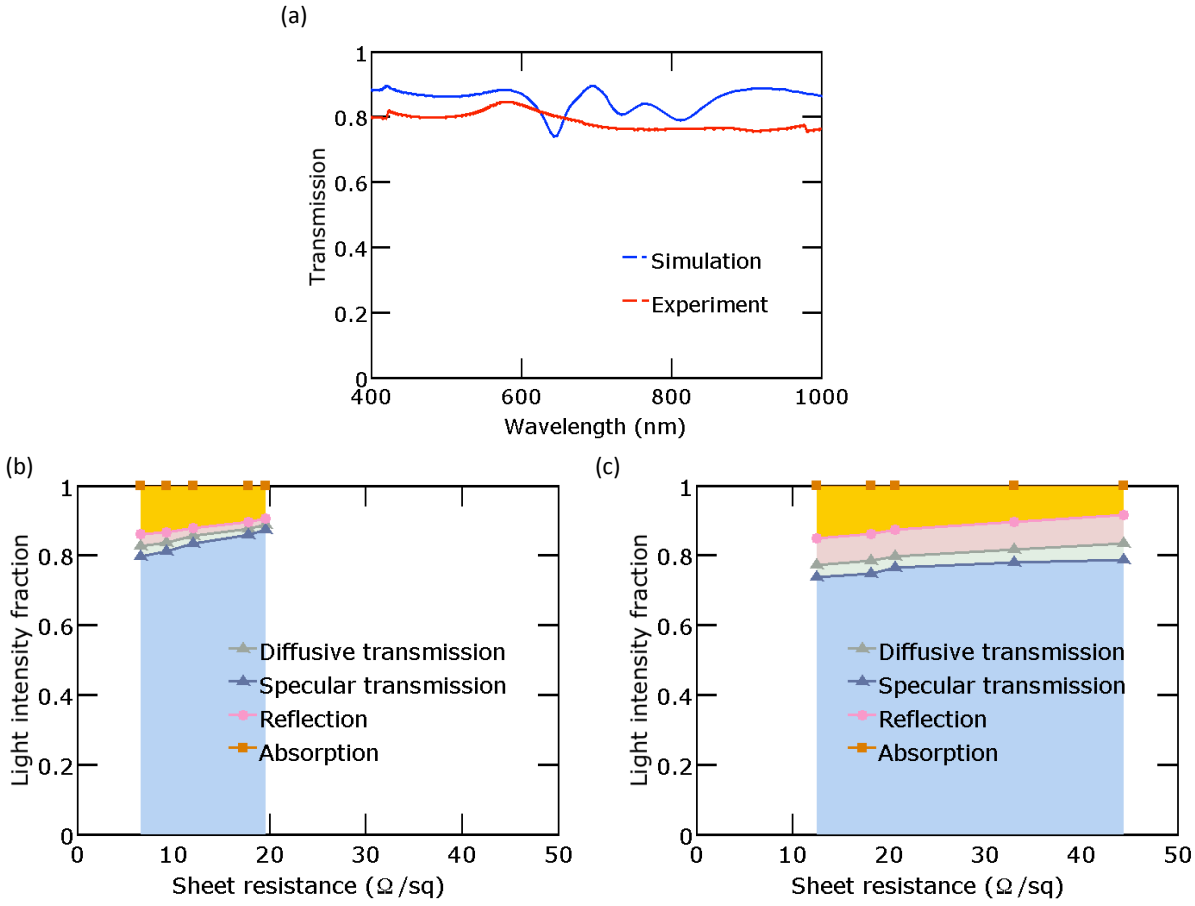

Figure 22: (a) Transmission spectrum for Cu NM with $a = 1300$ nm, $w = 70$ nm, and $t = 15$ nm obtained by simulation and experiment. (b) Plot of simulated diffuse transmission, specular transmission, reflection, and absorption versus sheet resistance for Cu NMs with various geometry at $\lambda = 550$ nm. (c) Plot of experimental diffuse transmission, specular transmission, reflection, and absorption versus sheet resistance for a variety of Cu NMs on quartz at $\lambda = 550$ nm.

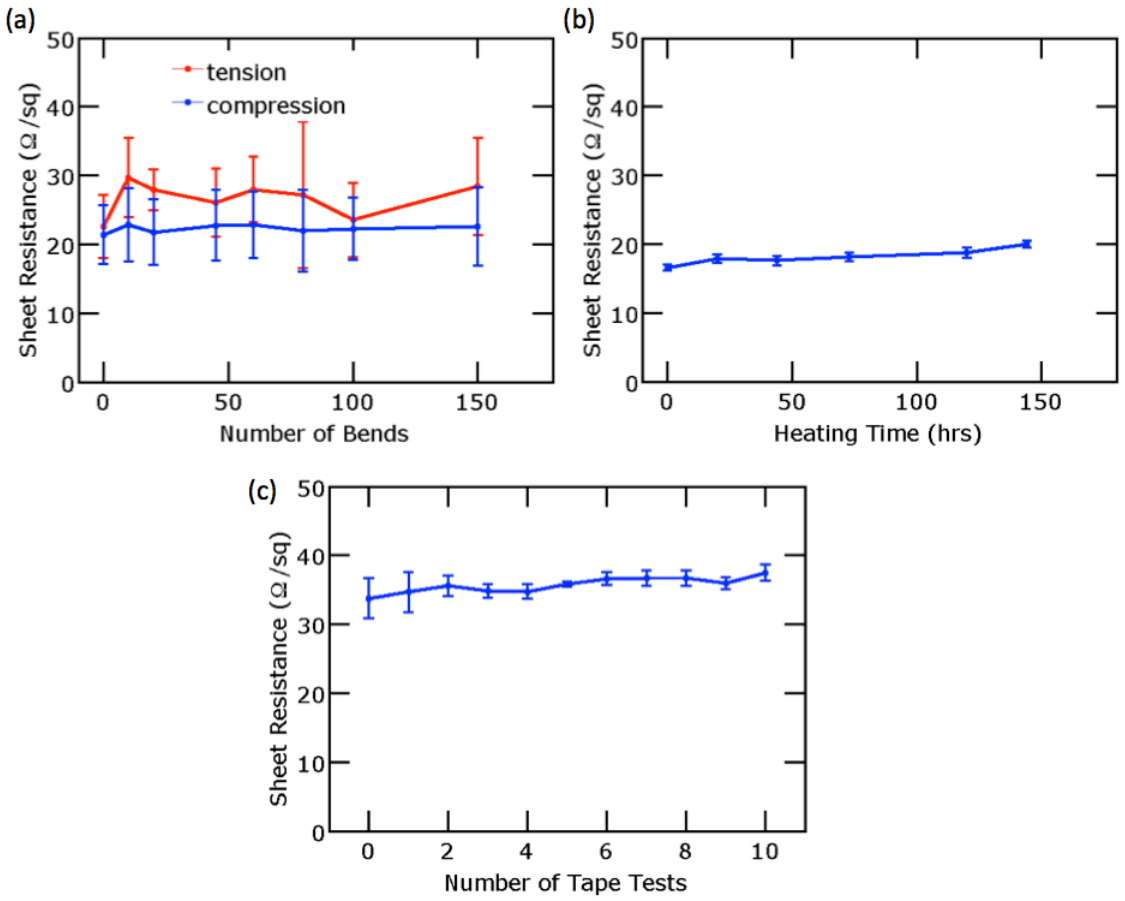

Figure 23: Durability tests for Cu NM on PET substrate. (a) Sheet resistance versus number of bends for Cu NM on PET. The bending curvature is 0.5 inch. (b) Sheet resistance versus heating time for Cu NM heated at 65°C in air. (c) Sheet resistance versus number of tape tests for Cu NM on PET substrate. Error bars correspond to the standard deviation of four measurements.

hot plate at 65°C. Cu in particular is prone to oxidation and alloying or passivation of the sample may help reduce sheet resistance degradation, especially at higher temperatures.[124] Fig. 23(c) shows the results of tape tests where Scotch® tape was pressed onto the NMs with finger pressure and then pulled off to assess the attachment of the Cu NM to the PET substrate. The geometry of the Cu NM is $t = 15$ nm, $a = 1300$ nm, and $w = 120$ nm. The sheet resistance of the sample only rose from 34.4 Ω/sq to 34.8 Ω/sq after ten cycles of tape tests.

4.2 CONCLUSIONS

In conclusion, we reported both simulations and experiments of Cu NMs. We investigated their transparency and sheet resistance and evaluated the potential of these structures as transparent conductors. Simulated Cu NMs demonstrate the role of propagating modes in transmission and thickness-dependent resistivity transport simulations compare reasonably to experimental results. We demonstrate a scalable method to fabricate Cu NMs on both rigid quartz substrates and flexible PET substrates. The samples on quartz substrates demonstrate good uniformity and order, with performance comparable to ITO, while the PET substrates have slightly poorer performance due to disorder and defects in the NM lattice. Durability tests demonstrate that the NMs are not affected significantly to bending, heating, and abrasion. Future studies may focus on larger pitches, which should offer better transparencies at a given sheet resistance.[80, 81] The morphology of these NMs may also be varied for narrowband transmission or filtering for other optoelectronic applications.

5.0 HIERARCHICAL TRANSPARENT CONDUCTOR MATERIALS

The idea of developing a variety of nanoscale materials for TCs, such as metal NW networks and metal NMs, can be considered as using highly transparent material, i.e. air, to modulate the transparency of inherently conductive materials. Nevertheless, tuning the transparency of a conductive material using air is a relatively passive strategy. In this section, we study the design principles and the fabrication methods of hierarchical materials, which are a combination of microscale and nanoscale materials, for improved TC transparency, electrical conductivity, and better carrier delivery or collecting ability. We propose to investigate the performance of hierarchical graphene/metal grid structure and hierarchical metal NM/microgrid (MG) structures in this chapter.

5.1 HIERARCHICAL GRAPHENE/METAL GRID STRUCTURES

There has been much interest in carbon nanostructured materials, such as random carbon nanotube networks[125–128] and graphene,[13, 129] as a potential substitute for ITO. We have reviewed carbon-based materials for TCs in the Introduction chapter. However, carbon nanotubes are very expensive and they suffer from high tube-tube resistance such that their performance has yet to exceed ITO. Graphene films (ranging from monolayer graphene to ultrathin graphite) have recently emerged as a promising transparent electrode material due to its high carrier mobility and high transparency when thin.[66, 67] However, theoretical estimates of single crystalline graphene films suggest that the highest achievable figure of merit is $\sigma_{DC}/\sigma_{op} = 11$ or $R_s = 317\ \Omega$/sq at $T = 90\%$.[130] This performance is worse than even the minimum performance needs of transparent conductors in industry, which are $\sigma_{DC}/\sigma_{op} = 35$

or $R_s = 100$ Ω/sq at $T = 90\%$.[130] Experimentally fabricated graphene typically suffers from much higher sheet resistance than the theoretical limit due to imperfections in the 2D structure, such as grain boundaries, lattice defects, and oxidative traps. Graphene produced by scalable production methods, such as chemical vapor deposition (CVD) and epitaxial growth, usually has a sheet resistance of hundreds of Ω/sq at around 80% transmission for the wavelength 550 nm.[131] Graphene has high sheet resistance because its intrinsic carrier concentration is low. The intrinsic carrier concentration is only about 9×10^{10} cm^{-2} at room temperature (or 300 K)[132] or about 10^{11} to 10^{12} cm^{-2} with unintentional or surface adsorbate doping.[133] Theoretical calculations have suggested that higher values of $\sigma_{DC}/\sigma_{op} = 330$ or $R_s = 11$ Ω/sq at $T = 90\%$ may be achievable by doping.[130] However, highly doped graphene still falls short of typical industry needs of $\sigma_{DC}/\sigma_{op} = 350$ or $R_s = 10$ Ω/sq at $T = 90\%$.[130]

In this section, we propose to demonstrate that single-layered graphene may be integrated with microscale metal grids to form hierarchical graphene/metal grid structures that have significantly improved performance over graphene thin films or metal grid structures by themselves. The hierarchical structure exhibits σ_{DC}/σ_{Op} as high as 8900 and 94% diffusive transmission at 0.6 Ω/sq. In contrast, the single layer of graphene has $\sigma_{DC}/\sigma_{Op} = 12$ and 97% diffusive transmission at 1000 Ω/sq. The sheet resistance may be decreased by over 3 orders of magnitude with only a slight decrease in transmission. The hierarchical structures demonstrate uniform conductivity over large areas and local current conductivity due to the graphene. The fabrication process, consisting of graphene deposition and transfer and metal photolithography patterning, has the potential for continuous and scalable manufacturing. Thermal and bending tests also demonstrate the improved durability of the hierarchical structures compared to microscale metal grids as the graphene limits oxidation and enhances the adhesion of the metal to the substrate.

5.1.1 Results and Discussion

Figure 24(a) shows a schematic of the hierarchical graphene/metal grid structure. The graphene is produced on copper foils by CVD[134] and transferred onto a hexagonal mi-

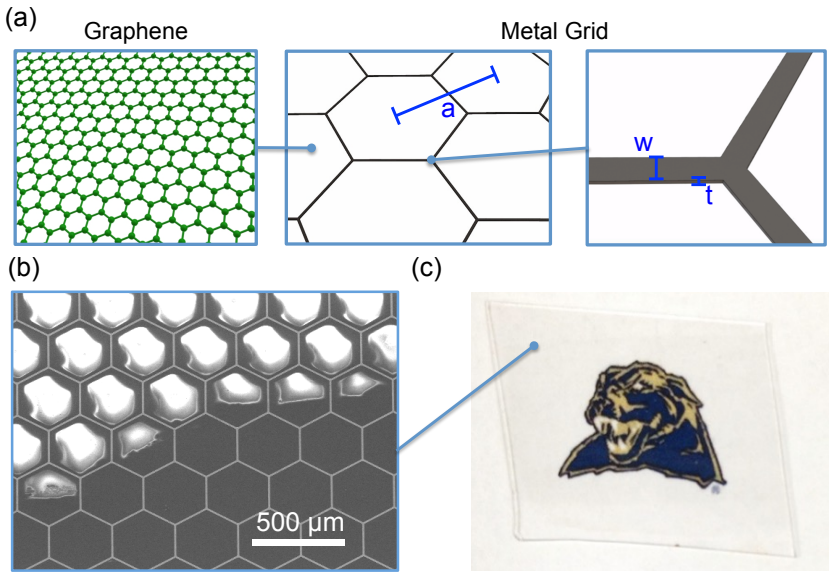

Figure 24: (a) Schematic of the hierarchical graphene/metal grid transparent conductor, where the structure consists of a single-layer graphene sheet fabricated by CVD and transferred on a hexagonal metal grid with pitch a, grid width w, and thickness t. (b) SEM image for the edge of a graphene sheet on microscale silver (Ag) grid with $a = 300$ μm, $w = 10$ μm, and $t = 1$ μm on a rigid quartz substrate. The dark part on the bottom is where there is a graphene sheet. (c) Optical image of graphene/microscale Ag grid on quartz substrate.

croscale silver (Ag) grid using poly(methyl methacrylate) (PMMA). The microscale Ag grids are fabricated using photolithography and e-beam evaporation. The morphology of the microscale grid is defined by the pitch of the hexagonal array a and the width w and thickness t of the metal. The microscale metal grids by themselves may exhibit over 90% transmission at less than 0.5 Ω/sq sheet resistance.[80, 81] However, they are not a good transparent conductor material *per se*, because the distance between the metal is hundreds of microns and this results in the poor local collection or delivery of carriers. Figure 24(b) shows a representative scanning electron microscope (SEM) image of the hierarchical structure fabricated on a quartz substrate. For this particular sample, $a = 300$ µm, $w = 10$ µm, and $t = 1$ µm. The SEM image is taken at the edge of the deposited graphene sheet. There is no graphene in the upper left of the SEM image; the bright contrast in this area is a result of surface charging due to poor conductivity in the empty areas between the microscale Ag grids. The lower right of the SEM image is covered by graphene and therefore shows a much darker contrast. The graphene sheet can cover the microscale Ag grids conformally without significant cracks and wrinkles. The hierarchical graphene/Ag grid samples exhibit a uniformly transparent appearance over an area of about 2 cm × 2 cm as shown in Fig. 24(c). Conductive atomic force microscopy measurements demonstrate that the hierarchical structures exhibit uniform localized current conductivity at the microscale. This is in contrast to random networks of carbon nanotubes or NWs. The high uniformity of localized current conductivity for the hierarchical structures is desirable for a more uniform appearance in flat panel displays and better carrier collecting ability in solar cells.

Figure 25(a) plots the relationship between the diffusive transmission and sheet resistance for a variety of graphene thin films. Our experimental data for the hierarchical graphene/Ag grid structures is plotted with blue stars. The diffusive and specular transmission of the samples were measured using a spectrophotometer with and without an integrating sphere respectively. The diffusive transmission accounts for transmission from all angles, while the specular transmission only accounts for normal transmission. Our diffusive transmission data is plotted at the wavelength $\lambda = 550$ nm, which is near the middle of the visible spectrum. The effect of the substrate has been excluded by renormalization. The performance of the graphene without the Ag grids is shown with green stars. The sheet resistance of the

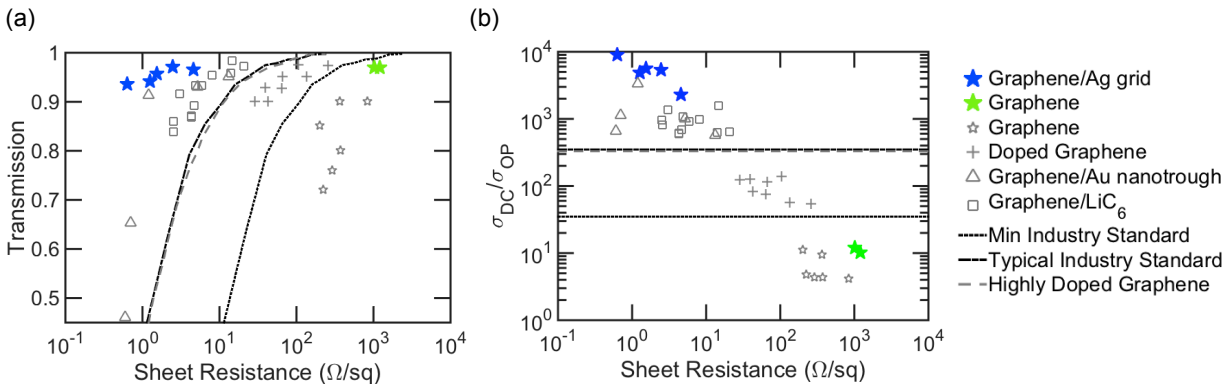

Figure 25: (a) Transmission versus sheet resistance for graphene in the literature. The minimum industry standard, typical industry standard, and theoretical calculation of highly doped graphene are plotted with lines.[135] Experimental data for chemical vapor deposited (CVD) graphene,[60, 72, 131, 136–138] roll-to-roll synthesized and transferred doped graphene (R2R),[13] graphene with gold (Au) nanotroughs citeAn:14 and lithiated graphene[139] are also shown. (b) Figure of merit of the various graphene compared with the minimum industry standard and theoretical estimates of doped graphene limit.

hierarchical structures slightly increased from that of the metal grid due to some oxidation or corrosion of the metal during the graphene transfer. For example, our Ag grid with a = 200 µm, w = 5 µm, and t = 1 µm exhibited R_s = 0.5 Ω/sq and diffusive transmission of 98%. After graphene transfer, the sheet resistance increased to R_s = 1.2 Ω/sq and diffusive transmission dropped to 94%.

The minimum and typical transparent conductor requirements are shown with the black dotted and dash dotted lines, and the theoretical limit for highly doped graphene is shown with the gray dashed line. For comparison purposes, we plot the best graphene data that we are aware of in the literature for CVD intrinsic graphene[60, 72, 131, 136–138] and roll-to-roll synthesized and transferred doped graphene[13] using grey markers. Other graphene films have also been reported, such as exfoliated graphene,[140] reduced graphene oxide (rGO),[68, 141] and chemically modified graphene (CMG),[142] though these tend to have much worse performance with sheet resistances over 1000 Ω/sq. Two structures, graphene with Au nanotroughs[143] and lithiated graphene,[139] have recently demonstrated performances above theoretical limit estimates for doped graphene and are also plotted. Our CVD single layer of graphene exhibits very high transmission of 97%, but the sheet resistance is also very high and over 1000 Ω/sq. By integrating the graphene with the Ag microscale grids, the sheet resistance may be decreased substantially to between 0.6 and 5 Ω/sq. The transmission decreases only slightly to between 94 to 97%.

Figure 25(b) plots the figure of merit σ_{DC}/σ_{op} of these transparent conductors versus sheet resistance. σ_{DC}/σ_{op} is a commonly used figure of merit (FoM) for transparent conductors[90], where σ_{DC} is the DC conductivity of the material and σ_{op} is the optical conductivity. This FoM can be represented in terms of T and R_s by $T = \left(1 + \frac{\mathrm{Z}_0}{2R_\mathrm{s}} \frac{\sigma_{op}}{\sigma_{DC}}\right)^{-2}$, where Z_0 = 377 Ω is the free space impedance. The FoM for the single-layer graphene is just slightly above 10. The hierarchical structures have significantly performance with FoMs from 2300 to 8900. These FoMs are above theoretical doped graphene limits and the highest values in the literature we are aware of for graphene-based structures.

The diffusive transmission spectra for the graphene/Ag grid structures and graphene films on quartz are plotted in Fig. 26(a). The geometry for the Ag grid in the hierarchical structures is a = 200 µm, w = 5 µm, and t = 1 µm. The average diffusive transmission across

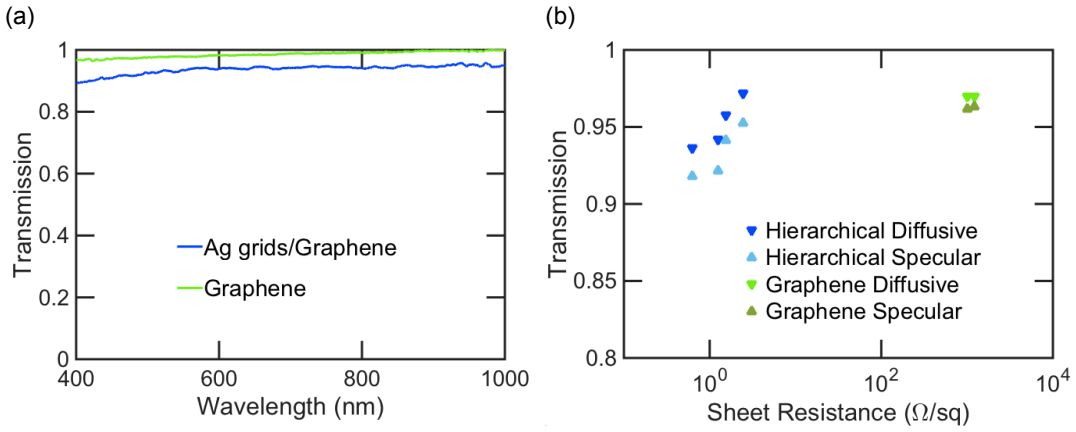

Figure 26: (a) Diffusive transmission spectrum for hierarchical graphene/Ag grid and single-layer graphene on quartz. The sheet resistance is 0.63 Ω/sq for the graphene/Ag grids sample and 1.0 kΩ/sq for the graphene sample. (b) The diffusive and specular transmission (at $\lambda = 550$ nm) for the graphene/Ag grid and graphene samples as a function of sheet resistance. The effect of substrate has been excluded.

the visible spectrum for the graphene sample is 96.8% and is 92.5% for the graphene/Ag grids sample. The incorporation of microscale Ag grids results in about a 4% drop in the average diffusive transmission of graphene in the range of 400 nm to 700 nm.

Unlike sputtered ITO thin films, which have lower transmission in the long wavelength range,[144] the transmission spectrum for our hierarchical graphene/Ag grid is almost flat, which is important for applications such as thin film or organic solar cells. No significant plasmonic effect is observed in the transmission spectrum because the dimensions of the Ag features exceed the wavelength interested. The samples have a uniform, transparent appearance without Moire fringes. Fig. 26(b) demonstrates the diffusive transmission and specular transmission spectra for the hierarchical samples and graphene control sample at $\lambda = 550$ nm. The hierarchical structures exhibit little scattering of light and very low haziness. The difference between the diffusive and specular transmission is 1.5% on average. In contrast, random Ag NW films have demonstrated a difference of about 10%.[14] The low

scattering and low haziness of the graphene/Ag grid structrues is beneficial for showing clear images and text in displays.

To evaluate the thermal stability of the hierarchical structures, samples were heated at 300 °C on a hot plate and compared to control samples, which only have the microscale Ag grids on quartz. Two contacts were deposited onto the samples and the resistances of both sample were monitored.

The geometry of the Ag grids in both samples is $t = 0.6$ µm, $a = 200$ µm, and $w = 10$ µm. Figure 27 shows the change in resistance of the hierarchical structure and control sample on quartz substrate with the heating test. After 65 hours of heating, the resistance for the sample with only microscale Ag grids increased by 83%. Oxidation incurred conductivity degradation has been previously reported in Ag NW thin films after one hour of heating in the ambient at 200 °C.[63] However, the resistance of the graphene/Ag grid structures only increased by 11%. Graphene is known for its ability to block gas molecules,[61] and thus, may limit the Ag oxidation and maintain a more stable performance at elevated temperature. The resistance for both samples became constant after additional heating past 42 hours. The graphene should offer additional benefits for copper nanostructures, which are more prone to oxidation than silver.[7, 145]

To evaluate the durability of the graphene/Ag structures for flexible optoelectronics, bending tests were performed. Graphene/Ag grid and Ag grid only samples with 100 nm, 500 nm, and 1 µm Ag thicknesses were fabricated on flexible PET substrates. The Ag grids in the tests have pitch $a = 500$ µm and width $w = 10$ µm.

The resistance between two deposited contacts was monitored in the bending test. The samples were bent around a steel rod with 1 cm diameter. Both compression and tension were applied by bending by placing the Ag grid side towards the steel rod and away from the steel rod respectively. Figure 28(a) and (c) show the variation in the resistance of graphene/Ag grid and Ag grid on PET substrates respectively after both bending in compression and tension for various metal thicknesses. The 1 µm thick Ag grid (without graphene) data is not shown in Fig. 28(c), because the Ag grid detached from the substrate after less than 10 bending cycles. The resistance for both graphene/Ag grid and Ag grid increase after bending and the resistance increases faster for thicker Ag grid due to greater strain on the surface of

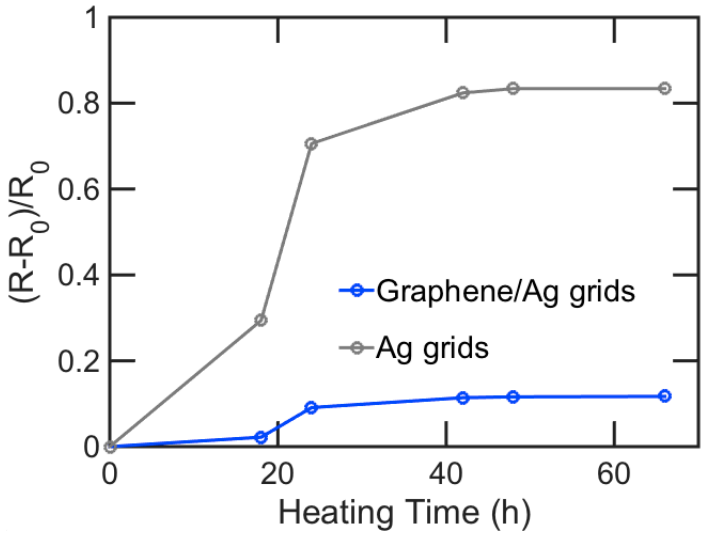

Figure 27: Heating test results for microscale Ag grids and microscale Ag grids/graphene samples at 300 °C.

the Ag grid. A single-layer graphene sheet will protect the Ag grid from bending, especially for thick Ag grids. For 100 nm thick Ag grids, the resistance increased by 15.1% without graphene and by 9.5% with graphene after 200 tension bending cycles. For 500 nm thick Ag grids, the resistance increased by 41.8% without graphene and by 18.2% with graphene after 200 tension bending cycles. Fig. 28(b) and (d) show structures with metal thickness $t = 500$ nm after 200 tension bending cycles. As can be seen in Fig. 28(b), the hierarchical structures exhibit increased resistance to cracking and delamination of the metal grids. There is some metal cracking near the vertices of the hexagons. The structures are mostly intact as the the graphene strengthens the attachment between the Ag grid and PET substrate. In contrast, as shown in Fig. 28(d), the Ag grids without graphene, exhibit large-scale cracking and delamination.

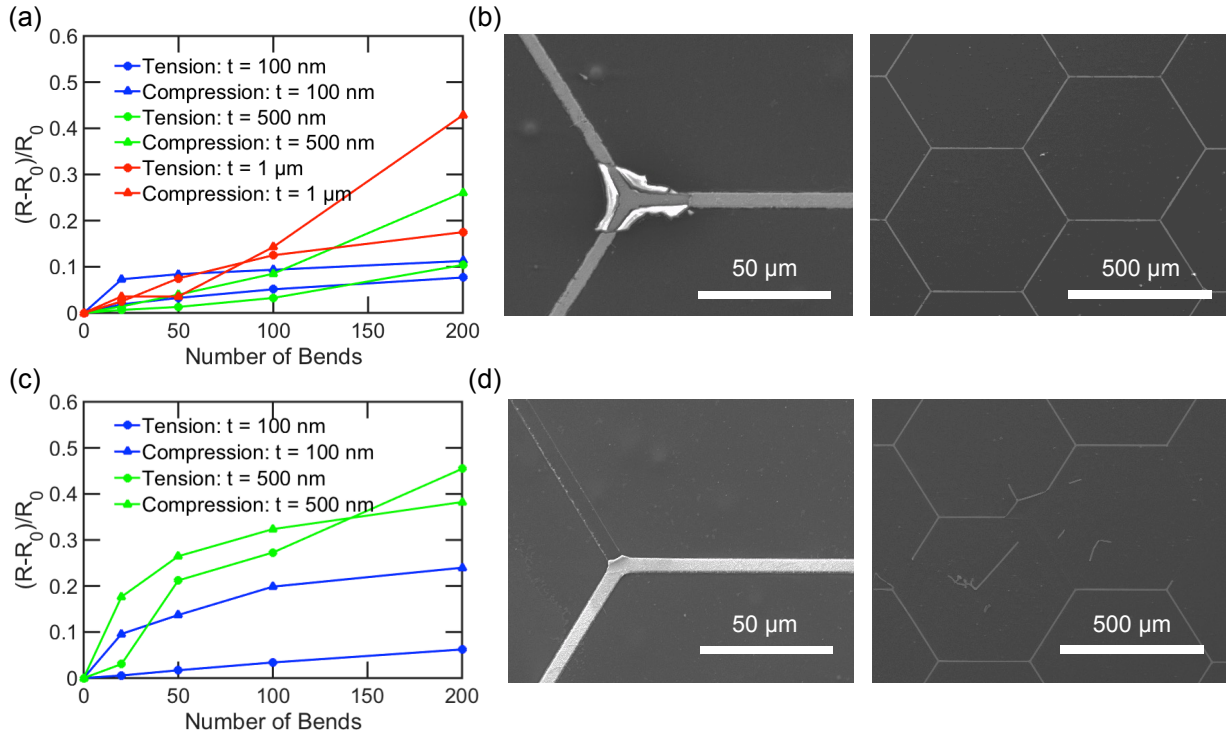

Figure 28: (a) Change in resistance versus number of bends for graphene/Ag grid. (b) SEM images after 200 tension bending cycles for graphene/Ag grid. (c) Change in resistance versus number of bends for Ag grid. (d) SEM images after 200 tension bending cycles for Ag grid. The structures were fabricated on PET film. The bending curvature is 0.5 cm. The Ag grid is defined by $a = 500$ μm and width $w = 10$ μm. $t = 500$ nm for the grids shown in (b) and (d).

5.1.2 Conclusions

In summary, a proof-of-concept graphene/microscale Ag grid transparent conductor was designed to break the limitation on transmission and resistance of graphene. The transparent conductor was fabricated on quartz and characterized. Our structures exhibit up to 94% diffusive transmission at 0.6 Ω/sq, which surpasses the theoretical performance limit of highly doped graphene thin films. The transparent conductor is stable in ambient air for prolonged heating at 300 °C due to the oxygen blocking property of graphene. A single-layer graphene will also enhance the adhesion of the metal to the substrate for flexible optoelectronic applications, as demonstrated by bending tests. In the future, the work can be extended to the scalable manufacturing of these structures on plastic substrates for flexible optoelectronic devices.

5.2 HIERARCHICAL METAL NANOMESH/MICROGRID STRUCTURES

Random Ag NW films fabricated by solution-based methods have demonstrated superior optical transmission and sheet resistance compared to ITO films.[14, 16, 22, 63] However, the wire-wire junction resistance and percolation effects may be deleterious for random network TCs.[108] These films also tend to exhibit haze factors ranging from 13% to 33% due to Mie scattering.[14] Recently, we demonstrated Cu NMs that avoid these performance limitations because they are uniform, ordered, and junctionless.[7]

Metal NW films with larger NW diameters and pitches tend to have better transparent conductor performance.[80, 81] However, a large separation between NWs will result in poor localized conductivity and thus, poor uniform carrier collection or delivery. This is especially a problem for organic optoelectronic devices, which have short exciton diffusion lengths.[146] Hierarchical structures may combine the advantages of both localized conductivity in NWs or NMs and the better transparent conductor performance of larger structures such as a MG. For example, random Ag NW films have recently been combined with mesoscale wires (widths from 1 to 5 μm) to demonstrate $T = 92\%$ at $R_s = 0.36$ Ω/sq or σ_{DC}/σ_{op} over

12000.[147] However, these structures suffer from some of the same contact resistance issues of random NW films and for example, must be annealed at 200 °C for 40 minutes to fuse the different length scale wires. The randomness of the structure may also result in less uniform sheet resistance and optical properties over micron length scales. We have also recently demonstrated a hierarchical structure that integrates graphene with a metal grid to achieve $T = 94\%$ at $R_s = 0.6$ Ω/sq or σ_{DC}/σ_{op} of almost 9000.[8]

I conducted both simulations and experiments to investigate the performance of hierarchical Ag NM/Ag MG structures as transparent conducting electrodes. The hierarchical structure exhibits diffusive transmission $T = 83\%$ at $R_s = 0.7$ Ω/sq or $\sigma_{DC}/\sigma_{op} = 2900$ when fabricated on a quartz substrate and $T = 81\%$ at $R_s = 0.7$ Ω/sq or $\sigma_{DC}/\sigma_{op} = 2300$ when fabricated on a polyethylene terephthalate (PET) substrate. In contrast, Ag NMs fabricated on quartz exhibit $T = 83\%$ at $R_s = 13$ Ω/sq or $\sigma_{DC}/\sigma_{op} = 140$. The sheet resistance of the NM may be decreased by over an order of magnitude with only a slight decrease in transmission by integration with the MG.

The hierarchical structures also exhibit more uniform resistance and optical properties on the microscale compared with random networks of NWs. In addition, we performed durability experiments to assess the performance of the Ag NM/MG under various bending, heating, and abrasion conditions.

5.2.1 Results and Discussion

Figure 29(a), (b) show the schematic and representative scanning electron microscope (SEM) images of the hierarchical NM/MG structure. The Ag NM consists of a hexagonal array of holes in Ag thin film. The primitive lattice vectors are $\vec{a_1}$ and $\vec{a_2}$ with $|\vec{a_1}| = |\vec{a_2}| = a_{NM}$, as shown in Figure 29(a). The NM is fabricated using a microsphere lithography approach, which we have previously reported for Cu.[7]

Specific control over the various NM geometric parameters, pitch a_{NM}, thickness t_{NM}, and width w_{NM}, may be accomplished through the self assembly of different diameter microspheres or nanospheres,[148] different etching time, and different metal evaporation time. The geometric parameters for the MG include the pitch a_{MG}, width w_{MG}, and thickness

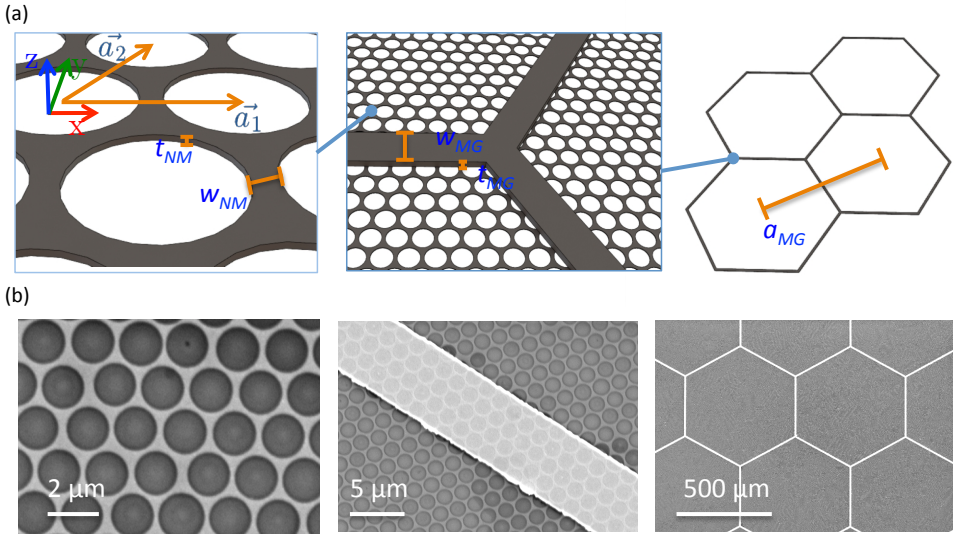

Figure 29: (a) Schematic of the hierarchical Ag NM/MG structure and various geometric parameters that define its morphology. (b) SEM images of AG NM/MG structure with a_{NM} = 2000 nm, w_{NM} = 100 nm, t_{NM} = 30 nm, and a_{MG} = 500 μm, w_{MG} = 10 μm, and t_{MG} = 1 μm

t_{MG}, as shown in Figure 29(a). The Ag MG is fabricated by photolithography with lift-off metal patterning. Figure 29(b) shows SEM images of the Ag NM/MG structure with a_{NM} = 2000 nm, w_{NM} = 1900 nm, and t_{NM} = 30 nm, and a_{MG} = 500 μm, w_{MG} = 10 μm, and t_{MG} = 1 μm. The high uniformity and long-range order of the structure is apparent in the images, where these qualities address the percolation and contact resistance issues of random NW networks or disordered structures.

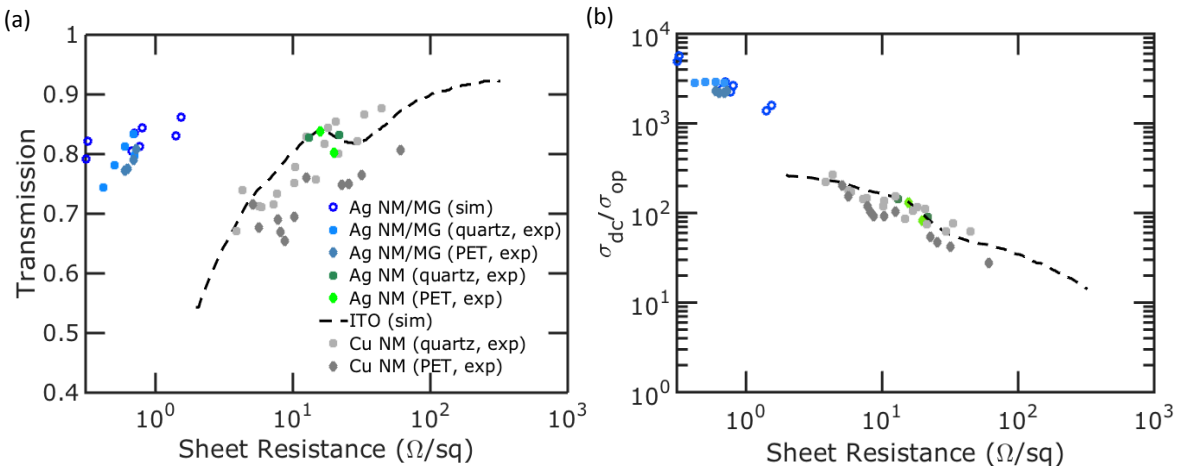

Figure 30: (a) Transmission versus sheet resistance for transparent conductors. Our Ag NM/MG data is shown in shades of blue and NM data is shown in shades of green at λ = 550 nm. Data for Cu NMs on quartz and PET substrates[7] and simulated ITO thin films[63] is also shown. (b) Figure of merit versus sheet resistance for the same data.

Figure 30(a) plots the relationship between diffusive transmission and sheet resistance for the hierarchical NM/MG structures along with various other transparent conductors in the literature. The data for Ag NM/MG structures is plotted with various shades of blue for simulations and experiments on quartz and PET substrates. Experimentally fabricated Ag NMs on quartz and PET substrates is plotted with different shades of green. Our transmission data is plotted at the wavelength λ = 550 nm, which is near the middle of the visible spectrum. The effect of the substrates has been excluded. For comparison purposes, we plot simulation data for ITO thin films[63] as well as our previously reported Cu NMs on quartz and PET substrates.[7] Ag NMs exhibit comparable performance to ITO thin films

and Cu NMs. The Ag NMs exhibit comparable performance to Cu NMs because the transmission properties at the length scales involved are primarily independent of material and the resistivity of Ag is only slightly lower than that of Cu.[80, 81] The Ag NMs fabricated on rigid quartz also performs slightly better than that fabricated on PET due to the better uniformity and ordering of the structure.[7] The sheet resistance of the Ag NM is between 13 and 21 Ω/sq with about 83% transmission on quartz, and on PET has a sheet resistance between 16 and 20 Ω/sq with a transmission between 81% and 83%. By integrating the Ag NM with the MG, the sheet resistance may be decreased substantially by over an order of magnitude without substantial decrease in transmission. The sheet resistance of the hierarchical Ag NM/MG on quartz is between 0.4 and 0.7 Ω/sq with a transmission between 74% and 83% and on PET is between 0.6 and 0.7 Ω/sq with a transmission between 77% and 81%. Our data demonstrates that Ag NM/MG samples fabricated on quartz substrates or PET substrates exhibit superior performance to ITO films. More details about the simulations and experiments and differences in the results between the two will be discussed later in the text.

Figure 30(b) plots the figure of merit σ_{DC}/σ_{op} of these transparent conductors versus sheet resistance. σ_{DC}/σ_{op} is a commonly used figure of merit (FoM) for transparent conductors,[90] where σ_{DC} is the dc conductivity of the material and σ_{op} is the optical conductivity. This figure of merit can be represented in terms of T and R_s by $T = \left(1 + \frac{\mathrm{Z}_0}{2R_\mathrm{s}} \frac{\sigma_{op}}{\sigma_{DC}}\right)^{-2}$, where $\mathrm{Z}_0 = 377\ \Omega$ is the free space impedance. The Ag NM has a σ_{DC}/σ_{op} of between 80 and 140. However, typical industry requirements are $\sigma_{DC}/\sigma_{op} = 350$.[130] By integrating the NM with the MG, we can improve σ_{DC}/σ_{op} drastically to over 2000.

Figure 31(a) plots both the simulated and experimentally measured (on quartz) diffusive transmission spectrum for the hierarchical structure with $a_{NM} = 2000$ nm, $w_{NM} = 100$ nm, $t_{NM} = 30$ nm, $a_{MG} = 200\ \mu$m, $w_{MG} = 5\ \mu$m, and $t_{MG} = 1\ \mu$m. The simulated and experimental transmission spectra are reasonably close to each other, where the minor differences can be accounted for by statistical variations and imperfections in the fabricated structure. The simulated sheet resistance for this geometry is 0.67 Ω/sq while the measured sheet resistance was 0.70 Ω/sq. The haze factor, defined as $\frac{T-T_{spec}}{T}$, is an important property for transparent conductors, where T is the diffusive transmission and T_{spec} is the specular

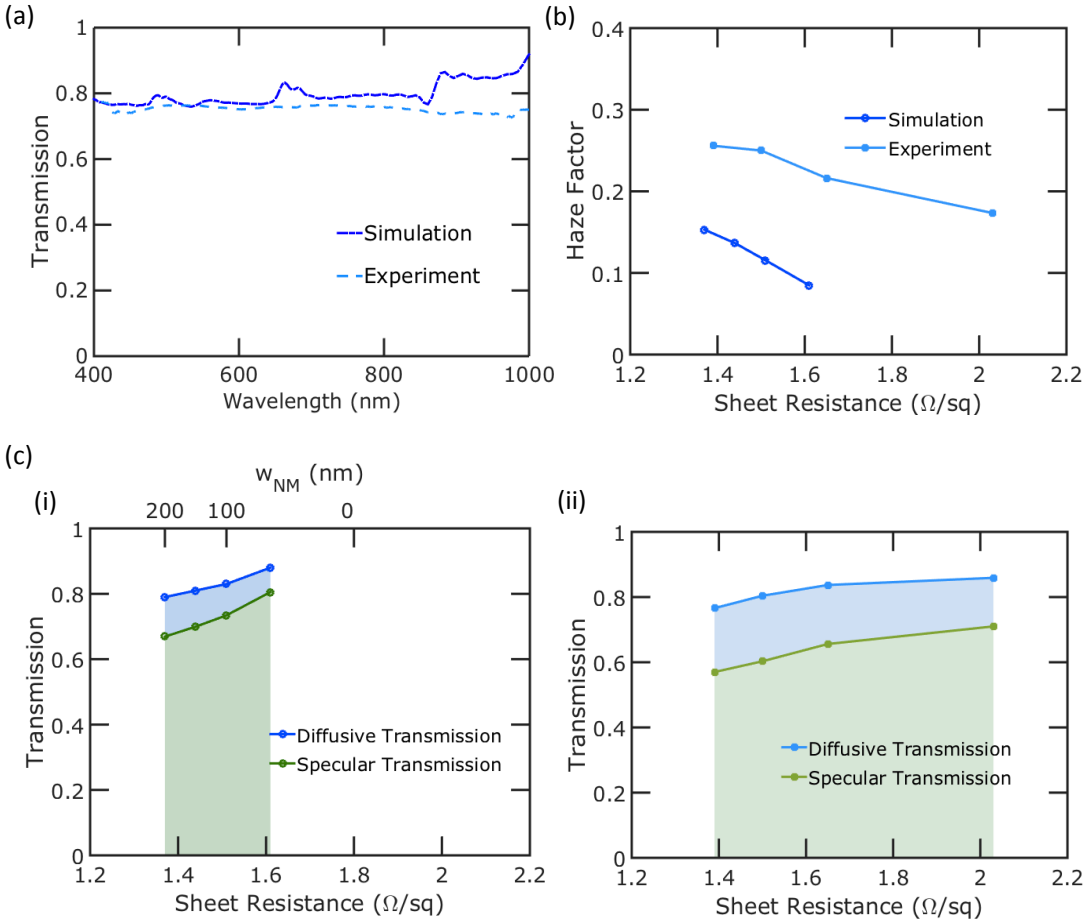

Figure 31: (a) Diffusive transmission spectrum for Ag NM/MG with $a_{NM} = 2000$ nm, $w_{NM} = 100$ nm, $t_{NM} = 30$ nm, $a_{MG} = 200$ μm, $w_{MG} = 5$ μm, and $t_{MG} = 1$ μm obtained by simulation and experiment. (b) Haze factor as a function of sheet resistance for experimental and simulated samples with $a_{MG} = 500$ μm, $w_{MG} = 5$ μm, $t_{MG} = 1$ μm, $a_{NM} = 2000$ nm, $t_{NM} = 20$ nm, and various w_{NM}. (c) Diffusive transmission and specular transmission as a function of sheet resistance at $\lambda = 550$ nm for Ag NM/MG with different extends of haziness using (i) simulation and (ii) experiment.w_{NM} is varied from 200 to 50 nm in simulation to match the experimental geometry and is labelled accordingly. $w_{NM} = 0$ corresponds to that the sheet resistance is only contributed by Ag MG.

transmission.[149] The haze factor of the hierarchical metal NM/MG transparent conductors is tunable by changing the geometric parameters and materials. The haze factor is mostly determined by diffraction and scattering from the NM, because its dimensions are of the same magnitude as the wavelength of incident light. The MG should have a geometric shadow because its features are larger than the wavelengths involved. We investigated the haze factor for Ag NM/MGs with geometric parameters a_{MG} = 500 μm, w_{MG} = 5 μm, t_{MG} = 1 μm, a_{NM} = 2000 nm, t_{NM} = 20 nm, and various w_{NM} using both simulation and experiments. Figure 31(c) shows (i) the simulated and (ii) the experimentally measured diffusive and specular transmission versus sheet resistance for Ag NM/MGs on quartz. In the simulation, w_{NM} ranges from 50 nm to 200 nm to match the experimental geometry. The haze factor of experimentally fabricated Ag NM/MGs demonstrate the same overall trends as the simulated data, but the haze factor is higher than the simulation results, due to imperfections in the surfaces and crystallinity. The simulated haze factor increases from 8% to 15% as w_{NM} increases from 50 nm to 200 nm, with R_s decreases from 1.6 to 1.4 Ω/sq. The haze factor in the fabricated samples increases from 17% to 26%, while R_s decreases from 2.0 to 1.4 Ω/sq correspondingly. The haze factor of the NM/MG can be tuned while maintaining a low sheet resistance because the overall conductance of the NM/MG is primarily due to the MG. As the NM width increases, the hole diameter decreases and the Airy pattern from Fraunhofer diffraction broadens. This results in a higher fraction of photons transmitted at non-normal angles.

The tunability of haze factor is important for solar cells because a high haze factor is desirable for increasing the coupling of light into the absorber.

Lastly, various durability tests were performed to evaluate the robustness of the Ag NM/MG in applications. Figure 32(a) shows the variation in the resistance of two Ag NM/MG samples on PET substrates after both bending in compression and tension. Two Au contacts were deposited on the samples using an e-beam evaporator, and the resistance between the two contacts was monitored after bending. The samples were bent around a steel rod with 1 cm diameter with the structure toward and away from the rod for compression and tension tests, respectively. The samples for both bending tests have a geometry of a_{NM} = 2000 nm, and w_{NM} = 100 nm, t_{NM} = 30 nm, a_{MG} = 500 μm, w_{MG} = 10 μm, and t_{MG} =

1 μm. The original resistance of the samples prepared for the tension and compression tests are 4.3 Ω/sq and 4.0 Ω/sq, respectively. After 200 cycles of bending, the sheet resistance for the samples are 6.1 Ω/sq and 5.3 Ω/sq, corresponding to a 39.5% and 32.5% increase, respectively. The degradation of the sample is mainly due to the delamination of the Ag MG from the substrate, as shown in Figure 32(b)(i). The Ag NM, which is more resilient under bending,[7] is mostly intact after the bending test, as shown in Figure 32(b)(ii). The flakes on the substrate in Figure 32(b)(ii) are the SiO_2 protection layer for PET partially peeled off from the substrate through the bending test.

Figure 32(c) shows the change in resistance of a Ag NM/MG on PET substrate after the heating test. The sample has a_{NM} = 2000 nm, w_{NM} = 150 nm, t_{NM} = 30 nm, a_{MG} = 500 μm, w_{MG} = 10 μm, and t_{MG} = 1 μm. After continuous heating for 168 h on a hot plate at 65 °C, the resistance of the sample changed from 2.0 to 2.7 Ω/sq increasing by 35%. Ag is prone to oxidation and passivation of the sample may help reduce sheet resistance degradation, especially at higher temperatures.[150]

5.2.2 Conclusions

In conclusion, we reported both simulations and experiments on hierarchical Ag NM/MG for transparent conductors. We investigated their transparency and sheet resistance and evaluated the potential of these structures as transparent conductors. Simulations compare reasonably to experimental results and can be used to guide the design of the hierarchical structures. Experimentally, we demonstrate a scalable method to fabricate Ag NM/MG on both rigid quartz substrates and flexible PET substrates. The samples demonstrate good uniformity and ordering, with performance superior to ITO. The haze factor of the hierarchical structure as transparent conductors can be tuned to suit the requirements for different applications. Durability tests demonstrate that the hierarchical structures are not significantly sensitive to bending and heating.

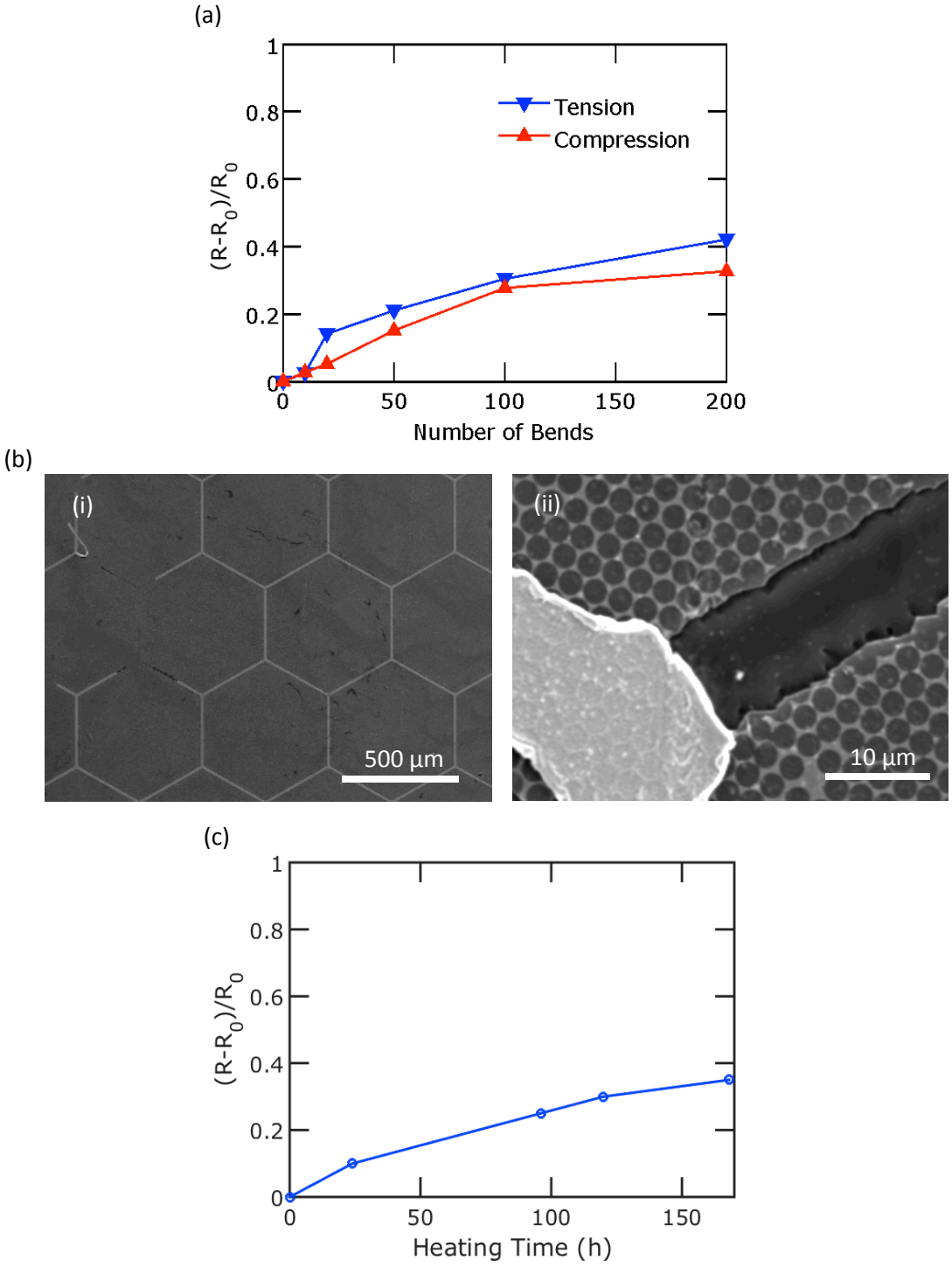

Figure 32: Durability tests for Ag NM/MG on PET substrates. (a) Resistance change versus number of bends for Ag NM/MG on PET substrates. The bending curvature is 0.5 cm. (b) SEM image for the sample after bending test. (c) Resistance change versus heating time for Ag NM/MG on PET substrate heated at 65°C in air.

6.0 TRANSPARENT CONDUCTORS IN SOLAR CELLS

In the previous chapters, we systematically studied a variety of TC materials based on nanoscale and microscale materials and demonstrate colossal FoM. However, Sciacca *et al* pointed out that the abuse of FoM may lead to partial evaluation of TC materials and real devices must be built to compare the performance of TCs.[151] In this chapter, we propose a functional TC materials for thin film silicon solar cells. As a key component for solar cells, TCs not only functions as a transparent layer that collects and delivers photogenerated charge carriers with minimal loss, but act as a good source of light trapping, which is of paramount importance for thin film solar cells. Nanoscale Ag hemisphere array is first studied as the preliminary work to understand the light trapping mechanisms by the incorporation of nanoscale metal structures. Metal NM sandwiches are then investigated as both light trapping elements and excellent TCs.

6.1 AG HEMISPHERE ARRAYS FOR LIGHT TRAPPING

6.1.1 Schematic and Methodology

Figure 33 shows a schematic of the system we studied. The photoactive region consists of a c-Si ultrathin film with thickness t_{Si}. A two dimensional (2D) array of Ag hemispheres sits on top of the silicon thin film. The arrays are defined by the diameter of the hemisphere d and the pitch a of the square lattice. We investigated c-Si thin films with $t_{Si} = 100$ nm and hemispheres with diameter $d = 50$ to 500 nm and pitches a from 50 to 500 nm, where $d \leq a$. The two parameters were varied in 5 nm increments.

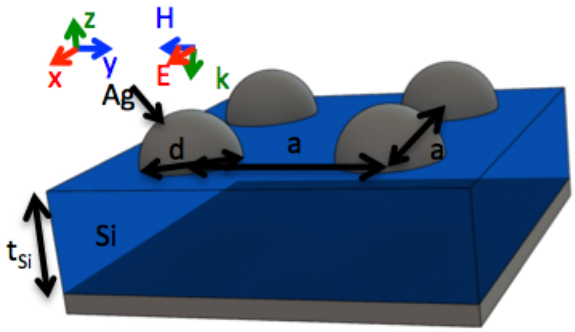

Figure 33: Schematic of the plasmonic solar cell structure. A square array of hemispheres of diameter d and pitch a sit on top of a crystalline silicon thin film of thickness t_{Si} on a perfect back reflector.

We performed electrodynamic simulations by solving Maxwell's equations using the finite-difference time-domain (FDTD) method.[152] We used a perfectly matched layer for the top boundary condition of the simulation supercell and a perfectly reflecting boundary, representing an ideal metal back contact for the bottom boundary condition. The side boundary conditions of the supercell were set to be antisymmetric and symmetric in the direction of the electric and magnetic field respectively to model the periodic nature of the Ag hemispheres. We also utilized a non-uniform simulation mesh with a finer mesh near interfaces and larger mesh in bulk regions. The optical constants for the crystalline Si and Ag were taken from experimental results in Palik's *Handbook of Optical Constants of Solids*.[153]

The position dependent absorption per unit volume $A(\mathbf{r}, \lambda)$ was calculated from the divergence of the Poynting vector $\mathbf{P}$ normalized over the incoming radiation power $P_{in}(\lambda)$:

$$A(\mathbf{r}, \lambda) = \frac{1}{2} \frac{\text{real}\{\vec{\nabla} \cdot \mathbf{P}\}}{P_{in}(\lambda)} = \frac{1}{2} \frac{\epsilon_i(\lambda)\omega(\lambda) \left|\mathbf{E}(\mathbf{r}, \lambda)\right|^2}{P_{in}(\lambda)} \tag{6.1}$$

where λ is the free-space wavelength, $\epsilon_i(\lambda)$ is the imaginary part of the permittivity, $\omega(\lambda) = 2\pi c/\lambda$ is the photon angular frequency, c is the speed of light, and $\mathbf{E}(\mathbf{r}, \lambda)$ is the electric field vector as the function of position and wavelength. The absorption spectra $A(\lambda)$ of the Si photoactive region was obtained by integrating the position dependent absorption per unit volume over the Si volume, $A(\lambda) = \int A(\mathbf{r}, \lambda) dV_{Si}$. This eliminates any parasitic absorption

that may occur in the Ag hemispheres that does not contribute to solar efficiency. Likewise, the parasitic absorption spectra of the metal hemispheres was obtained by integrating the position dependent absorption per unit volume over the Ag volume, $A_{Ag}(\lambda) = \int A(\mathbf{r}, \lambda) dV_{Ag}$. Assuming that each absorbed photon generates one electron-hole pair, and that all photo-generated carriers are collected, the short-circuit current density is

$$J_{sc} = q \int_0^{\lambda_g} I(\lambda) A(\lambda) \frac{\lambda}{\lambda_g} d\lambda. \tag{6.2}$$

$\lambda_g = 1107$ nm is wavelength corresponding to the band gap of c-Si ($E_g = 1.12$ eV), and $I(\lambda)$ is the solar irradiance under the global 37° tilt Air Mass 1.5 spectrum.[95]

6.1.2 Results and discussion

Figure 34(a) plots the absorption spectra of a $t_{Si} = 100$ nm c-Si film on a perfect back reflector. For thin film systems, FP modes are supported where the resonant wavelengths are sensitive to thickness. Maxwell's equations may be solved with appropriate boundary conditions to determine that FP modes occur for a Si thin film on a perfect conductor when the following condition is satisfied:

$$\tan(n_{Si} k t_{Si}) = -n_{Si} i \tag{6.3}$$

where k is the free space wave number and n_{Si} is the silicon index of refraction. The FP modes[154] are TEM modes labelled with mode number m as TEM_m. The thin film absorption resonances for $m = 2$ and 1 at $\lambda = 410$ and 550 nm respectively are marked in Figure 34(a) with white dashed lines. The electric field intensity $|\mathbf{E}(\mathbf{r}, \lambda)|^2$ is plot in Figure 34(b) for the (i) TEM_2 and (ii) TEM_1 mode. These resonant modes are characterized by $m + 1/2$ half wavelengths in the transverse direction of the planar film, where the electric field intensity is maximum at the front surface and 0 at the back metal interface. Light absorption is increased by constructive interference in the Si thin film at these particular wavelengths.

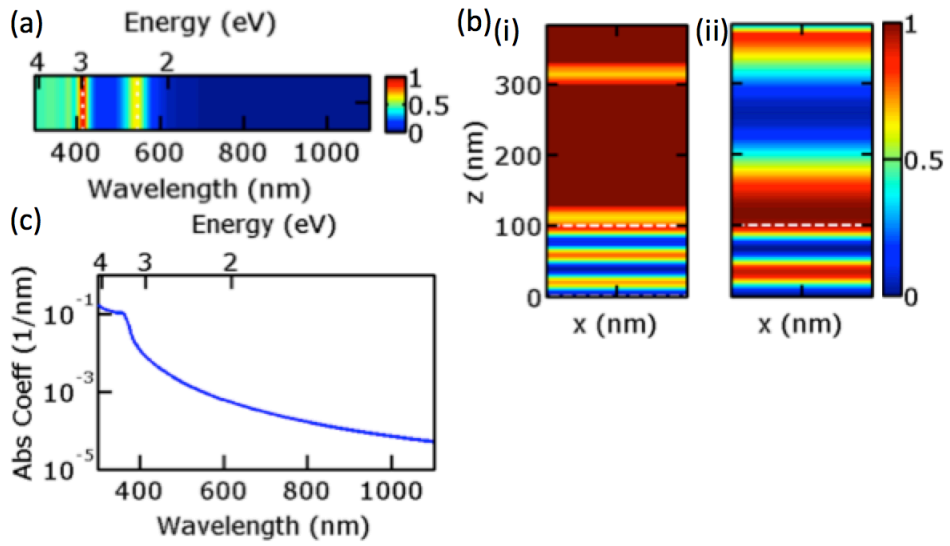

Figure 34: (a) Absorption spectra of $t_{Si} = 100$ nm c-Si film on a perfect back reflector. The FP modes are marked with white dashed lines and correspond to the TEM_2 and TEM_1 mode at $\lambda = 410$ and 550 nm respectively. (b) Electric field intensity $|\mathbf{E}(\mathbf{r}, \lambda)|^2$ of the (i) TEM_2 and (ii) TEM_1 modes.

Figure 35(a) plots the absorption in the Si as a function of the pitch a from 170 to 400 nm and the free-space wavelength. Apart from the FP modes of the film, which are again plot with white dashed lines, introducing Ag hemisphere arrays on the front of the c-Si thin film allows for the excitation of waveguide modes and plasmons. The TE waveguide modes for a thin film of Si on a perfect conductor satisfy

$$k_{Si} \cot(k_{Si} t_{Si}) = i k_x \tag{6.4}$$

where k_{Si} and k_x are the traverse waves in the Si and air respectively, $k_{Si} = (n_{Si}^2 k^2 - \beta^2)^{1/2}$ and $k_x = (k^2 - \beta^2)^{1/2}$. β is the propagation constant. The TM modes for a thin film of Si on a perfect conductor satisfy

$$i k_{Si} \tan(k_{Si} t_{Si}) = n_{Si}^2 k_x. \tag{6.5}$$

The periodicity of the Ag hemisphere arrays allows light to couple to waveguide modes in the Si thin film when $\beta = \frac{2\pi}{a}$. Equations 6.4 and 6.5 reduce to Equation 6.3 when $\beta = 0$.

The analytical solutions of the TM_0, TE_0, TM_1, and TE_1 mode are plot with black dashed lines in Figure 35(a). As $a \to \infty$ and $\beta \to 0$, the TE_0 and TM_0 modes converge to the TEM_0 mode at $\lambda = 1350$ nm and the TE_1 and TM_1 modes converge to the TEM_1 mode at $\lambda = 550$ nm. Higher order modes may also be excited at lower wavelengths (higher energies) when $\beta = \frac{2\pi}{a}\frac{1}{\sqrt{n^2+p^2}}$, where n and p are integers. The TM_0 and TE_0 modes are plot for $n = 1$, $p = 1$ as well as for $n = 2$, $p = 0$ (or $n = 0$, $p = 2$) with gray dashed lines. The simulated modes are slightly blue shifted compared to the analytical solution due to the presence of the metal on the front side of the silicon.

Figure 35(b) plots the absorption in the metal hemisphere as a function of the pitch a from 170 to 400 nm and the free-space wavelength. The FP modes and waveguide modes are plot with dashed lines as before. Light is efficiently coupled into the FP modes where there is little absorption in the metal. It can be seen there is a some increased absorption in the metal when the incoming light is scattered into the waveguide modes. In addition, a pitch-dependent absorption enhancement in both the Si and the metal hemispheres can be seen at longer wavelengths in the neighborhood of $\lambda = 1000$ nm. This absorption enhancements corresponds to a localized surface plasmon resonance, based on analysis of the electric field intensity and its angle-dependence that will be discussed later. The absorption is enhanced in both the metal and in the Si at this wavelength due to a strong local field enhancement around the metal hemisphere.

The maximum short circuit current was obtained at $a = 245$ nm and this is indicated by the white dash-dotted line in Figure 35(a). The absorption spectra for this pitch is plot in Figure 35(c) along with the absorption spectra for the Si thin film without the Ag hemispheres. The short-circuit current for c-Si with the selected Ag hemisphere array is $J_{sc} = 60.8$ mA/cm^2, which is a a 21.7% enhancement compared to the bare c-Si thin film, which has $J_{sc} = 50.0$ mA/cm^2 The absorption enhancement $g(\lambda) = A_h(\lambda)/A_{bare}(\lambda)$ is plot in Figure 35(d) where $A_{bare}(\lambda)$ and $A_h(\lambda)$ are the absorption spectra of the plain Si and with the hemispheres respectively. Four enhancement peaks at $\lambda = 620, 680, 750$, and 1000 nm can be seen.

The three resonance modes at $\lambda = 620$, 680, and 750 nm correspond to the excitation of waveguide modes in the c-S and exhibit absorption enhancements of 4.3, 6.5, and 9.9 times

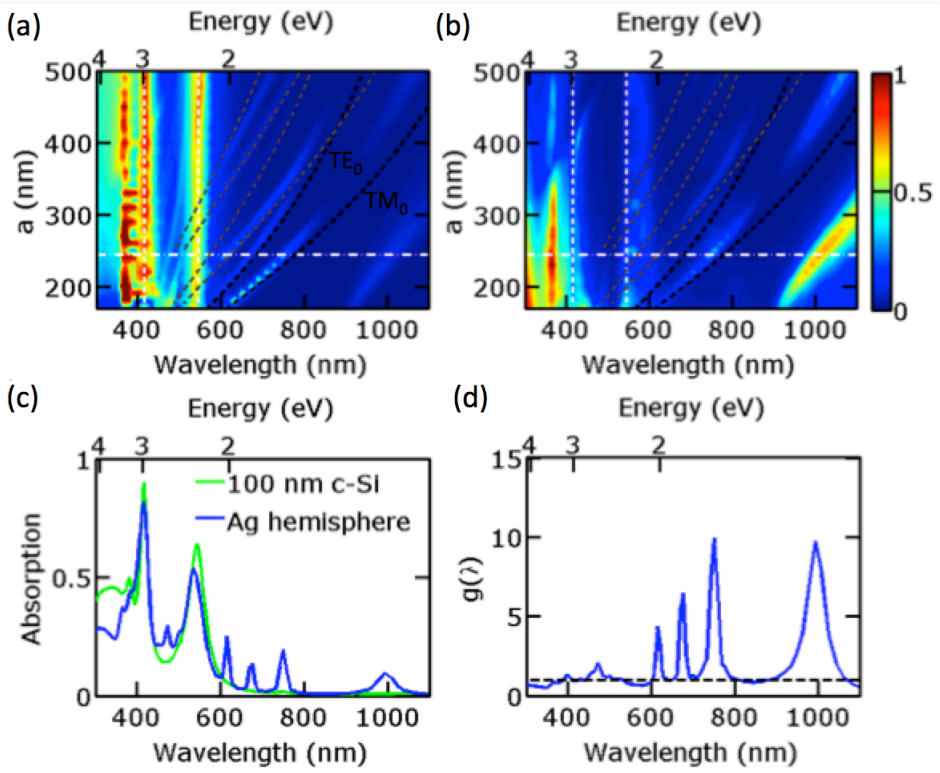

Figure 35: Absorption in (a) the Si and (b) the Ag hemispheres for a 2D Ag hemisphere array of diameter $d = 170$ nm and different pitches a from 170 nm to 400 nm on $t_{Si} = 100$ nm c-Si thin film on a perfect back reflector. (c) Absorption as the function of wavelength for 100 nm thick c-Si layer with and without the Ag hemispheres at $a = 245$ nm (indicated by the white dash dotted line in a). (d) The absorption enhancement $g(\lambda)$ due to the hemispheres as a function of wavelength.

respectively compared to that of a $t_{Si} = 100$ nm c-Si thin film. Fig. 36 plots the electric field intensity $|\mathbf{E}(\mathbf{r}, \lambda)|^2$ at $\lambda =$ (a) 620, (b) 680, and (c) 750 nm. The electric field of the incident light is in the positive x-direction and the magnetic field in the negative y-direction in these plots as indicated in the schematic in Fig. 33. The top row in Fig. 36 shows the electric field intensity through the center of the c-Si at $z = 50$ nm and the bottom row shows the electric field intensity through the center of one of the hemispheres along $y = 0$. The mode at $\lambda = 620$ nm corresponds to a TM_0 mode with $n = 1$ and $p = 1$. The mode at $\lambda = 750$ nm is also a TM_0 mode, but with $n = 0$ and $p = 1$ (or $n = 1$ and $p = 0$). The profile of these modes in the $z-$direction resemble each other, but the mode at $\lambda = 615$ nm has periodicity in both the $x-$ and $y-$ directions, while the mode at $\lambda = 751$ nm only has periodicity in the $x-$direction. In addition, the mode at $\lambda = 680$ nm is a TE_0 mode with $n = 0$ and $p = 1$ (or $n = 1$ and $p = 0$). This mode has one period in the $y-$direction. The metal hemispheres on the front surface of the c-Si film allows light to couple to waveguide modes in the c-Si film, where the mode energy is concentrated in the Si layer, leading to an absorption enhancement.

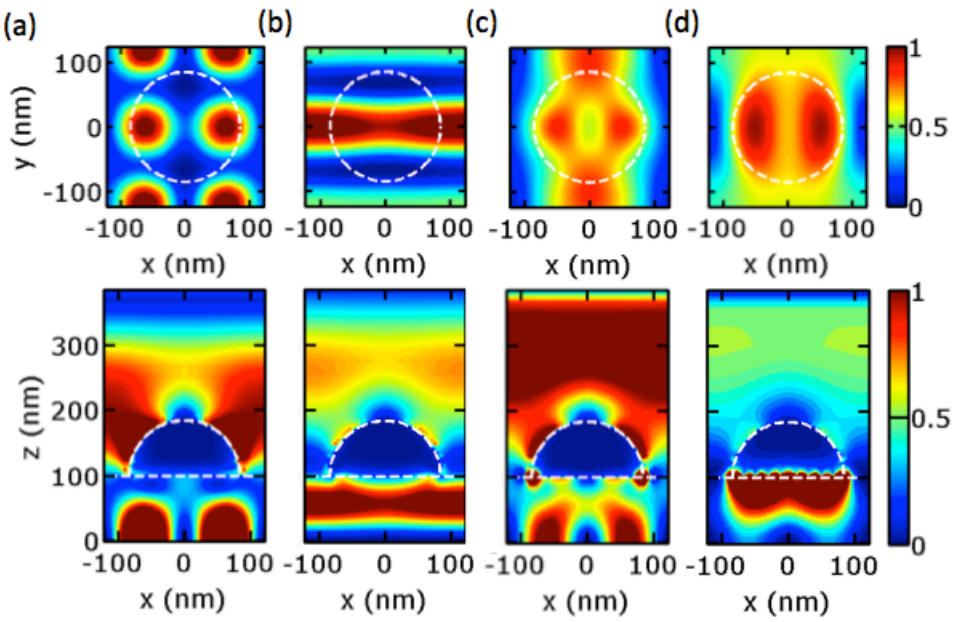

Figure 36: Electric field intensity profile $|\mathbf{E}(\mathbf{r},\lambda)|^2$ at $\lambda =$ (a) 620, (b) 680, (c) 750 nm, and (d) 1000 nm. The top row shows a slice in the $x-y$ plane at $z = 50$ nm and the bottom row shows an $x-z$ slice at $y = 0$. (a) and (c) are TM_0 modes, while (b) is a TE_0 mode. (d) is a localized surface plasmon resonance.

The resonance mode at $\lambda = 1000$ exhibits an enhancement of about 10 times compared to that of a $t_{Si} = 100$ nm c-Si thin film. The electric field intensity at $\lambda = 1000$ nm is shown in Fig. 36(d). This concentration of light inside the Si film is induced by a surface plasmon, where the electric field intensity decays exponentially into the c-Si layer away from the Ag and c-Si interface. The parasitic absorption in the metal is significant at this wavelength and about 76%. This mode shifts to higher wavelengths (lower energies) with increasing pitch due to the electromagnetic interaction between neighboring hemispheres. We found that this resonance peak exhibits some pitch dependence for pitches below 500 nm.

Finally, we studied the angle-dependent absorption behavior in the hemisphere array structures. Fig. 37 plots the angle dependence of the absorption from 0° to 35° for the structure with $d = 170$ nm and $a = 245$ nm for (a) TE- and (b) TM-polarized incident light. The fundamental TM_0 mode at $\lambda = 750$ is only dependent on incidence angle for TM-incident light, while the fundamental TE_0 mode at $\lambda = 680$ nm is only dependent on

incidence angle for TE-incident light. In contrast, the higher order TM_0 mode at $\lambda = 620$ nm is dependent on incidence angle for both TE- and TM-incidence light since $n = 1$ and $p = 1$. The LSPR is independent of incidence angle for both TE- and TM-incident light. The short circuit current is shown in Fig. 37 and is almost constant for oblique incident light. Furthermore, the angle dependence of the short circuit current is similar for TE and TM-polarized incident light.

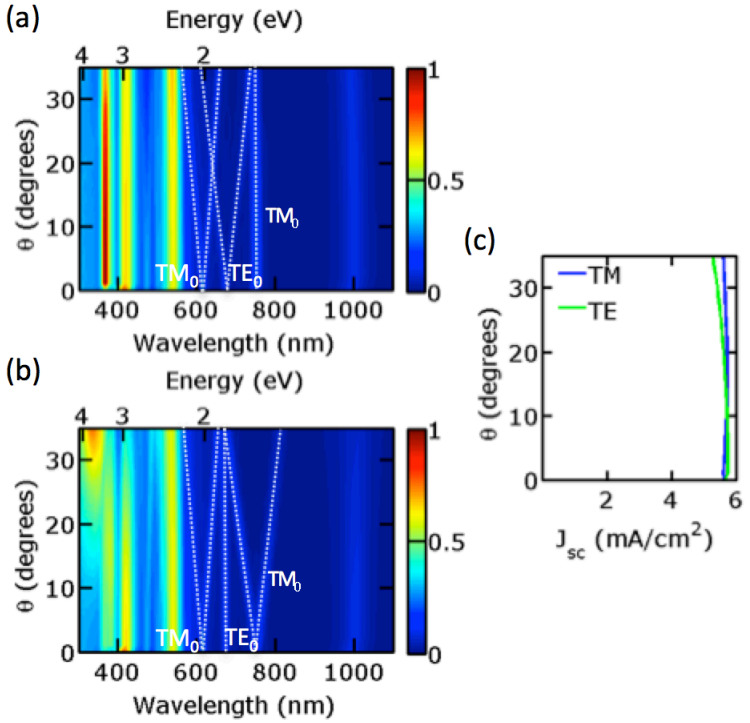

Figure 37: Absorption spectra of $d = 170$ nm, $a = 245$ nm Ag hemisphere array on $t_{Si} = 100$ nm thin film on perfect back reflector as a function of wavelength for (a) TE-incident light and (b) TM-incident light. (c) Short-circuit current density J_{sc} as a function of incident angle.

6.1.3 Conclusion

In summary, we investigated the design of 2D Ag hemisphere arrays for plasmonic c-Si ultrathin film solar cells. Structures with a broad range of parameters were systematically studied and the best structure with 21.7% integrated enhancement in short-circuit current

compared to bare c-Si solar cell was observed. Three types of resonance modes: (1) FP, (2) waveguide, and (3) LSPR are supported by the studied structure. FP modes may be excited in bare c-Si solar cells, but the introduction of 2D hemisphere arrays introduces waveguide and LSPR modes that lead to enhanced absorption compared to bare c-Si solar cells. The resonance modes can be conveniently tuned by varying Ag hemisphere array pitch. We also studied the angle-dependence of the absorption in these structures and demonstrate how the absorption resonances shift with incidence angle.

6.2 METAL NANOMESH SANDWICH FOR SOLAR CELLS

We report on numerical investigations of the optical absorption and short-circuit current densities of ultrathin c-Si solar cells with the incorporation of metal NPs or NMs into the top and/or bottom of the c-Si. The properties for c-Si thin film with an antireflection coating (ARC) and/or a flat back reflector as well as an ideal double pass c-Si thin film were simulated for benchmarking. The results were compared with the properties for ultrathin c-Si solar cells with metal NPs/NM on either side. We demonstrate that metal NMs may function as both a plasmonic light trapping element and a transparent top electrode when deposited on the top side of the ultrathin c-Si film, and as effective back reflector when placed on the back side. A variety metals, including Ag, Au, Cu, Al, and Ni, have been used to investigate the plasmonic effects when contacting dielectrics.[155–157] We studied the effect of nanostructured Al and Ag for ultrathin c-Si solar cells, because Au introduce states near the middle of the Si band gap that serve as highly effective recombination centers and Cu diffuses rapidly into c-Si even at room temperature. Our results shed light on the design principles of these structures for improved c-Si solar cell performance.

6.2.1 Schematic and Methodology

Figure 38(a) illustrates schematics of the four types of systems studied: ultrathin c-Si film with (i) frontside metal NM/NPs, (ii) backside metal NM, (iii) metal NM sandwich, and

(iv) metal NM sandwich with antireflection coating. The parameters for the various systems studied are illustrated in Figure 38(b). The photoactive region consists of an ultrathin c-Si film with thickness t_{Si}. The metal NMs are metal thin films with holes in a hexagonal array. The top NM is defined by the pitch a_{top}, hole diameter d_{top}, and metal thickness t_{top}. The bottom NM is defined by the pitch a_{bot}, hole diameter d_{bot}, and metal thickness t_{bot}. For simplicity, we assume the top and bottom pitch are equal, $a_{top} = a_{bot} = |\vec{a_1}| = |\vec{a_2}|$. The thickness of the antireflection coating is t_{ARC}, and the x and y component of the off-shift between the top and bottom NM lattice are denoted by u and v respectively (not shown in the schematic). As a proof-of-concept, we investigate ultrathin c-Si film with t_{Si} = 300 nm and metal NMs with pitch $a_{top} = a_{bot} = a$ = 200 to 1000 nm, and hole diameter d_{top} and d_{bot} = 200 to 1000 nm, where d_{top} and $d_{bot} \leq a$.

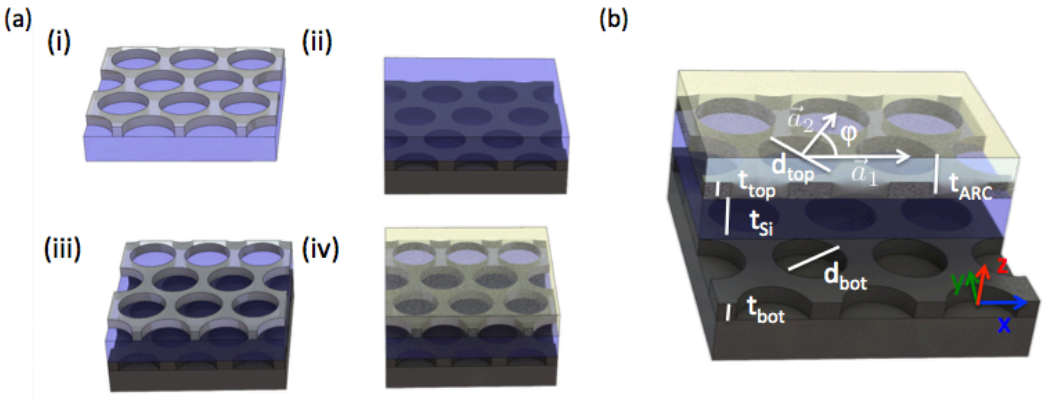

Figure 38: Schematics of the plasmonic solar cell structures studied, including (a) ultrathin c-Si film with (i) frontside metal NM or NPs, (ii) backside metal NM, (iii) metal NM sandwich, and (iv) metal NM sandwich with antireflection coating and backside metal. (b) Parameters of the various structures studied.

We performed electrodynamic simulations to determine the optical properties of solar cells by solving Maxwell's equations using the finite-difference time-domain (FDTD) method.[91, 152] We used a perfectly matched layer as the top and bottom boundary condition to truncate the simulation super cell. The side boundary conditions of the supercell were set to be antisymmetric and symmetric in the direction of the electric and magnetic field

respectively to model the periodic nature of the metal NMs. We also utilized a non-uniform simulation mesh with a finer mesh near interfaces and larger mesh in bulk regions. The optical constants for the c-Si, Ag, and Al were taken from experimental results in Palik's *Handbook of Optical Constants of Solids*[153] and the refractive indices for silicon nitride were taken from Ref. [158].

The position dependent absorption per unit volume $A(\mathbf{r},\lambda)$ was calculated from the divergence of the Poynting vector $\mathbf{P}$:

$$A(\mathbf{r},\lambda) = \frac{1}{2}\text{real}\{\vec{\nabla}\cdot\mathbf{P}\} = \frac{1}{2}\epsilon_i(\lambda)\omega(\lambda)\left|\mathbf{E}(\mathbf{r},\lambda)\right|^2 \tag{6.6}$$

where λ is the free-space wavelength, $\epsilon_i(\lambda)$ is the imaginary part of the permittivity, $\omega(\lambda) = 2\pi c/\lambda$ is the photon angular frequency, c is the speed of light, and $\mathbf{E}(\mathbf{r},\lambda)$ is the electric field vector as the function of position and wavelength. The absorption spectra $A(\lambda)$ of the Si photoactive region was obtained by integrating the position dependent absorption per unit volume over the Si volume, $A(\lambda) = \int A(\mathbf{r},\lambda)dV_{Si}$. This eliminates any parasitic absorption that may occur in the metal that does not contribute to solar efficiency. Assuming that each absorbed photon generates one electron-hole pair, and that all photogenerated carriers are collected, the short-circuit current density is

$$J_{sc} = q\int_0^{\lambda_g} I(\lambda)A(\lambda)\frac{\lambda}{\lambda_g}d\lambda. \tag{6.7}$$

$\lambda_g = 1107$ nm is the free-space wavelength corresponding to the band gap of c-Si ($E_g = 1.12$ eV), and $I(\lambda)$ is the solar irradiance under the global 37° tilt Air Mass 1.5 spectrum.[95]. We use the FDTD method to determine the transmission of the frontside NM as the transparent electrode, and the finite element method to simulate the sheet resistance R_s by solving the transport equation. The resistivity of bulk metals is assumed in these simulations. Solar integrated transmission is calculated from

$$T_{solar} = \frac{\int b(\lambda)T(\lambda)d\lambda}{\int b(\lambda)d\lambda}, \tag{6.8}$$

where $b(\lambda)$ is the photon flux density under the global 37° tilt Air Mass 1.5 spectrum, and $T(\lambda)$ is the wavelength dependent optical transmission. To compare different geometries, we utilize the angle-averaged short-circuit current density $J_{sc} = (J_{sc,xx} + J_{sc,yy})/2$, where

$J_{sc,xx}$ and $J_{sc,yy}$ are the short-circuit-current density under illumination polarized in the x- and y-directions respectively. Similarly, we calculate the angle-averaged sheet resistance $R_s = (R_{s,xx}+R_{s,yy})/2$, and angle-averaged transmission $T_{solar} = (T_{solar,xx}+T_{solar,yy})/2$, where $R_{s,xx}$ and $R_{s,yy}$ are the sheet resistances measured in the x- and y-direction; $T_{solar,xx}$ and $T_{solar,yy}$ are the transmission results under illumination polarized in the x- and y-directions, respectively.

6.2.2 Results and Discussion

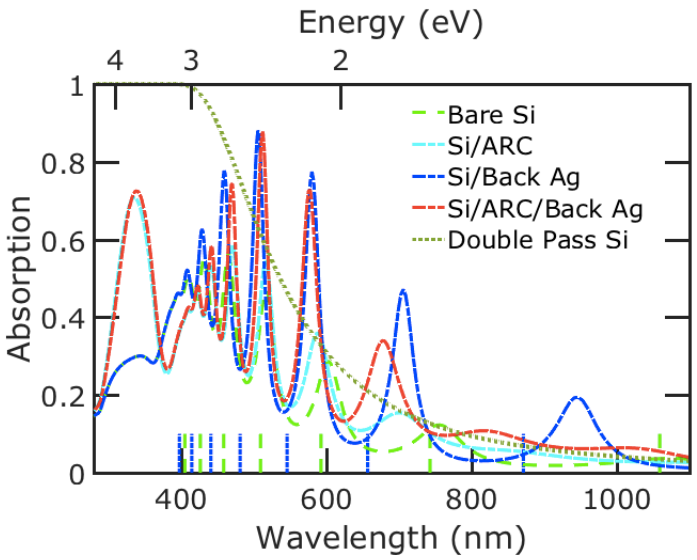

Figure 39: Absorption spectrum for 300-nm-thick bare c-Si, c-Si with 100 nm Si_3N_4 ARC, c-Si with Ag back reflector, c-Si with ARC and Ag back reflector, and ideal double pass c-Si.

We first investigated ultrathin c-Si films with various ARC and/or back reflectors. The five structures selected are bare c-Si film, c-Si thin film with 100-nm-thick Si_3N_4 as ARC, c-Si with 300-nm-thick Ag back reflector, c-Si with both ARC and Ag back reflector, and ideal double pass 300-nm-thick c-Si. Fig. 39 shows the absorption spectrum for these scenarios, where the short-circuit current density $J_{sc} = 6.0$, 7.1, 8.6, 9.4, and 11.0 mA/cm^2, respectively. The absorption near the band gap is weak due to the indirect band gap of c-Si, though multiple peaks are observed in the absorption spectra due to the Fabry-Pérot resonance supported

by thin film systems. Fabry-Pérot resonances occur for a c-Si thin film on a perfect electric conductor (PEC) when the following condition is satisfied:

$$\tan(n_{Si}kt_{Si}) = -n_{Si}i \tag{6.9}$$

where k is the free space wave number and n_{Si} is the refractive index of c-Si. For a free-standing thin film, the even modes occur when

$$\cot(n_{Si}k\frac{1}{2}t_{Si}) = n_{Si}i \tag{6.10}$$

and the odd modes occur at

$$\tan(n_{Si}k\frac{1}{2}t_{Si}) = -n_{Si}i. \tag{6.11}$$

The analytical solutions in both cases are plotted with dashed blue lines near the x-axis in Fig. 39. The numerically simulated resonances correspond well to the analytical solution, but are slightly red-shifted due to numerical error. The smaller the grid size used, the smaller the offset from the analytical solution. The resonance modes with the Ag back reflector are red-shifted compared to that with the PEC back reflector because the electromagnetic field extends slightly into the back Ag back reflector and thus, increases the effective film thickness slightly. In addition, we show the absorption spectra $A(\lambda)$ of a double pass c-Si film

$$A(\lambda) = 1 - \exp[2\alpha(\lambda)t_{Si}] \tag{6.12}$$

where $\alpha(\lambda)$ is the wavelength dependent absorption coefficient of c-Si. The ideal double pass thin film assumes perfect antireflection at the front surface, $R(\lambda) = 0$, and perfect reflection at the back surface, $R(\lambda) = 1$. The photon optical length, the distance a photon travels in the c-Si, is exactly twice the thickness of the Si. The short-circuit current density is $J_{sc} = 11.0$ mA/cm^2 in this case. Table 1 summarizes the short circuit current density results for these thin film structures.

Table 1: The short circuit current density J_{sc} of different ultrathin Si structures.

Structure	$\boldsymbol{J_{sc}}$ **(mA/cm^2)**
Si/ARC	7.1
Si/Ag Back Reflector	8.6
Si/ARC/Ag Back Reflector	9.4
Double Pass Si	11.0

6.2.2.1 Frontside NP/NM optimization The optimization for metal nanostructures on the top side of bare ultrathin c-Si film with $t_{Si} = 300$ nm shows that the greatest enhancement in J_{sc} is achieved by nanoparticles (NPs). NPs are defined by the condition $d_{top} = a_{top}$, such that the metal structures are not continuous and instead form triangular NPs. Specifically, Al NPs with $d_{top} = a_{top} = 800$ nm and $t_{top} = 200$ nm demonstrate the optimal results. The short-circuit current is $J_{sc} = 9.7$ mA/cm^2 with $J_{sc,xx} = 11.5$ mA/cm^2 and $J_{sc,yy} = 7.9$ mA/cm^2, corresponding to a 36.6% enhancement compared with ultrathin c-Si film with 100-nm-thick Si_3N_4 ARC.

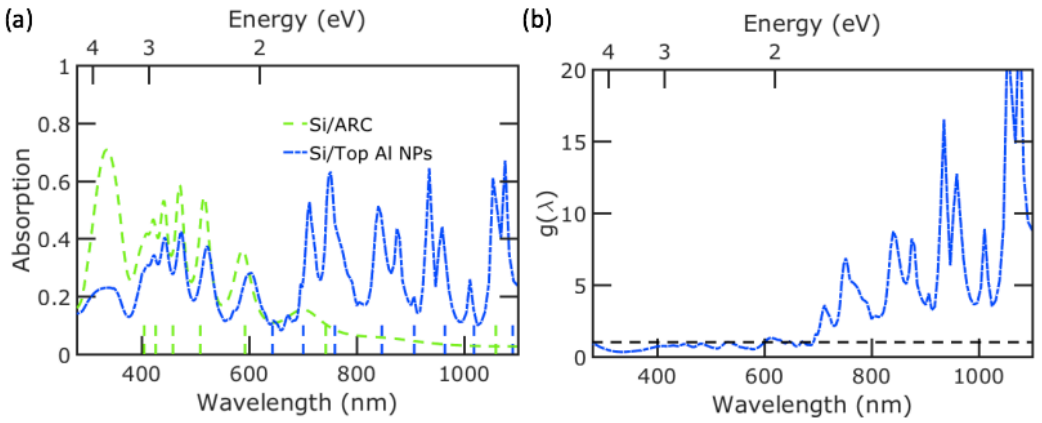

Figure 40: (a) Averaged absorption spectrum for ultrathin c-Si film with ARC and ultrathin c-Si film with frontside Al NPs. Fabry-Pérot and waveguide modes are plotted with green and blue dashed lines, respectively, near the x-axis. (b) The enhancement in optical absorption as a function of wavelength.

The guided TE waveguide modes for a Si thin film satisfy

$$k_{Si}\tan(k_{Si}\frac{1}{2}t_{Si}) = k_x \tag{6.13}$$

and

$$k_{Si}\cot(k_{Si}\frac{1}{2}t_{Si}) = -k_x \tag{6.14}$$

for even and odd modes, respectively. k_{Si} and k_x are the transverse waves in the Si and air respectively, where $k_{Si} = (n_{Si}^2k^2 - \beta^2)^{1/2}$ and $k_x = (\beta^2 - k^2)^{1/2}$. β is the propagation constant. The guided TM waveguide modes for a Si thin film satisfy

$$k_{Si}\tan(k_{Si}\frac{1}{2}t_{Si}) = n_{Si}^2k_x \tag{6.15}$$

and

$$k_{Si}\cot(k_{Si}\frac{1}{2}t_{Si}) = n_{Si}^2k_x \tag{6.16}$$

for even and odd modes, respectively. Incident light may couple to to the guided modes, which become quasiguided or leaky,[159] when the propagation constant matches the reciprocal lattice constant, $\beta = \frac{4\sqrt{3}\pi}{3a}\sqrt{p^2 - pq + q^2}$, where p and q are integers. Figure 40(a)

plots the absorption spectra results for the optimized frontside NPs compared with just the Si thin film. Fig. 40(a) plots the TEM Fabry-Pérot modes and waveguide modes up to $|p|$ and $|q| = 2$ with green and blue dashed lines, respectively, near the x-axis. The peak at 674 nm corresponds to a TE waveguide mode where $(p, q) = (3, -2), (2, -3), (-2, 3)$ or $(-3, 2)$ and the absorption peak at 935 nm is a $(3, 3)$ or $(-3, -3)$ TE waveguide mode. The mode at $\lambda = 792$ nm is a $(3, -2), (2, -3), (-2, 3)$ or $(-3, 2)$ TM waveguide mode. An additional mode is present at $\lambda = 875$ nm which is unaccounted for by this simple waveguide model. Peaks with over a 10-fold enhancement are observed near the band gap of c-Si as shown in Fig. 40(b).

Apart from Fabry-Pérot modes and waveguide modes, a localized surface plasmon resonance (LSPR) is excited by the Al NPs at $\lambda = 712$ nm. The LSPR will lead to absorption enhancement in the c-Si thin film with little pitch dependence. Figure 41 shows the electric field profile at $\lambda = 712$ nm, in which the presence of LSPR is evident, demonstrated by a strong localized field intensity near the vertices of each NP[160].

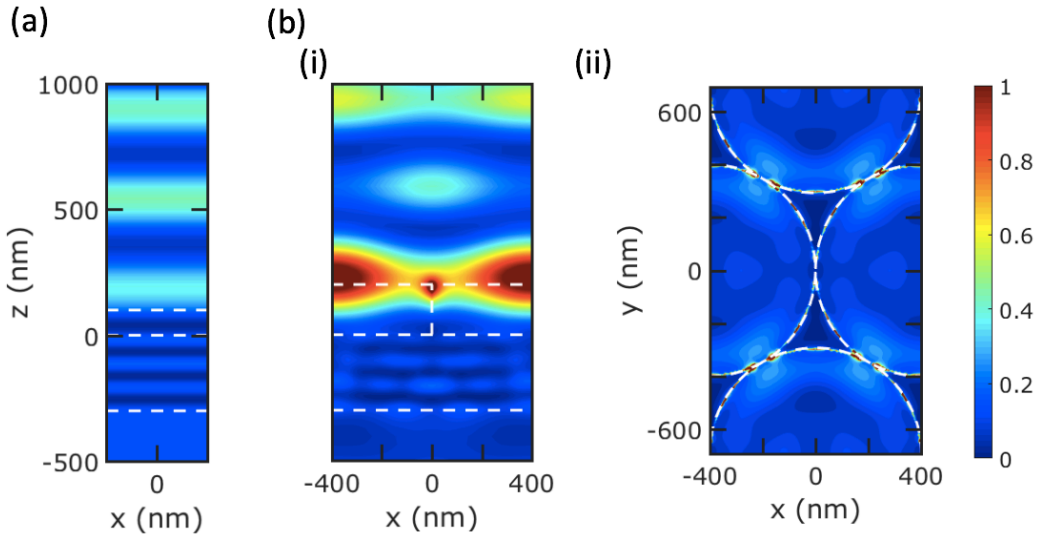

Figure 41: Normalized electric field intensity profiles at incident wavelength $\lambda = 712$ nm for (a) c-Si thin film with 100 nm ARC and (b) ultrathin c-Si film with frontside Al NPs. The cross-sectional view for the structure is shown in (i) the x-z plane at $y = 0$, and (ii) in the x-y plane at the Al/c-Si interface. The electric field profiles are the averaged result from incident light with polarization along x- and y- directions. The dashed white lines indicate where the c-Si film and Al NPs are located.

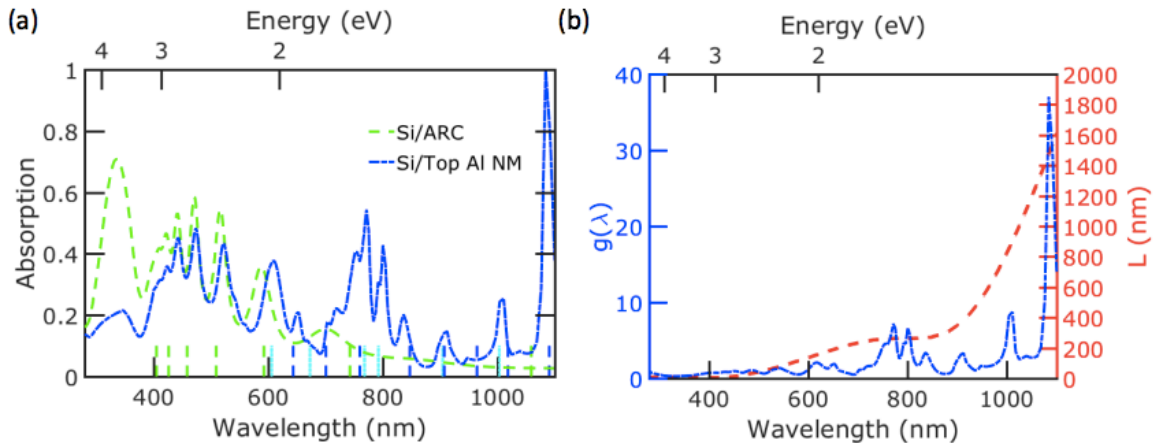

Figure 42: (a) Averaged absorption spectrum for ultrathin c-Si film with ARC and ultrathin c-Si film with frontside Al NM. (b) The enhancement in optical absorption $g(\lambda)$ in blue and the SPP propagation length L at an Al/c-Si interface as a function of wavelength in red.

By constraining $d_{top} < a_{top}$, the NPs become continuous NMs that may additionally function as a transparent conductor. We optimized the NMs and found that the most enhancement in J_{sc} is got by Al NM with a_{top} = 800 nm, d_{top} = 760 nm, and t_{top} = 100 nm. The short-circuit current is J_{sc} = 9.6 mA/cm^2 with $J_{sc,xx}$ = 9.6 mA/cm^2 and $J_{sc,yy}$ = 9.5 mA/cm^2, corresponding to a 35.2% enhancement compared with c-Si film with ARC. The enhancement with NMs is less than that with NPs because there is more top side metal in these structures and thus more reflection and parasitic absorption. The sheet resistance averaged over the x− and y− direction is 3.2 Ω/sq at a 83% average solar transmission. Figure. 42(a) plots Fabry-Pérot modes and quasiguided modes up to $|p|$ and $|q|$ = 2 with green and blue dashed lines, respectively, near the x-axis. In addition to coupling light to waveguide modes, the NM may excite SPPs. SPPs may be excited at normal incidence when the SPP wave vector matches the reciprocal lattice constant

$$\beta_{SPP} = k\sqrt{\frac{\epsilon_{Si}\epsilon_m}{\epsilon_{Si}+\epsilon_m}} \tag{6.17}$$

where ϵ_m and ϵ_{Si} are the complex permittivities for metal and dielectric, respectively.[161] $\beta_{SPP} = \frac{4\sqrt{3}\pi}{3a}\sqrt{m^2-mn+n^2}$. Figure 42(a) plots SPP modes with cyan dotted lines near the x-axis for modes up to $|m|$ and $|n|$ = 3.

The absorption enhancement is significant for incident light with larger wavelengths. A peak with over 30-fold enhancement is observed at $\lambda = 1084$ nm as shown in Fig. 42(b). Fig. 42(b) also plots the propagation length L of the SPP wave at an Al/c-Si interface in red on the right y-axis. SPPs can be excited at the interface separating metal and dielectric by the interaction between light and metal nanostructures. An SPP wave is lossy because the wave vector of SPP is greater than that of a freely propagating light at the same angular frequency ω. The traveling SPP wave at the interface attenuates exponentially with characteristic propagation length L, given by

$$L = (2\ \mathrm{Im}[\beta_{SPP}])^{-1}. \tag{6.18}$$

SPPs decay exponentially perpendicular to the interface. Incident light with longer wavelengths excites SPPs with larger propagation length.

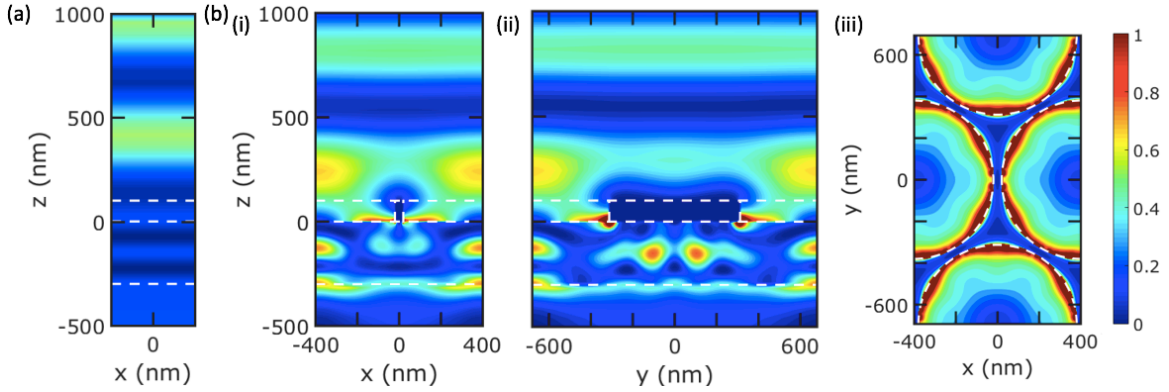

Figure 43: Normalized electric field intensity profiles at incident wavelength $\lambda = 1084$ nm for (a) bare ultrathin c-Si film and (b) ultrathin c-Si film with Al NM as transparent electrode. The cross-sectional view for the structure is shown in (i) the x-z plane at $y = 0$, (ii) in the y-z plane at $x = 0$, and (iii) in the x-y plane at the Al/c-Si interface. The electric field profiles are the averaged result from incident light with polarization along x- and y- directions. The dashed white lines indicate where the c-Si film and Al NM are located.

Figure 43 plots the electric field intensity at $\lambda = 1084$ nm. Fig. 43(a) plots the electric field intensity for just the Si thin film. The field pattern at this wavelength is close to one of the Fabry-Pérot modes (the TEM_2 mode at $\lambda = 1059$ nm where there is a single

wavelength in the transverse direction of the planar film). Fig. 43(b) plots the electric field intensity with the addition of the Al NM on top of the c-Si film in (i) the x-z plane at $y = 0$, (ii) in the y-z plane at $x = 0$, and (iii) in the x-y plane at the Al/c-Si interface. The electric field intensity plotted is an average for incident light polarized along the x- and y-directions. An SPP is excited with the presence of Al NM, indicated by the enhanced electric field intensity spatially confined near the Al/c-Si interface. This corresponds to the $(1, -2)$, $(2, -1)$, $(-1, 2)$, or $(-2, 1)$ SPP mode. The coupling of incident light and the SPP results in significant light trapping and absorption enhancement in the c-Si film.

6.2.2.2 Backside NM optimization Next, we evaluate metal NMs as effective back reflectors for ultrathin c-Si film solar cells. Specifically, we study a solar cell consisting of $t_{Si} = 300$ nm ultrathin c-Si film with metal NM on 100 nm Ag back reflector as the backside, as shown in Fig. 33(a)(ii). This is compared with an ultrathin c-Si film with 300 nm Ag thin film back reflector that was discussed earlier.

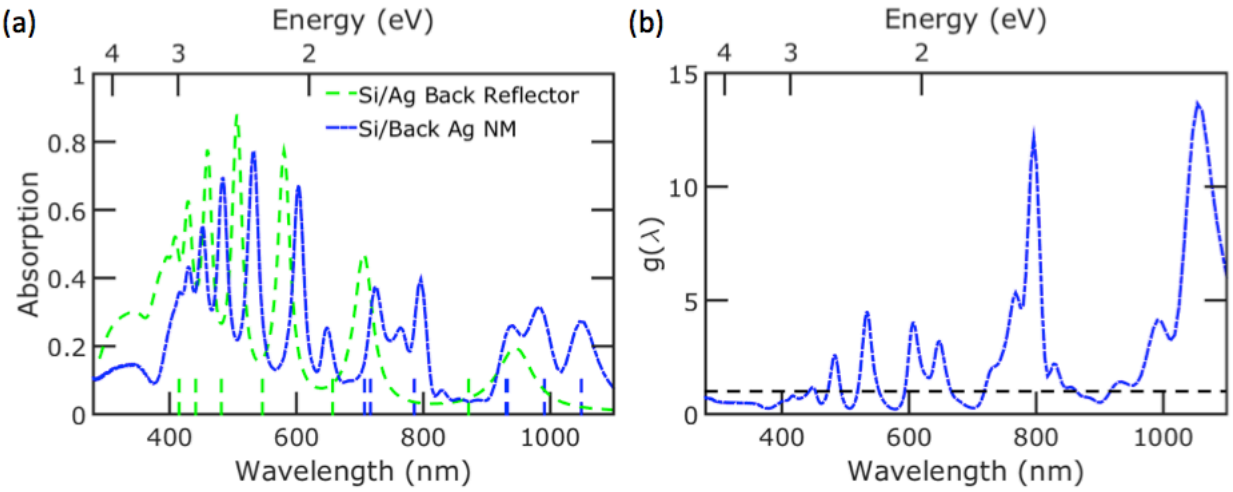

Figure 44: (a) Averaged absorption spectrum for ultrathin c-Si film with Ag film and optimal Ag NM as back reflector. Fabry-Pérot and waveguide modes are plotted with green and blue dashed lines, respectively, near the x-axis. (b) The enhancement of the absorption as a function of wavelength due to the Ag NM.

Fig. 44(a) plots the absorption spectra for the Ag thin film back reflector and the optimized Ag NM back reflector. The optimal solar cell performance is achieved by using a backside Ag NM with $a_{bot} = 900$ nm, $d_{bot} = 520$ nm, and $t_{bot} = 350$ nm. The short-circuit current density is $J_{sc} = 10.1$ mA/cm^2, with $J_{sc,xx} = 10.1$ mA/cm^2 and $J_{sc,yy} = 10.1$ mA/cm^2, exhibiting a 17.4% enhancement in J_{sc} compared with c-Si thin film with a 300 nm Ag back reflector.

For shorter wavelengths, the ultrathin c-Si film with Ag NM as back reflector supports the same thin film Fabry-Pérot resonance modes as its counterpart with 300 nm Ag thin film, but with redshifted and slightly weaker absorption peaks. The redshift of the peaks arises from the larger penetration of the electromagnetic field into the Ag NM back reflector due to the leaky nature. The absorption peaks for the c-Si with Ag thin film are stronger than with Ag NM. The location of the Fabry-Pérot resonance modes are plotted near the x-axis with green dashed lines.

Leaky waveguide modes are plotted in Fig. 44(a) with blue dashed lines near the x-axis for modes up to $|p|$ and $|q| = 2$. These leaky waveguide modes are plotted for freestanding silicon thin film without a back contact (Equations 6.13 to 6.16) since the electromagnetic field propagates into the holes of the metal NM. Figure 44(b) plots the absorption enhancement $g(\lambda)$ between the two structures shown in Figure 44(b). The guided modes contribute to the absorption enhancement in the long wavelength regime ($\lambda = 700$ to 1100 nm). An over 10-fold enhancement is observed near $\lambda = 796$ nm and 1046 nm.

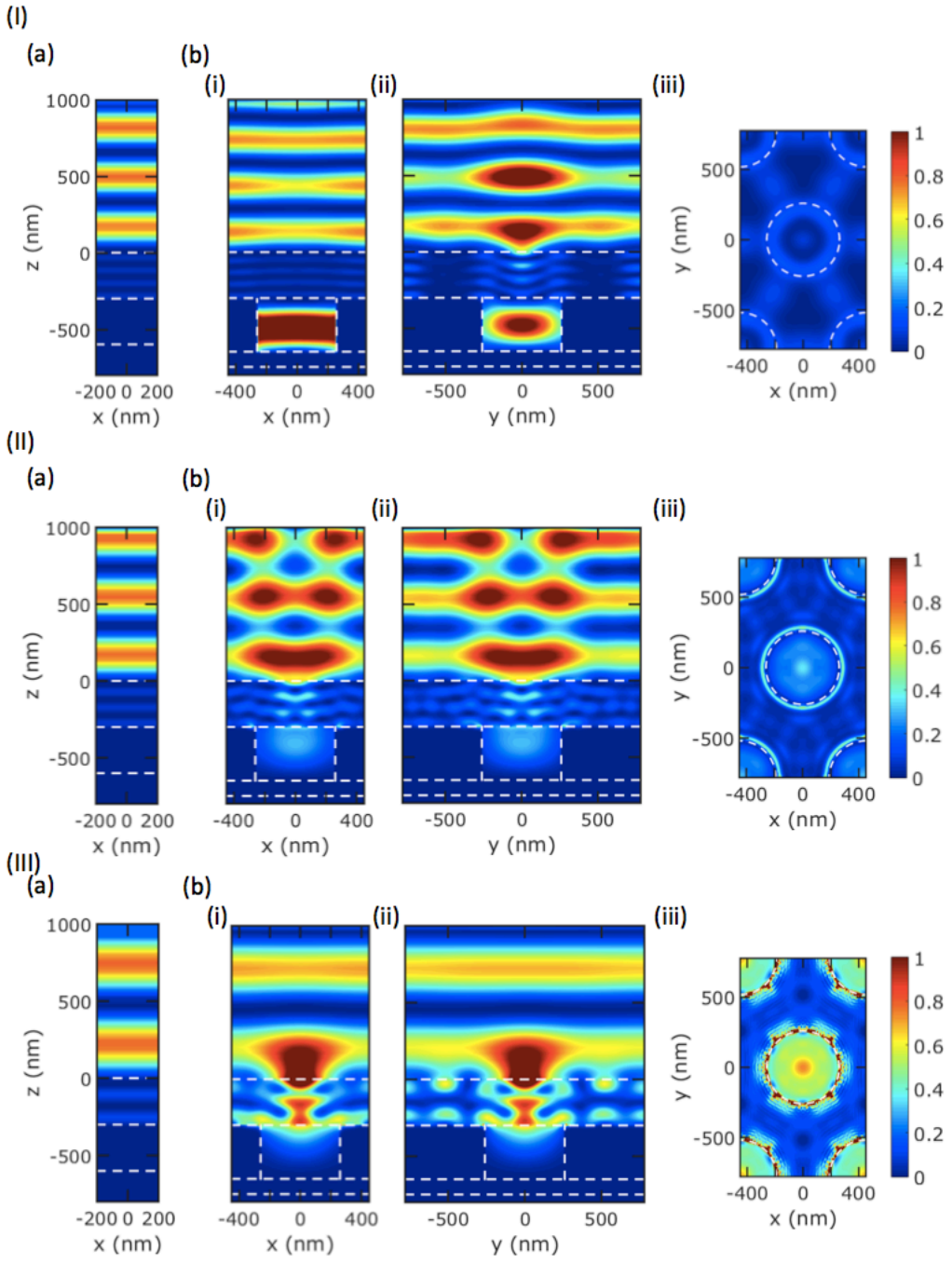

Figure 45: Normalized electric field intensity profiles at incident wavelength (I) $\lambda = 648$, (II) 764, and (III) 1046 nm for ultrathin c-Si film with (a) 300 nm Ag film and (b) optimal Ag NM as back reflector. The cross-sectional views for the structure in (i) the x-z plane with $y = 0$, (ii) the y-z plane with $x = 0$, and (iii) at the Ag NM/c-Si interface. The electric field profiles are the averaged result from incident light with polarization along x- and y-directions. The dashed white lines indicate the edges of where the c-Si thin film, Ag NM, and Ag thin film are located.

Figure 45 plots the electric field intensity at (I) $\lambda = 648$, (II) 764, and (III) 1046 nm. The electric field intensity is plotted at these wavelengths for a Si thin film with (a) 300 nm Ag thin film and (b) optimal Ag NM back reflector. The electric field intensity profiles shown in Fig. 45(II)(b) and (III)(b) indicate the excitation of leaky waveguide modes. The absorption enhancement at $\lambda = 648$ nm is due to the excitation of a cavity mode (or localized waveguide resonance near its cutoff wavelength) within the cylindrical holes of the metal NMs.[162] This resonance is independent of metal NM pitch. At $\lambda = 764$ and 1046 nm, the incident light is coupled into $(p, q) = (2, 2)$ or $(-2, -2)$ TM waveguide modes.

6.2.2.3 NM sandwich optimization Finally, we explored the combination of a metal NM on both the top and bottom of the ultrathin c-Si film. In addition to the parameters discussed previously, we further consider the spatial offset between the NMs. The frontside NM is Al and backside NM is Ag as simulated before. In addition, the backside metal NM sits on top of a 100-nm-thick Ag back reflector like in the previous structure optimized. The optimized NM sandwich consists of a frontside Al NM and a backside Ag NM with a_{top} = a_{bot} = 850 nm, d_{top} = 800 nm, t_{top} = 100 nm, d_{bot} = 500 nm, t_{bot} = 300 nm, u = 425 nm, and $v = 0$. The short-circuit current density of this structure is $J_{sc} = 13.3$ mA/cm^2, with $J_{sc,xx} = 13.6$ mA/cm^2 and $J_{sc,yy} = 13.0$ mA/cm^2 corresponding to a 41.5% and 20.7% enhancement compared to c-Si with ARC /Ag back reflector and an ideal double pass 300 nm c-Si, respectively. Figure 46 plots the (a) absorption spectra of the optimized NM sandwich compared to c-Si film with ARC and Ag back reflector, and (b) the enhancement in absorption. The enhancement in J_{sc} induced by the NM sandwich is similar to the accumulated enhancement by NM on frontside and backside separately, implying a weak coupling between the SPP near the frontside and the leaky waveguide modes.

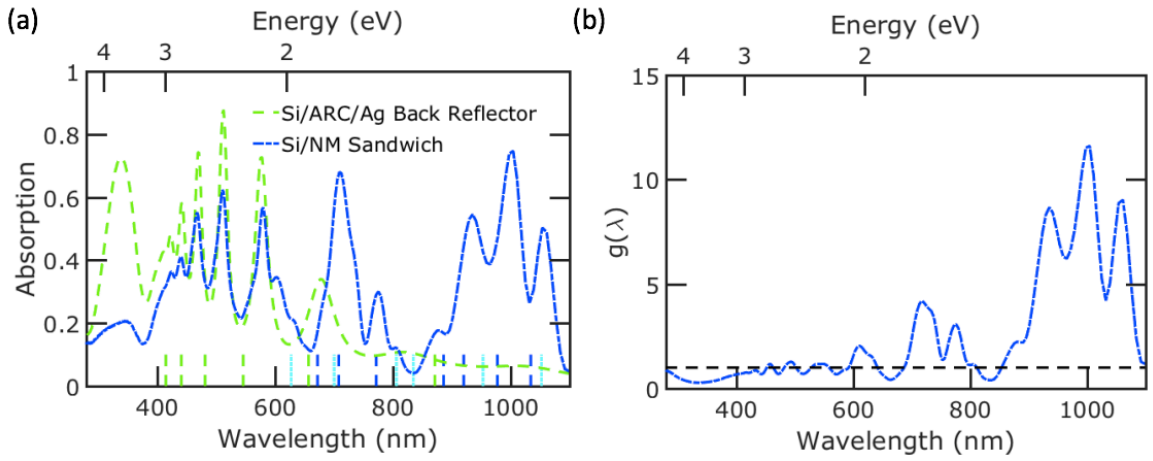

Figure 46: (a) Absorption spectrum of ultrathin c-Si film with ARC and Ag back reflector, and c-Si with the optimal NM sandwich. (b) The enhancement of the absorption as the function of wavelength.

The absorption enhancement at long wavelength regime predominantly contributes to the total enhancement, as shown in 46(a). The guided TE and TM waveguide modes for free-standing c-Si with up to $|p|$ and $|q| = 2$ are analytically calculated and plotted in Fig. 46(a) as well with blue dashed lines near the x-axis. Similarly, the SPP modes with up to $|m|$ and $|n| = 3$ are analytically calculated for the frontside Al and c-Si and plotted with cyan dotted lines near the x-axis. The combination of concentrated electric field intensity from the SPPs excited by the frontside Al NM and the excitation of waveguide modes from the backside Ag NM lead to high absorption peaks compared with just the frontside or backside NMs alone.

To reduce reflection, an additional silicon nitride Si_3N_4 ARC is used at the frontside. A flat layer of Si_3N_4 with thickness t_{ARC} is positioned upon the frontside NM with the holes in the NM also filled with Si_3N_4. The optimal structure includes an additional Si_3N_4 thin film of thickness $t_{ARC} = 100$ nm added to the former structure. The short-circuit current density of this structure is $J_{sc} = 16.25$ mA/cm^2, with $J_{sc,xx} = 16.6$ mA/cm^2 and $J_{sc,yy} = 15.9$ mA/cm^2, as shown in Fig. 47, corresponding to a 72.9% and 47.8% enhancement compared to c-Si film with ARC and Ag back reflector, and an ideal double pass 300-nm-thick c-Si thin film, respectively. The sheet resistance of the Al NM as the top electrode is $R_s = 2.4$ Ω/sq at $T_{solar} = 81\%$, satisfying the industry standard $R_S < 10$ Ω/sq.

Table 2: The short circuit current density J_{sc} of c-Si with different metal structures.

Structure	J_{sc} (mA/cm^2)
Frontside NPs	9.7
Frontside NM	9.6
Backside NM	8.7
NM Sandwich	13.3
NM Sandwich with ARC	16.25

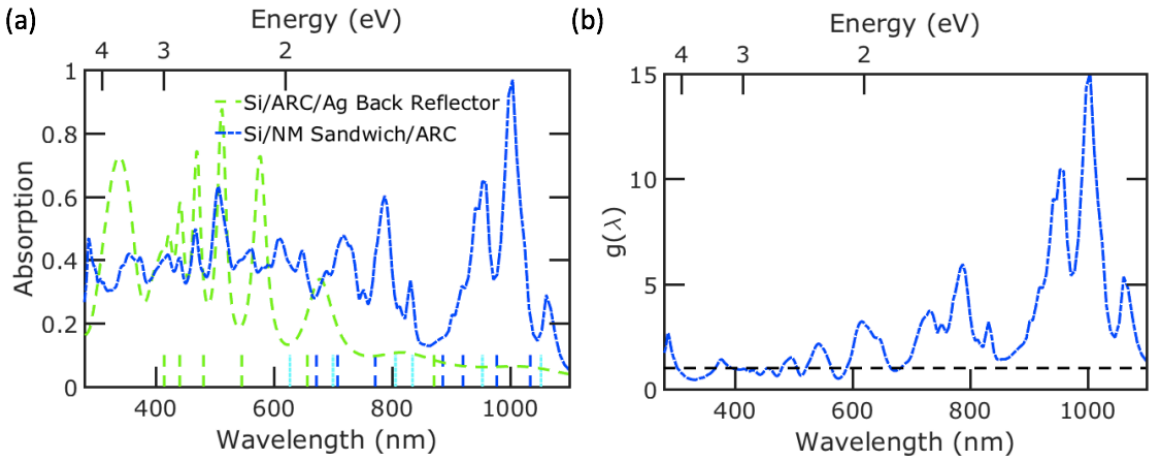

Figure 47: (a) Absorption spectrum of c-Si ultrathin film with ARC and Ag back reflector, and c-Si with the optimal double-side NMs with silicon nitride antireflection coating. (b) The enhancement of the absorption as the function of wavelength.

6.2.3 Conclusion

The frontside NM excites SPPs and couples incident light into waveguide modes in the c-Si. The backside NM supports resonances amplified by localized surface plasmons at the metal/c-Si interface. The effect of NMs on either side leads to significant absorption

enhancement in c-Si layer in long wavelength regime. To achieve a broadband enhancement, Si_3N_4 is used as antireflection coating to increase the absorption in c-Si in short wavelength regime. We illustrated how metal NM sandwich with appropriate antireflection coating may be utilized to achieve a broadband light trapping with a 72.9% enhancement in short-circuit current compared with that of a 300-nm-thick c-Si thin film solar cell with ARC and Ag back reflector.

7.0 CONCLUSIONS AND PROSPECTS

Nanoscale materials offer exciting new possibilities in material design and opportunities for high performance and low-cost TC and photovoltaic applications. In this work, I mainly focus on the development of high performance TC materials based on a variety of nanoscale and microscale building blocks using both numerical and experimental methods. Metal NW arrays for TCs are first examined. According to the simulation results, Ag NW and Cu NW array have both demonstrated a performance superior to ITO thin films. Moreover, given a fixed areal fraction, thicker NWs with wider spacing is more favorable with respect to the commonly used figure of merit σ_{DC}/σ_{op}. A 10-nm-thick Ni coating over Cu NW will serve as a protection layer against oxidation without significant impact on the TC performance. Cu NM is then studied using both simulation and experiments. A transmission over 80% at a sheet resistance of 17 Ω/sq is achievable, which is comparable to commercial ITO thin films. Cu NM is conveniently fabricated on flexible substrate and demonstrated exceptional durability against bending, heating, and abrasion. Toward even better performance and functionality, two hierarchical materials are developed. Graphene/metal MG structures show a transmission over 90% at a sheet resistance of ∼1 Ω/sq. The graphene layer also acts as protection layer for the underlying metal MG against bending and oxidation. Metal NM/MG structures are studied because they show tunable haze factor from 17% to 26%, which is especially useful for solar cells.

As a natural extension of the study on TCs, we carry on the research on the light trapping effects associated with the TCs as the top electrodes. With the preliminary results obtained from studying the effects of Ag hemisphere arrays on c-Si thin film solar cells, we systematically examine impact of incorporating NM on frontside and/or backside of an ultrathin c-Si film solar cell. The optimal NMs on both sides of the c-Si thin film solar cell

lead to a 72.9% enhancement in J_{sc} compared with c-Si of the same thickness with ARC and metal back reflector. Despite much work has been done by the TC research community to improve the performance and reduce the manufacturing cost of TCs, there are still challenges. For example, how haze factor of TCs will affect the performance of photovoltaic applications is still not entirely clear. The upper and lower bound of the haze factor for a given material system need to be systematically investigated. Beside, more device-specified TC materials need to be designed and tested, as the sole use of figure of merit may not adequately reveal how good the TCs really are.

BIBLIOGRAPHY

[1] K. Bädeker. Über die elektrische leitfähigkeit und die thermoelektrische kraft einiger schwermetallverbindungen. *Annalen der Physik*, 327(4):749–766, 1907. ISSN 1521-3889. doi: 10.1002/andp.19073270409. URL http://dx.doi.org/10.1002/andp.19073270409.

[2] Hideo Hosono, David C Paine, and David Ginley. *Handbook of transparent conductors*. Springer Science & Business Media, 2010.

[3] Michael W. Rowell and Michael D. McGehee. Transparent electrode requirements for thin film solar cell modules. *Energy Environ. Sci.*, 4(1):131–134, 2011. doi: 10.1039/C0EE00373E. URL http://pubs.rsc.org/en/Content/ArticleLanding/2011/EE/c0ee00373e.

[4] Neil Ashcroft and David Mermin. *Solid state physics*. Holt, Rinehart and Winston, New York, 1976.

[5] D.S. Ginley and C. Bright. Transparent conducting oxides. *MRS Bulletin*, 25 (8):15–21, 2000. URL http://www.scopus.com/inward/record.url?eid=2-s2.0-0034247128&partnerID=40&md5=436c11da28bea02dbd01e10766b4a84b.

[6] Lei Zhang, Yuanjun Zhou, Lu Guo, Weiwei Zhao, Anna Barnes, Hai-Tian Zhang, Craig Eaton, Yuanxia Zheng, Matthew Brahlek, Hamna F. Haneef, Nikolas J. Podraza, Moses H. W. Chan, Venkatraman Gopalan, Karin M. Rabe, and Roman Engel-Herbert. Correlated metals as transparent conductors. *Nat Mater*, 15(2):204–210, 02 2016. URL http://dx.doi.org/10.1038/nmat4493.

[7] Tongchuan Gao, Baomin Wang, Bo Ding, Jung-kun Lee, and Paul W. Leu. Uniform and ordered copper nanomeshes by microsphere lithography for transparent electrodes. *Nano Letters*, 14(4):2105–2110, 2014. doi: 10.1021/nl5003075. URL http://pubs.acs.org/doi/abs/10.1021/nl5003075.

[8] Tongchuan Gao, Zhiting Li, Po-Shun Huang, Ganesh J Shenoy, David Parobek, Susheng Tan, Jung kun Lee, Haitao Liu, and Paul W. Leu. Hierarchical graphene/metal grid structures for stable, flexible transparent conductors. *ACS Nano*, 9(5):5440 – 5446, April 2015. URL http://pubs.acs.org/doi/abs/10.1021/acsnano.5b01243.

[9] Tongchuan Gao, Po-Shun Huang, Jung kun Lee, and Paul W. Leu. Hierarchical metal nanomesh/microgrid structures for ordered and uniform transparent electrodes. *RSC Advances*, 5(87):70713–70717, Aug 2015. URL http://pubs.rsc.org/en/Content/ArticleLanding/2015/RA/C5RA14851K#!divAbstract.

[10] Michael W. Rowell, Mark A. Topinka, Michael D. McGehee, Hans-Jürgen Prall, Gilles Dennler, Niyazi Serdar Sariciftci, Liangbing Hu, and George Gruner. Organic solar cells with carbon nanotube network electrodes. *Applied Physics Letters*, 88(23):233506, 2006. ISSN 00036951. doi: 10.1063/1.2209887. URL http://link.aip.org/link/APPLAB/v88/i23/p233506/s1&Agg=doi.

[11] Sanghyun Ju, Antonio Facchetti, Yi Xuan, Jun Liu, Fumiaki Ishikawa, Peide Ye, Chongwu Zhou, Tobin J. Marks, and David B. Janes. Fabrication of fully transparent nanowire transistors for transparent and flexible electronics. *Nat Nano*, 2(6):378–384, 06 2007. URL http://dx.doi.org/10.1038/nnano.2007.151.

[12] Hui Wu, Desheng Kong, Zhichao Ruan, Po-Chun Hsu, Shuang Wang, Zongfu Yu, Thomas J. Carney, Liangbing Hu, Shanhui Fan, and Yi Cui. A transparent electrode based on a metal nanotrough network. *Nat Nano*, 8(6):421–425, 06 2013. URL http://dx.doi.org/10.1038/nnano.2013.84.

[13] Sukang Bae, Hyeongkeun Kim, Youngbin Lee, Xiangfan Xu, Jae-Sung Park, Yi Zheng, Jayakumar Balakrishnan, Tian Lei, Hye Ri Kim, Young Il Song, Young-Jin Kim, Kwang S. Kim, Barbaros Ozyilmaz, Jong-Hyun Ahn, Byung Hee Hong, and Sumio Iijima. Roll-to-roll production of 30-inch graphene films for transparent electrodes. *Nat Nano*, 5(8):574–578, 2010. ISSN 1748-3387. doi: 10.1038/nnano.2010.132. URL http://dx.doi.org/10.1038/nnano.2010.132.

[14] Liangbing Hu, Han Sun Kim, Jung-Yong Lee, Peter Peumans, and Yi Cui. Scalable coating and properties of transparent, flexible, silver nanowire electrodes. *ACS Nano*, 4(5):2955–2963, May 2010. doi: 10.1021/nn1005232. URL http://dx.doi.org/10.1021/nn1005232.

[15] Pochiang Chen, Haitian Chen, Jing Qiu, and Chongwu Zhou. Inkjet printing of single-walled carbon nanotube/ruo2 nanowire supercapacitors on cloth fabrics and flexible substrates. *Nano Research*, 3(8):594–603, 2010. ISSN 1998-0000. doi: 10.1007/s12274-010-0020-x. URL http://dx.doi.org/10.1007/s12274-010-0020-x.

[16] Sukanta De, Thomas M. Higgins, Philip E. Lyons, Evelyn M. Doherty, Peter N. Nirmalraj, Werner J. Blau, John J. Boland, and Jonathan N. Coleman. Silver nanowire networks as flexible, transparent, conducting films: Extremely high DC to optical conductivity ratios. *ACS Nano*, 3(7):1767–1774, July 2009. doi: 10.1021/nn900348c. URL http://dx.doi.org/10.1021/nn900348c.

[17] Dong Yun Choi, Yong Suk Oh, Donggeon Han, Seunghyup Yoo, Hyung Jin Sung, and Sang Soo Kim. Highly conductive, bendable, embedded ag nanoparticle wire arrays via convective self-assembly: Hybridization into ag nanowire transparent conductors.

Advanced Functional Materials, 25(25):3888–3898, 2015. ISSN 1616-3028. doi: 10.1002/adfm.201500677. URL http://dx.doi.org/10.1002/adfm.201500677.

[18] Saewon Kang, Taehyo Kim, Seungse Cho, Youngoh Lee, Ayoung Choe, Bright Walker, Seo-Jin Ko, Jin Young Kim, and Hyunhyub Ko. Capillary printing of highly aligned silver nanowire transparent electrodes for high-performance optoelectronic devices. *Nano Letters*, 15(12):7933–7942, 2015. doi: 10.1021/acs.nanolett.5b03019. URL http://dx.doi.org/10.1021/acs.nanolett.5b03019. PMID: 26540011.

[19] Colin Preston, Yunlu Xu, Xiaogang Han, JeremyN. Munday, and Liangbing Hu. Optical haze of transparent and conductive silver nanowire films. *Nano Research*, 6(7):461–468, 2013. doi: 10.1007/s12274-013-0323-9. URL http://dx.doi.org/10.1007/s12274-013-0323-9.

[20] Yinhua Zhou, Canek Fuentes-Hernandez, Jaewon Shim, Jens Meyer, Anthony J. Giordano, Hong Li, Paul Winget, Theodoros Papadopoulos, Hyeunseok Cheun, Jungbae Kim, Mathieu Fenoll, Amir Dindar, Wojciech Haske, Ehsan Najafabadi, Talha M. Khan, Hossein Sojoudi, Stephen Barlow, Samuel Graham, Jean-Luc Brédas, Seth R. Marder, Antoine Kahn, and Bernard Kippelen. A universal method to produce low–work function electrodes for organic electronics. *Science*, 336(6079):327–332, 2012. ISSN 0036-8075. doi: 10.1126/science.1218829. URL http://science.sciencemag.org/content/336/6079/327.

[21] Anuj R Madaria, Akshay Kumar, and Chongwu Zhou. Large scale, highly conductive and patterned transparent films of silver nanowires on arbitrary substrates and their application in touch screens. *Nanotechnology*, 22(24):245201, 2011. URL http://stacks.iop.org/0957-4484/22/i=24/a=245201.

[22] Jinhwan Lee, Phillip Lee, Hyungman Lee, Dongjin Lee, Seung Seob Lee, and Seung Hwan Ko. Very long ag nanowire synthesis and its application in a highly transparent, conductive and flexible metal electrode touch panel. *Nanoscale*, 4:6408–6414, 2012. doi: 10.1039/C2NR31254A. URL http://dx.doi.org/10.1039/C2NR31254A.

[23] Ja-Yeon Kim, Jong-Hyun Jeon, and Min-Ki Kwon. Indium tin oxide-free transparent conductive electrode for gan-based ultraviolet light-emitting diodes. *ACS Applied Materials & Interfaces*, 7(15):7945–7950, 2015. doi: 10.1021/am509116s. URL http://dx.doi.org/10.1021/am509116s. PMID: 25830932.

[24] Munsik Oh, Won-Yong Jin, Hyeon Jun Jeong, Mun Seok Jeong, Jae-Wook Kang, and Hyunsoo Kim. Silver nanowire transparent conductive electrodes for high-efficiency iii-nitride light-emitting diodes. *Scientific Reports*, 5:13483, 09 2015. URL http://dx.doi.org/10.1038/srep13483.

[25] Makoto Takada, Takashi Kobayashi, Takashi Nagase, and Hiroyoshi Naito. Inverted organic light-emitting diodes using different transparent conductive oxide films as a cathode. *Japanese Journal of Applied Physics*, 55(3S2):03DC06, 2016. URL http://stacks.iop.org/1347-4065/55/i=3S2/a=03DC06.

[26] Caroline Celle, Céline Mayousse, Eléonore Moreau, Henda Basti, Alexandre Carella, and Jean-Pierre Simonato. Highly flexible transparent film heaters based on random networks of silver nanowires. *Nano Research*, 5(6):427–433, 2012. ISSN 1998-0000. doi: 10.1007/s12274-012-0225-2. URL http://dx.doi.org/10.1007/s12274-012-0225-2.

[27] Sooyeun Kim and Minoru Taya. Electrochromic windows based on V_2O_5–TiO_2 and poly (3,3-dimethyl-3,4-dihydro-2h-thieno[3,4-b][1,4]dioxepine) coatings. *Solar Energy Materials and Solar Cells*, 107:225–229, 12 2012. doi: http://dx.doi.org/10.1016/j.solmat.2012.06.032. URL http://www.sciencedirect.com/science/article/pii/S0927024812003352.

[28] Mingjun Hu, Jiefeng Gao, Yucheng Dong, Kai Li, Guangcun Shan, Shiliu Yang, and Robert Kwok-Yiu Li. Flexible transparent PES/silver nanowires/PET sandwich-structured film for high-efficiency electromagnetic interference shielding. *Langmuir*, 28 (18):7101–7106, 2012. doi: 10.1021/la300720y. URL http://dx.doi.org/10.1021/la300720y. PMID: 22533864.

[29] David S. Hecht, Liangbing Hu, and Glen Irvin. Emerging transparent electrodes based on thin films of carbon nanotubes, graphene, and metallic nanostructures. *Advanced Materials*, 23(13):1482–1513, 2011. ISSN 1521-4095. doi: 10.1002/adma.201003188. URL http://dx.doi.org/10.1002/adma.201003188.

[30] Klaus Ellmer. Past achievements and future challenges in the development of optically transparent electrodes. *Nat Photon*, 6(12):809–817, 12 2012. URL http://dx.doi.org/10.1038/nphoton.2012.282.

[31] HJ Vanboort and R Groth. Low-pressure sodium lamps with indium oxide filter. *Philips Technical Review*, 29(1):17, 1968.

[32] AR Hutson. Piezoelectricity and conductivity in ZnO and CdS. *Physical Review Letters*, 4(10):505, 1960.

[33] Klaus Ellmer, Andreas Klein, and Bernd Rech. *Transparent conductive zinc oxide: basics and applications in thin film solar cells*, volume 104. Springer Science & Business Media, 2007.

[34] Brian G. Lewis and David C. Paine. Applications and processing of transparent conducting oxides. *MRS Bulletin*, 25(08):22–27, 2000. doi: 10.1557/mrs2000.147. URL http://journals.cambridge.org/action/displayAbstract?fromPage=online&aid=7966198.

[35] Indium price charts. URL http://www.smg-indium.com/Docs/IndiumPriceCharts.pdf.

[36] Th. Kugler, Å. Johansson, I. Dalsegg, U. Gelius, and W.R. Salaneck. International conference on electroluminescence of molecular materials and related phenomena elec-

tronic and chemical structure of conjugated polymer surfaces and interfaces: applications in polymer-based light-emitting devices. *Synthetic Metals*, 91(1):143 – 146, 1997. ISSN 0379-6779. doi: http://dx.doi.org/10.1016/S0379-6779(98)80076-3. URL http://www.sciencedirect.com/science/article/pii/S0379677998800763.

[37] Chia-Hua Huang, Hung-Lung Cheng, Wei-En Chang, and Ming-Show Wong. Comprehensive characterization of DC sputtered AZO films for CIGS photovoltaics. *Journal of The Electrochemical Society*, 158(5):H510–H515, 2011.

[38] Sin Liang Ou, Dong Sing Wuu, Shu Ping Liu, Yu Chuan Fu, Shih Cheng Huang, and Ray Hua Horng. Pulsed laser deposition of ITO/AZO transparent contact layers for GaN LED applications. *Opt. Express*, 19(17):16244–16251, Aug 2011. doi: 10.1364/OE.19.016244. URL http://www.opticsexpress.org/abstract.cfm?URI=oe-19-17-16244.

[39] Yong Hyun Kim, Christoph Sachse, Michael L. Machala, Christian May, Lars Müller-Meskamp, and Karl Leo. Highly conductive PEDOT:PSS electrode with optimized solvent and thermal post-treatment for ITO-free organic solar cells. *Advanced Functional Materials*, 21(6):1076–1081, 2011. doi: 10.1002/adfm.201002290. URL http://dx.doi.org/10.1002/adfm.201002290.

[40] S. C. J. Meskers, J. K. J. van Duren, R. A. J. Janssen, F. Louwet, and L. Groenendaal. Infrared detectors with poly(3,4-ethylenedioxy thiophene)/poly(styrene sulfonic acid) (PEDOT/PSS) as the active material. *Advanced Materials*, 15(7-8):613–616, 2003. doi: 10.1002/adma.200304592. URL http://dx.doi.org/10.1002/adma.200304592.

[41] Joji Ohshita, Yosuke Tada, Atsutaka Kunai, Yutaka Harima, and Yoshihito Kunugi. Hole-injection properties of annealed polythiophene films to replace pedot–pss in multilayered {OLED} systemsyered OLED systems. *Synthetic Metals*, 159(3–4):214 – 217, 2009. ISSN 0379-6779. doi: http://dx.doi.org/10.1016/j.synthmet.2008.09.002. URL http://www.sciencedirect.com/science/article/pii/S0379677908003160.

[42] Baomin Wang and Paul W Leu. Enhanced absorption in silicon nanocone arrays for photovoltaics. *Nanotechnology*, 23(19):194003, May 2012. ISSN 0957-4484, 1361-6528.

[43] Whitney Gaynor, George F. Burkhard, Michael D. McGehee, and Peter Peumans. Smooth nanowire/polymer composite transparent electrodes. *Advanced Materials*, 23 (26):2905–2910, 2011. ISSN 1521-4095. doi: 10.1002/adma.201100566. URL http://dx.doi.org/10.1002/adma.201100566.

[44] Faheem Ahmed, Shalendra Kumar, Nishat Arshi, M. S. Anwar, Lee Su-Yeon, Gyung-Suk Kil, Dae-Won Park, Bon Heun Koo, and Chan Gyu Lee. Preparation and characterizations of polyaniline (pani)/zno nanocomposites film using solution casting method nanocomposites film using solution casting method. *Thin Solid Films*, 519(23):8375–8378, 9 2011. doi: http://dx.doi.org/10.1016/j.tsf.2011.03.090. URL http://www.sciencedirect.com/science/article/pii/S0040609011007474.

[45] Min Kyoon Shin, Yu Jin Kim, Sun I. Kim, Sung-Kyoung Kim, Haiwon Lee, Geoffrey M. Spinks, and Seon Jeong Kim. Enhanced conductivity of aligned PANi/PEO/MWNT nanofibers by electrospinning. *Sensors and Actuators B: Chemical*, 134(1):122–126, 8 2008. doi: http://dx.doi.org/10.1016/j.snb.2008.04.021. URL http://www.sciencedirect.com/science/article/pii/S0925400508002906.

[46] Yangyong Wang and Xinli Jing. Transparent conductive thin films based on polyaniline nanofibers. *Materials Science and Engineering: B*, 138(1):95 – 100, 2007. ISSN 0921-5107. doi: http://dx.doi.org/10.1016/j.mseb.2006.12.016. URL http://www.sciencedirect.com/science/article/pii/S0921510707000025.

[47] Sergio H. Domingues, Rodrigo V. Salvatierra, Marcela M. Oliveira, and Aldo J. G. Zarbin. Transparent and conductive thin films of graphene/polyaniline nanocomposites prepared through interfacial polymerization. *Chemical Communications*, 47:2592–2594, 2011. doi: 10.1039/C0CC04304D. URL http://dx.doi.org/10.1039/C0CC04304D.

[48] Rodrigo V. Salvatierra, Carlos E. Cava, Lucimara S. Roman, and Aldo J. G. Zarbin. ITO-free and flexible organic photovoltaic device based on high transparent and conductive polyaniline/carbon nanotube thin films. *Advanced Functional Materials*, 23 (12):1490–1499, 2013. doi: 10.1002/adfm.201201878. URL http://dx.doi.org/10.1002/adfm.201201878.

[49] Zhifeng Wang, Peng Xiao, Lei Qiao, Xiaoqin Meng, Yunhuai Zhang, Xiaoling Li, and Fei Yang. Polypyrrole sensitized ZnO nanorod arrays for efficient photo-electrochemical splitting of water. *Physica B: Condensed Matter*, 419:51–56, 6 2013. doi: http://dx.doi.org/10.1016/j.physb.2013.03.021. URL http://www.sciencedirect.com/science/article/pii/S0921452613001695.

[50] Sumio Iijima. Helical microtubules of graphitic carbon. *Nature*, 354(6348):56–58, 1991.

[51] Francesca Mirri, Anson W. K. Ma, Tienyi T. Hsu, Natnael Behabtu, Shannon L. Eichmann, Colin C. Young, Dmitri E. Tsentalovich, and Matteo Pasquali. High-performance carbon nanotube transparent conductive films by scalable dip coating. *ACS Nano*, 6(11):9737–9744, 2012. doi: 10.1021/nn303201g. URL http://pubs.acs.org/doi/abs/10.1021/nn303201g.

[52] K. S. Novoselov, A. K. Geim, S. V. Morozov, D. Jiang, Y. Zhang, S. V. Dubonos, I. V. Grigorieva, and A. A. Firsov. Electric field effect in atomically thin carbon films. *Science*, 306(5696):666–669, 2004. doi: 10.1126/science.1102896. URL http://www.sciencemag.org/content/306/5696/666.abstract.

[53] Sasha Stankovich, Dmitriy A. Dikin, Richard D. Piner, Kevin A. Kohlhaas, Alfred Kleinhammes, Yuanyuan Jia, Yue Wu, SonBinh T. Nguyen, and Rodney S. Ruoff. Synthesis of graphene-based nanosheets via chemical reduction of exfoliated graphite oxide. *Carbon*, 45(7):1558–1565, June 2007. ISSN 0008-6223. doi: 10.1016/j.carbon.2007.02.034. URL http://www.sciencedirect.com/science/article/pii/S0008622307000917. 04777.

[54] A.E. Morgan and G.A. Somorjai. Low energy electron diffraction studies of gas adsorption on the platinum (100) single crystal surface. *Surface Science*, 12(3):405 – 425, 1968. ISSN 0039-6028. doi: http://dx.doi.org/10.1016/0039-6028(68)90089-7. URL http://www.sciencedirect.com/science/article/pii/0039602868900897.

[55] J.C. Shelton, H.R. Patil, and J.M. Blakely. Equilibrium segregation of carbon to a nickel (111) surface: A surface phase transition. *Surface Science*, 43(2):493 – 520, 1974. ISSN 0039-6028. doi: http://dx.doi.org/10.1016/0039-6028(74)90272-6. URL http://www.sciencedirect.com/science/article/pii/0039602874902726.

[56] H.J. Grabke, W. Paulitschke, G. Tauber, and H. Viefhaus. Equilibrium surface segregation of dissolved nonmetal atoms on iron(100) faces. *Surface Science*, 63(0):377 – 389, 1977. ISSN 0039-6028. doi: http://dx.doi.org/10.1016/0039-6028(77)90353-3. URL http://www.sciencedirect.com/science/article/pii/0039602877903533.

[57] J.C. Hamilton and J.M. Blakely. Carbon segregation to single crystal surfaces of Pt, Pd and Co. *Surface Science*, 91(1):199 – 217, 1980. ISSN 0039-6028. doi: http://dx.doi.org/10.1016/0039-6028(80)90080-1. URL http://www.sciencedirect.com/science/article/pii/0039602880900801.

[58] Xuesong Li, Carl W. Magnuson, Archana Venugopal, Jinho An, Ji Won Suk, Boyang Han, Mark Borysiak, Weiwei Cai, Aruna Velamakanni, Yanwu Zhu, Lianfeng Fu, Eric M. Vogel, Edgar Voelkl, Luigi Colombo, and Rodney S. Ruoff. Graphene films with large domain size by a two-step chemical vapor deposition process. *Nano Letters*, 10(11):4328–4334, 2010. ISSN 1530-6984. doi: 10.1021/nl101629g. URL http://dx.doi.org/10.1021/nl101629g. 00434.

[59] Xuesong Li, Carl W. Magnuson, Archana Venugopal, Rudolf M. Tromp, James B. Hannon, Eric M. Vogel, Luigi Colombo, and Rodney S. Ruoff. Large-area graphene single crystals grown by low-pressure chemical vapor deposition of methane on copper. *Journal of the American Chemical Society*, 133(9):2816–2819, 2011. ISSN 0002-7863. doi: 10.1021/ja109793s. URL http://dx.doi.org/10.1021/ja109793s. 00442.

[60] Weiwei Cai, Yanwu Zhu, Xuesong Li, Richard D. Piner, and Rodney S. Ruoff. Large area few-layer graphene/graphite films as transparent thin conducting electrodes. *Applied Physics Letters*, 95(12):123115, 2009. doi: http://dx.doi.org/10.1063/1.3220807. URL http://scitation.aip.org/content/aip/journal/apl/95/12/10.1063/1.3220807.

[61] Shanshan Chen, Weiwei Cai, Richard D. Piner, Ji Won Suk, Yaping Wu, Yujie Ren, Junyong Kang, and Rodney S. Ruoff. Synthesis and characterization of large-area graphene and graphite films on commercial cu–ni alloy foils alloy foils. *Nano Letters*, 11(9):3519–3525, 2011. doi: 10.1021/nl201699j. URL http://dx.doi.org/10.1021/nl201699j. PMID: 21793495.

[62] Alexander A. Balandin, Suchismita Ghosh, Wenzhong Bao, Irene Calizo, Desalegne Teweldebrhan, Feng Miao, and Chun Ning Lau. Superior thermal conductivity of

single-layer graphene. *Nano Letters*, 8(3):902–907, 2008. doi: 10.1021/nl0731872. URL http://dx.doi.org/10.1021/nl0731872. PMID: 18284217.

[63] Changgu Lee, Xiaoding Wei, Jeffrey W. Kysar, and James Hone. Measurement of the elastic properties and intrinsic strength of monolayer graphene. *Science*, 321(5887): 385–388, 2008. doi: 10.1126/science.1157996. URL http://www.sciencemag.org/content/321/5887/385.abstract.

[64] S. V. Morozov, K. S. Novoselov, M. I. Katsnelson, F. Schedin, D. C. Elias, J. A. Jaszczak, and A. K. Geim. Giant intrinsic carrier mobilities in graphene and its bilayer. *Physics Review Letters*, 100:016602, Jan 2008. doi: 10.1103/PhysRevLett.100.016602. URL http://link.aps.org/doi/10.1103/PhysRevLett.100.016602.

[65] Yuanbo Zhang, Yan-Wen Tan, Horst L Stormer, and Philip Kim. Experimental observation of the quantum Hall effect and Berry's phase in graphene. *Nature*, 438(7065): 201–204, 2005.

[66] Junbo Wu, Héctor A. Becerril, Zhenan Bao, Zunfeng Liu, Yongsheng Chen, and Peter Peumans. Organic solar cells with solution-processed graphene transparent electrodes. *Applied Physics Letters*, 92(26):263302, 2008. ISSN 00036951. doi: 10.1063/1.2924771. URL http://link.aip.org/link/APPLAB/v92/i26/p263302/s1&Agg=doi.

[67] Goki Eda, Yun-Yue Lin, Steve Miller, Chun-Wei Chen, Wei-Fang Su, and Manish Chhowalla. Transparent and conducting electrodes for organic electronics from reduced graphene oxide. *Applied Physics Letters*, 92(23):233305, 2008. doi: http://dx.doi.org/10.1063/1.2937846. URL http://scitation.aip.org/content/aip/journal/apl/92/23/10.1063/1.2937846.

[68] Xuan Wang, Linjie Zhi, and Klaus Mullen. Transparent, Conductive Graphene Electrodes for Dye-Sensitized Solar Cells. *Nano Letters*, 8(1):323–327, January 2008. doi: 10.1021/nl072838r. URL http://dx.doi.org/10.1021/nl072838r.

[69] Héctor A. Becerril, Jie Mao, Zunfeng Liu, Randall M. Stoltenberg, Zhenan Bao, and Yongsheng Chen. Evaluation of Solution-Processed Reduced Graphene Oxide Films as Transparent Conductors. *ACS Nano*, 2(3):463–470, March 2008. doi: 10.1021/nn700375n. URL http://dx.doi.org/10.1021/nn700375n.

[70] Junbo Wu, Mukul Agrawal, Héctor A. Becerril, Zhenan Bao, Zunfeng Liu, Yongsheng Chen, and Peter Peumans. Organic light-emitting diodes on solution-processed graphene transparent electrodes. *ACS Nano*, 4(1):43–48, 2010. doi: 10.1021/nn900728d. URL http://dx.doi.org/10.1021/nn900728d. PMID: 19902961.

[71] Vincent C. Tung, Li-Min Chen, Matthew J. Allen, Jonathan K. Wassei, Kurt Nelson, Richard B. Kaner, and Yang Yang. Low-temperature solution processing of graphene-carbon nanotube hybrid materials for high-performance transparent conductors. *Nano Letters*, 9(5):1949–1955, May 2009. doi: 10.1021/nl9001525. URL http://dx.doi.org/10.1021/nl9001525.

[72] Xuesong Li, Weiwei Cai, Luigi Colombo, and Rodney S. Ruoff. Evolution of graphene growth on Ni and Cu by carbon isotope labeling. *Nano Letters*, 9(12):4268–4272, December 2009. ISSN 1530-6984. doi: 10.1021/nl902515k. URL http://dx.doi.org/10.1021/nl902515k.

[73] Lewis Gomez De Arco, Yi Zhang, Cody W. Schlenker, Koungmin Ryu, Mark E. Thompson, and Chongwu Zhou. Continuous, highly flexible, and transparent graphene films by chemical vapor deposition for organic photovoltaics. *ACS Nano*, 4(5):2865–2873, 2010. doi: 10.1021/nn901587x. URL http://dx.doi.org/10.1021/nn901587x. PMID: 20394355.

[74] Peter B. Catrysse and Shanhui Fan. Nanopatterned metallic films for use as transparent conductive electrodes in optoelectronic devices. *Nano Letters*, 10(8):2944–2949, 2010. ISSN 1530-6984. doi: 10.1021/nl1011239. URL http://dx.doi.org/10.1021/nl1011239.

[75] Anuj R. Madaria, Akshay Kumar, Fumiaki N. Ishikawa, and Chongwu Zhou. Uniform, highly conductive, and patterned transparent films of a percolating silver nanowire network on rigid and flexible substrates using a dry transfer technique. *Nano Research*, 3(8):564–573, July 2010. ISSN 1998-0124, 1998-0000. doi: 10.1007/s12274-010-0017-5. URL http://www.springerlink.com/content/c88411327w6uj456/.

[76] Aaron R. Rathmell and Benjamin J. Wiley. The synthesis and coating of long, thin copper nanowires to make flexible, transparent conducting films on plastic substrates. *Advanced Materials*, 23(41):4798–4803, 2011. ISSN 1521-4095. doi: 10.1002/adma.201102284. URL http://dx.doi.org/10.1002/adma.201102284.

[77] Aaron R. Rathmell, Minh Nguyen, Miaofang Chi, and Benjamin J. Wiley. Synthesis of oxidation-resistant cupronickel nanowires for transparent conducting nanowire networks. *Nano Letters*, 12(6):3193–3199, 2012. doi: 10.1021/nl301168r. URL http://pubs.acs.org/doi/abs/10.1021/nl301168r.

[78] Zhiting Li, Yongjin Wang, Andrew Kozbial, Ganesh Shenoy, Feng Zhou, Rebecca McGinley, Patrick Ireland, Brittni Morganstein, Alyssa Kunkel, Sumedh P. Surwade, Lei Li, and Haitao Liu. Effect of airborne contaminants on the wettability of supported graphene and graphite. *Nature Materials*, 12(10):925–931, October 2013. ISSN 1476-1122. doi: 10.1038/nmat3709. URL http://www.nature.com/nmat/journal/v12/n10/abs/nmat3709.html. 00052.

[79] Chuan Fei Guo, Tianyi Sun, Qihan Liu, Zhigang Suo, and Zhifeng Ren. Highly stretchable and transparent nanomesh electrodes made by grain boundary lithography. *Nature Communications*, 5, 01 2014. URL http://dx.doi.org/10.1038/ncomms4121.

[80] Tongchuan Gao and Paul W. Leu. The role of propagating modes in silver nanowire arrays for transparent electrodes. *Optics Express*, 21(S3):A419, April 2013. ISSN 1094-4087. doi: 10.1364/OE.21.00A419. URL http://www.opticsinfobase.org/oe/fulltext.cfm?uri=oe-21-S3-A419&id=252879.

[81] Tongchuan Gao and Paul W. Leu. Copper nanowire arrays for transparent electrodes. *Journal of Applied Physics*, 114(6):063107–063107–6, August 2013. URL http://jap.aip.org/resource/1/japiau/v114/i6/p063107_s1.

[82] Shouli Bai, Chaozheng Sun, Pengbo Wan, Cheng Wang, Ruixian Luo, Yaping Li, Junfeng Liu, and Xiaoming Sun. Transparent conducting films of hierarchically nanostructured polyaniline networks on flexible substrates for high-performance gas sensors. *Small*, pages 306–310, 2014. ISSN 1613-6829. doi: 10.1002/smll.201401865. URL http://dx.doi.org/10.1002/smll.201401865.

[83] Phillip Lee, Jooyeun Ham, Jinhwan Lee, Sukjoon Hong, Seungyong Han, Young Duk Suh, Sang Eon Lee, Junyeob Yeo, Seung Seob Lee, Dongjin Lee, and Seung Hwan Ko. Highly stretchable or transparent conductor fabrication by a hierarchical multiscale hybrid nanocomposite. *Advanced Functional Materials*, 24(36):5671–5678, 2014. ISSN 1616-3028. doi: 10.1002/adfm.201400972. URL http://dx.doi.org/10.1002/adfm.201400972.

[84] Dieter K Schroder. *Semiconductor material and device characterization*. John Wiley & Sons, 2006.

[85] A. F. Mayadas and M. Shatzkes. Electrical-resistivity model for polycrystalline films: the case of arbitrary reflection at external surfaces. *Physical Review B*, 1(4):1382–1389, February 1970. doi: 10.1103/PhysRevB.1.1382. URL http://link.aps.org/doi/10.1103/PhysRevB.1.1382. 01352.

[86] N. Artunç and Z. Z. Öztürk. Influence of grain-boundary and surface scattering on the electrical resistivity of single-layered thin copper films. *Journal of Physics: Condensed Matter*, 5(5):559, February 1993. ISSN 0953-8984. doi: 10.1088/0953-8984/5/5/007. URL http://iopscience.iop.org/0953-8984/5/5/007.

[87] K.L. Chopra, S. Major, and D.K. Pandya. Transparent conductors–a status review. *Thin Solid Films*, 102(1):1–46, April 1983. ISSN 0040-6090. doi: 10.1016/0040-6090(83)90256-0. URL http://www.sciencedirect.com/science/article/B6TW0-46PB19M-T1/2/dfcd5c6ea4e7d6f873c2cbeb9ba7af98.

[88] DB Fraser and HD Cook. Highly conductive, transparent films of sputtered $In_{2-x}Sn_xO_{3-y}$. *Journal of the Electrochemical Society*, 119(10):1368–1374, 1972.

[89] G Haacke. New figure of merit for transparent conductors. *Journal of Applied Physics*, 47(9):4086–4089, 1976.

[90] Martin Dressel and George Grüner. *Electrodynamics of Solids: Optical Properties of Electrons in Matter*. Cambridge University Press, 1st edition, January 2002. ISBN 0521597269.

[91] Kane Yee. Numerical solution of initial boundary value problems involving maxwell's equations in isotropic media. *Antennas and Propagation, IEEE Transactions on*, 14

(3):302–307, 1966. ISSN 0018-926X. doi: 10.1109/TAP.1966.1138693. URL http://ieeexplore.ieee.org/xpls/abs_all.jsp?arnumber=1138693&tag=1.

[92] A. Taflove. Application of the finite-difference time-domain method to sinusoidal steady-state electromagnetic-penetration problems. *Electromagnetic Compatibility, IEEE Transactions on*, EMC-22(3):191–202, 1980. ISSN 0018-9375. doi: 10.1109/TEMC.1980.303879. URL http://ieeexplore.ieee.org/search/srchabstract.jsp?tp=&arnumber=4091372.

[93] Edward D. Palik and Gorachand Ghosh. *Handbook of optical constants of solids*. Academic Press, 1998. ISBN 9780125444231.

[94] Jean-Pierre Berenger. A perfectly matched layer for the absorption of electromagnetic waves. *Journal of Computational Physics*, 114(2):185–200, October 1994. ISSN 0021-9991. doi: 06/jcph.1994.1159. URL http://www.sciencedirect.com/science/article/pii/S0021999184711594.

[95] Solar spectral irradiance: Air mass 1.5. URL http://rredc.nrel.gov/solar/spectra/am1.5/.

[96] B. R. Cooper, H. Ehrenreich, and H. R. Philipp. Optical properties of noble metals. II. *Physical Review*, 138(2A):A494–A507, April 1965. doi: 10.1103/PhysRev.138.A494. URL http://link.aps.org/doi/10.1103/PhysRev.138.A494.

[97] DR Lide. *2010, CRC handbook of chemistry and physics*. CRC Press/Taylor and Francis, 2010.

[98] A. J. McAlister and E. A. Stern. Plasma resonance absorption in thin metal films. *Physical Review*, 132(4):1599–1602, November 1963. doi: 10.1103/PhysRev.132.1599. URL http://link.aps.org/doi/10.1103/PhysRev.132.1599.

[99] J. A. Porto, F. J. García-Vidal, and J. B. Pendry. Transmission resonances on metallic gratings with very narrow slits. *Physical Review Letters*, 83(14):2845, October 1999. doi: 10.1103/PhysRevLett.83.2845. URL http://link.aps.org/doi/10.1103/PhysRevLett.83.2845.

[100] E. Popov, M. Nevière, S. Enoch, and R. Reinisch. Theory of light transmission through subwavelength periodic hole arrays. *Physical Review B*, 62(23):16100–16108, December 2000. doi: 10.1103/PhysRevB.62.16100. URL http://link.aps.org/doi/10.1103/PhysRevB.62.16100.

[101] Y. Takakura. Optical resonance in a narrow slit in a thick metallic screen. *Physical Review Letters*, 86(24):5601–5603, June 2001. doi: 10.1103/PhysRevLett.86.5601. URL http://link.aps.org/doi/10.1103/PhysRevLett.86.5601.

[102] U. Fano. Effects of configuration interaction on intensities and phase shifts. *Physical Review*, 124(6):1866–1878, December 1961. doi: 10.1103/PhysRev.124.1866. URL http://link.aps.org/doi/10.1103/PhysRev.124.1866.

[103] Peter N. Nirmalraj, Philip E. Lyons, Sukanta De, Jonathan N. Coleman, and John J. Boland. Electrical connectivity in single-walled carbon nanotube networks. *Nano Letters*, 9(11):3890–3895, 2009. doi: 10.1021/nl9020914. URL http://pubs.acs.org/doi/abs/10.1021/nl9020914.

[104] H. Ehrenreich and H. R. Philipp. Optical properties of Ag and Cu. *Physical Review*, 128(4):1622–1629, November 1962. doi: 10.1103/PhysRev.128.1622. URL http://link.aps.org/doi/10.1103/PhysRev.128.1622.

[105] Ilia Platzman, Reuven Brener, Hossam Haick, and Rina Tannenbaum. Oxidation of polycrystalline copper thin films at ambient conditions. *The Journal of Physical Chemistry C*, 112(4):1101–1108, 2008. doi: 10.1021/jp076981k. URL http://pubs.acs.org/doi/abs/10.1021/jp076981k.

[106] Free copper price charts. URL http://www.metalprices.com/p/CopperFreeChart.

[107] Aaron R. Rathmell, Stephen M. Bergin, Yi-Lei Hua, Zhi-Yuan Li, and Benjamin J. Wiley. The growth mechanism of copper nanowires and their properties in flexible, transparent conducting films. *Advanced Materials*, 22(32):3558–3563, 2010. ISSN 1521-4095. doi: 10.1002/adma.201000775. URL http://dx.doi.org/10.1002/adma.201000775.

[108] Sukanta De and Jonathan N. Coleman. The effects of percolation in nanostructured transparent conductors. *MRS Bulletin*, 36(10):774–781, 2011. doi: 10.1557/mrs.2011.236. URL http://journals.cambridge.org/action/displayAbstract?fromPage=online&aid=8409257.

[109] Hadi Hosseinzadeh Khaligh and Irene A. Goldthorpe. Failure of silver nanowire transparent electrodes under current flow. *Nanoscale Research Letters*, 8(1):235, May 2013. ISSN 1556-276X. doi: 10.1186/1556-276X-8-235. URL http://www.nanoscalereslett.com/content/8/1/235/abstract.

[110] Erik C. Garnett, Wenshan Cai, Judy J. Cha, Fakhruddin Mahmood, Stephen T. Connor, M. Greyson Christoforo, Yi Cui, Michael D. McGehee, and Mark L. Brongersma. Self-limited plasmonic welding of silver nanowire junctions. *Nature Materials*, 11(3):241–249, March 2012. ISSN 1476-1122. doi: 10.1038/nmat3238. URL http://www.nature.com/nmat/journal/v11/n3/abs/nmat3238.html. 00070.

[111] Jorik van de Groep, Pierpaolo Spinelli, and Albert Polman. Transparent conducting silver nanowire networks. *Nano Letters*, 12(6):3138–3144, June 2012. ISSN 1530-6984. doi: 10.1021/nl301045a. URL http://dx.doi.org/10.1021/nl301045a.

[112] M.-G. Kang and L. J. Guo. Nanoimprinted semitransparent metal electrodes and their application in organic light-emitting diodes. *Advanced Materials*, 19(10):1391–

1396, 2007. doi: 10.1002/adma.200700134. URL http://dx.doi.org/10.1002/adma.200700134.

[113] C.M. Sotomayor Torres, S. Zankovych, J. Seekamp, A.P. Kam, C. Clavijo Cedeño, T. Hoffmann, J. Ahopelto, F. Reuther, K. Pfeiffer, G. Bleidiessel, G. Gruetzner, M.V. Maximov, and B. Heidari. Nanoimprint lithography: an alternative nanofabrication approach. *Materials Science and Engineering: C*, 23(1–2):23–31, January 2003. ISSN 0928-4931. doi: 10.1016/S0928-4931(02)00221-7. URL http://www.sciencedirect.com/science/article/pii/S0928493102002217. 00145.

[114] Myung-Gyu Kang, Hui Joon Park, Se Hyun Ahn, and L. Jay Guo. Transparent Cu nanowire mesh electrode on flexible substrates fabricated by transfer printing and its application in organic solar cells. *Solar Energy Materials and Solar Cells*, 94(6):1179–1184, June 2010. ISSN 0927-0248. doi: 10.1016/j.solmat.2010.02.039. URL http://www.sciencedirect.com/science/article/B6V51-4YP16TP-2/2/b71923507161208b37028a415b71e49b.

[115] John C. Hulteen. Nanosphere lithography: A materials general fabrication process for periodic particle array surfaces. *Journal of Vacuum Science & Technology A: Vacuum, Surfaces, and Films*, 13(3):1553, 1995. ISSN 07342101. doi: 10.1116/1.579726. URL http://avspublications.org/jvsta/resource/1/jvtad6/v13/i3/p1553_s1.

[116] Christy L. Haynes and Richard P. Van Duyne. Nanosphere lithography: Versatile nanofabrication tool for studies of size-dependent nanoparticle optics. *The Journal of Physical Chemistry B*, 105(24):5599–5611, June 2001. doi: 10.1021/jp010657m. URL http://dx.doi.org/10.1021/jp010657m.

[117] Hui Wu, Liangbing Hu, Michael W. Rowell, Desheng Kong, Judy J. Cha, James R. McDonough, Jia Zhu, Yuan Yang, Michael D. McGehee, and Yi Cui. Electrospun metal nanofiber webs as high-performance transparent electrode. *Nano Letters*, 10(10):4242–4248, October 2010. doi: 10.1021/nl102725k. URL http://dx.doi.org/10.1021/nl102725k.

[118] T. W. Ebbesen, H. J. Lezec, H. F. Ghaemi, T. Thio, and P. A. Wolff. Extraordinary optical transmission through sub-wavelength hole arrays. *Nature*, 391:667–669, February 1998. doi: 10.1038/35570.

[119] Hocheol Shin, Peter B. Catrysse, and Shanhui Fan. Effect of the plasmonic dispersion relation on the transmission properties of subwavelength cylindrical holes. *Physical Review B*, 72(8):085436, August 2005. doi: 10.1103/PhysRevB.72.085436. URL http://link.aps.org/doi/10.1103/PhysRevB.72.085436.

[120] Xiaozhou Ye and Limin Qi. Two-dimensionally patterned nanostructures based on monolayer colloidal crystals: controllable fabrication, assembly, and applications. *Nano Today*, 6(6):608–631, 2011.

[121] Geon Dae Moon, Tae Il Lee, Bongsoo Kim, GeeSung Chae, Jinook Kim, SungHee Kim, Jae-Min Myoung, and Unyong Jeong. Assembled monolayers of hydrophilic particles on water surfaces. *ACS Nano*, 5(11):8600–8612, 2011. doi: 10.1021/nn202733f. URL http://pubs.acs.org/doi/abs/10.1021/nn202733f.

[122] Jie Yu, Chong Geng, Lu Zheng, Zhaohui Ma, Tianya Tan, Xiaoqing Wang, Qingfeng Yan, and Dezhong Shen. Preparation of high-quality colloidal mask for nanosphere lithography by a combination of air/water interface self-assembly and solvent vapor annealing. *Langmuir*, 28(34):12681–12689, 2012. doi: 10.1021/la3026182. URL http://pubs.acs.org/doi/abs/10.1021/la3026182.

[123] Sangmoo Jeong, Liangbing Hu, Hye Ryoung Lee, Erik Garnett, Jang Wook Choi, and Yi Cui. Fast and scalable printing of large area monolayer nanoparticles for nanotexturing applications. *Nano Letters*, 10(8):2989–2994, 2010. ISSN 1530-6984. doi: 10.1021/nl101432r. URL http://dx.doi.org/10.1021/nl101432r.

[124] Jian Li, J. W. Mayer, and E. G. Colgan. Oxidation and protection in copper and copper alloy thin films. *Journal of Applied Physics*, 70(5):2820–2827, September 1991. ISSN 0021-8979, 1089-7550. doi: 10.1063/1.349344. URL http://scitation.aip.org/content/aip/journal/jap/70/5/10.1063/1.349344. 00172.

[125] T. M. Barnes, X. Wu, J. Zhou, A. Duda, J. van de Lagemaat, T. J. Coutts, C. L. Weeks, D. A. Britz, and P. Glatkowski. Single-wall carbon nanotube networks as a transparent back contact in CdTe solar cells. *Applied Physics Letters*, 90(24):243503, 2007. ISSN 00036951. doi: 10.1063/1.2748078. URL http://link.aip.org/link/APPLAB/v90/i24/p243503/s1&Agg=doi.

[126] Qing Cao, Zheng-Tao Zhu, Maxime G. Lemaitre, Ming-Gang Xia, Moonsub Shim, and John A. Rogers. Transparent flexible organic thin-film transistors that use printed single-walled carbon nanotube electrodes. *Applied Physics Letters*, 88(11):113511, 2006. ISSN 00036951. doi: 10.1063/1.2181190. URL http://link.aip.org/link/APPLAB/v88/i11/p113511/s1&Agg=doi.

[127] Budhadipta Dan, Glen C. Irvin, and Matteo Pasquali. Continuous and scalable fabrication of transparent conducting carbon nanotube films. *ACS Nano*, 3(4):835–843, April 2009. doi: 10.1021/nn8008307. URL http://dx.doi.org/10.1021/nn8008307.

[128] Adrian Southard, Vinod Sangwan, Jeremy Cheng, Ellen D. Williams, and Michael S. Fuhrer. Solution-processed single walled carbon nanotube electrodes for organic thin-film transistors. *Organic Electronics*, 10(8):1556–1561, December 2009. ISSN 1566-1199. doi: 10.1016/j.orgel.2009.09.001. URL http://www.sciencedirect.com/science/article/pii/S1566119909002626.

[129] Hsi-Wen Tien, Yuan-Li Huang, Shin-Yi Yang, Jen-Yu Wang, and Chen-Chi M. Ma. The production of graphene nanosheets decorated with silver nanoparticles for use in transparent, conductive films. *Carbon*, 49(5):1550–1560, April 2011. ISSN 0008-6223.

doi: 10.1016/j.carbon.2010.12.022. URL http://www.sciencedirect.com/science/article/pii/S0008622310009012.

[130] Sukanta De and Jonathan N. Coleman. Are there fundamental limitations on the sheet resistance and transmittance of thin graphene films? *ACS Nano*, 4(5):2713–2720, 2010. doi: 10.1021/nn100343f. URL http://dx.doi.org/10.1021/nn100343f. PMID: 20384321.

[131] Keun Soo Kim, Yue Zhao, Houk Jang, Sang Yoon Lee, Jong Min Kim, Kwang S. Kim, Jong-Hyun Ahn, Philip Kim, Jae-Young Choi, and Byung Hee Hong. Large-scale pattern growth of graphene films for stretchable transparent electrodes. *Nature*, 457 (7230):706–710, 02 2009. URL http://dx.doi.org/10.1038/nature07719.

[132] Tian Fang, Aniruddha Konar, Huili Xing, and Debdeep Jena. Carrier statistics and quantum capacitance of graphene sheets and ribbons. *Applied Physics Letters*, 91(9):092109, August 2007. ISSN 0003-6951, 1077-3118. doi: 10.1063/1.2776887. URL http://scitation.aip.org/content/aip/journal/apl/91/9/10.1063/1.2776887. 00250.

[133] Yan Yin, Zengguang Cheng, Li Wang, Kuijuan Jin, and Wenzhong Wang. Graphene, a material for high temperature devices - intrinsic carrier density, carrier drift velocity, and lattice energy. *Scientific Reports*, 4, July 2014. doi: 10.1038/srep05758. URL http://www.nature.com/srep/2014/140721/srep05758/full/srep05758.html. 00000.

[134] Xuesong Li, Weiwei Cai, Jinho An, Seyoung Kim, Junghyo Nah, Dongxing Yang, Richard Piner, Aruna Velamakanni, Inhwa Jung, Emanuel Tutuc, Sanjay K. Banerjee, Luigi Colombo, and Rodney S. Ruoff. Large-area synthesis of high-quality and uniform graphene films on copper foils. *Science*, 324(5932):1312–1314, 2009. doi: 10.1126/science.1171245. URL http://www.sciencemag.org/content/324/5932/1312.abstract.

[135] Sukanta De, Paul J. King, Mustafa Lotya, Arlene O'Neill, Evelyn M. Doherty, Yenny Hernandez, Georg S. Duesberg, and Jonathan N. Coleman. Flexible, transparent, conducting films of randomly stacked graphene from surfactant-stabilized, oxide-free graphene dispersions. *Small*, 6(3):458–464, February 2010. ISSN 16136810, 16136829. doi: 10.1002/smll.200901162. URL http://onlinelibrary.wiley.com/enhanced/doi/10.1002/smll.200901162/.

[136] Yu Wang, Xiaohong Chen, Yulin Zhong, Furong Zhu, and Kian Ping Loh. Large area, continuous, few-layered graphene as anodes in organic photovoltaic devices. *Applied Physics Letters*, 95(6):063302, 2009. ISSN 00036951. doi: 10.1063/1.3204698. URL http://link.aip.org/link/APPLAB/v95/i6/p063302/s1&Agg=doi.

[137] Alfonso Reina, Xiaoting Jia, John Ho, Daniel Nezich, Hyungbin Son, Vladimir Bulovic, Mildred S. Dresselhaus, and Jing Kong. Large area, few-layer graphene films on arbitrary substrates by chemical vapor deposition. *Nano Letters*, 9(1):30–35, 2009. doi: 10.1021/nl801827v. URL http://dx.doi.org/10.1021/nl801827v. PMID: 19046078.

[138] Fethullah Güneş, Gang Hee Han, Ki Kang Kim, Eun Sung Kim, Seung Jin Chae, Min Ho Park, Hae-Kyung Jeong, Seong Chu Lim, and Young Hee Lee. Large-area graphene-based flexible transparent conducting films. *Nano*, 4(02):83–90, 2009. URL http://www.worldscientific.com/doi/abs/10.1142/S1793292009001538. 00027.

[139] Wenzhong Bao, Jiayu Wan, Xiaogang Han, Xinghan Cai, Hongli Zhu, Dohun Kim, Dakang Ma, Yunlu Xu, Jeremy N. Munday, H. Dennis Drew, Michael S. Fuhrer, and Liangbing Hu. Approaching the limits of transparency and conductivity in graphitic materials through lithium intercalation. *Nature Communications*, 5, 07 2014. URL http://dx.doi.org/10.1038/ncomms5224.

[140] Sanjib Biswas and Lawrence T. Drzal. A novel approach to create a highly ordered monolayer film of graphene nanosheets at the liquidliquid interface. *Nano Letters*, 9(1):167–172, 2009. doi: 10.1021/nl802724f. URL http://dx.doi.org/10.1021/nl802724f. PMID: 19113892.

[141] Yanyu Liang, Johannes Frisch, Linjie Zhi, Hassan Norouzi-Arasi, Xinliang Feng, Jürgen P Rabe, Norbert Koch, and Klaus Müllen. Transparent, highly conductive graphene electrodes from acetylene-assisted thermolysis of graphite oxide sheets and nanographene molecules. *Nanotechnology*, 20(43):434007, 2009. URL http://stacks.iop.org/0957-4484/20/i=43/a=434007.

[142] Yanwu Zhu, Weiwei Cai, Richard D. Piner, Aruna Velamakanni, and Rodney S. Ruoff. Transparent self-assembled films of reduced graphene oxide platelets. *Applied Physics Letters*, 95(10):103104, 2009. doi: http://dx.doi.org/10.1063/1.3212862. URL http://scitation.aip.org/content/aip/journal/apl/95/10/10.1063/1.3212862.

[143] Byeong Wan An, Byung Gwan Hyun, So-Yun Kim, Minji Kim, Mi-Sun Lee, Kyongsoo Lee, Jae Bon Koo, Hye Yong Chu, Byeong-Soo Bae, and Jang-Ung Park. Stretchable and transparent electrodes using hybrid structures of graphene–metal nanotrough networks with high performances and ultimate uniformity. *Nano Letters*, 14 (11):6322–6328, November 2014. ISSN 1530-6984. doi: 10.1021/nl502755y. URL http://dx.doi.org/10.1021/nl502755y. 00000.

[144] Liqiang Yang, Tim Zhang, Huaxing Zhou, Samuel C. Price, Benjamin J. Wiley, and Wei You. Solution-processed flexible polymer solar cells with silver nanowire electrodes. *ACS Applied Materials & Interfaces*, 3(10):4075–4084, 2011. doi: 10.1021/am2009585. URL http://dx.doi.org/10.1021/am2009585. PMID: 21899278.

[145] Yu Chang, Mei Ling Lye, and Hua Chun Zeng. Large-scale synthesis of high-quality ultralong copper nanowires. *Langmuir*, 21(9):3746–3748, April 2005. ISSN 0743-7463. doi: 10.1021/la050220w. URL http://dx.doi.org/10.1021/la050220w. 00236.

[146] Serap Günes, Helmut Neugebauer, and Niyazi Serdar Sariciftci. Conjugated polymer-based organic solar cells. *Chemical Reviews*, 107(4):1324–1338, 2007. doi: 10.1021/cr050149z. URL http://dx.doi.org/10.1021/cr050149z. PMID: 17428026.

[147] Po-Chun Hsu, Shuang Wang, Hui Wu, Vijay K. Narasimhan, Desheng Kong, Hye Ryoung Lee, and Yi Cui. Performance enhancement of metal nanowire transparent conducting electrodes by mesoscale metal wires. *Nature Communications*, 4(2522), 09 2013. URL http://dx.doi.org/10.1038/ncomms3522.

[148] Yiling Yu and Linyou Cao. Coupled leaky mode theory for light absorption in 2D, 1D, and 0D semiconductor nanostructures. *Optics Express*, 20(13):13847–13856, June 2012. doi: 10.1364/OE.20.013847. URL http://www.opticsexpress.org/abstract.cfm?URI=oe-20-13-13847.

[149] Daniel Langley, Gaël Giusti, Céline Mayousse, Caroline Celle, Daniel Bellet, and Jean-Pierre Simonato. Flexible transparent conductive materials based on silver nanowire networks: a review. *Nanotechnology*, 24(45):452001, 2013. URL http://stacks.iop.org/0957-4484/24/i=45/a=452001.

[150] Yumi Ahn, Youngjun Jeong, and Youngu Lee. Improved thermal oxidation stability of solution-processable silver nanowire transparent electrode by reduced graphene oxide. *ACS Applied Materials & Interfaces*, 4(12):6410–6414, 2012. doi: 10.1021/am301913w. URL http://dx.doi.org/10.1021/am301913w. PMID: 23206541.

[151] Beniamino Sciacca, Jorik van de Groep, Albert Polman, and Erik C. Garnett. Solution-grown silver nanowire ordered arrays as transparent electrodes. *Advanced Materials*, 28(5):905–909, 2016. ISSN 1521-4095. doi: 10.1002/adma.201504045. URL http://dx.doi.org/10.1002/adma.201504045.

[152] S.S. Zivanovic, K.S. Yee, and K.K. Mei. A subgridding method for the time-domain finite-difference method to solve Maxwell's equations. *Microwave Theory and Techniques, IEEE Transactions on*, 39(3):471–479, 1991. ISSN 0018-9480. doi: 10.1109/22.75289.

[153] Edward D. Palik. *Handbook of Optical Constants of Solids*. Academic Press, November 1997. ISBN 0125444257.

[154] Yiling Yu and Linyou Cao. Coupled leaky mode theory for light absorption in 2D, 1D, and 0D semiconductor nanostructures. *Optics Express*, 20(13):13847–13856, June 2012. doi: 10.1364/OE.20.013847. URL http://www.opticsexpress.org/abstract.cfm?URI=oe-20-13-13847. 00011.

[155] Hanwei Gao, Joel Henzie, Min Hyung Lee, and Teri W. Odom. Screening plasmonic materials using pyramidal gratings. *Proceedings of the National Academy of Sciences*, 105(51):20146–20151, 2008. doi: 10.1073/pnas.0809034105. URL http://www.pnas.org/content/105/51/20146.abstract.

[156] Vivian E. Ferry, Jeremy N. Munday, and Harry A. Atwater. Design considerations for plasmonic photovoltaics. *Advanced Materials*, 22(43):4794–4808, 2010. ISSN 1521-4095. doi: 10.1002/adma.201000488. URL http://dx.doi.org/10.1002/adma.201000488.

[157] C. Genet and T. W. Ebbesen. Light in tiny holes. *Nature*, 445:39–46, January 2007. doi: 10.1038/nature05350.

[158] Herbert R Philipp. Optical properties of silicon nitride. *Journal of the Electrochemical Society*, 120(2):295–300, 1973.

[159] Steven G. Johnson, Shanhui Fan, Pierre R. Villeneuve, J. D. Joannopoulos, and L. A. Kolodziejski. Guided modes in photonic crystal slabs. *Physical Review B*, 60(8):5751–5758, August 1999. doi: 10.1103/PhysRevB.60.5751. URL http://link.aps.org/doi/10.1103/PhysRevB.60.5751.

[160] W. Y. Ma, H. Yang, J. P. Hilton, Q. Lin, J. Y. Liu, L. X. Huang, and J. Yao. A numerical investigation of the effect of vertex geometry on localized surface plasmon resonance of nanostructures. *Optics Express*, 18(2):843–853, Jan 2010. doi: 10.1364/OE.18.000843. URL http://www.opticsexpress.org/abstract.cfm?URI=oe-18-2-843.

[161] Stefan Alexander Maier. *Plasmonics: Fundamentals and Applications*. Springer, 1 edition, May 2007. ISBN 0387331506.

[162] Zhichao Ruan and Min Qiu. Enhanced transmission through periodic arrays of subwavelength holes: The role of localized waveguide resonances. *Physics Review Letters*, 96:233901, Jun 2006. doi: 10.1103/PhysRevLett.96.233901. URL http://link.aps.org/doi/10.1103/PhysRevLett.96.233901.